

University of Nottingham
UK | CHINA | MALAYSIA

ON THE OCCURRENCE AND TRANSPORT OF BIOMASS BURNING HAZE IN SOUTH-SOUTHEAST ASIA USING OBSERVATION DATA AND COMPUTATIONAL METHODS

Muhammad Yaasiin Oozeer, BEng.

Thesis submitted to the University of Nottingham for the degree of Doctor of Philosophy

August 2017

ABSTRACT

Biomass-burning haze (BBH) is an environmental concern which has a tremendous impact on human health and the economy in Southeast Asia (SEA). One of the worst haze events to ever hit Peninsular Malaysia occurred in June 2013 due to smoke from Riau, Central Sumatra. While biomass-burning in the region is common, the early occurrence of a haze episode of this magnitude is uncharacteristic of the seasonality of extreme fire events which usually occur between August and October in the Maritime Continent (MC). Previous studies on the June 2013 event mostly include statistical studies of the impacts of haze on air quality and health. Therefore, this study aims to investigate the phenomenology of this peculiar haze event and its underlying meteorological forcing agents. The aerosol and meteorological environment during the event is examined using the Moderate Resolution Imaging Spectroradiometer (MODIS) active fire hotspot detections and aerosol optical thickness (AOT) retrievals, satellite based precipitation retrievals and meteorological indices. Particular attention is given to El Niño Southern Oscillation (ENSO) and Madden-Julian Oscillation (MJO) conditions since these phenomena influence inter-annual and intra-seasonal fire-activity, respectively, as well as the influence of tropical cyclones (TC) over the South China Sea. The above datasets are then supported by a WRF-Chem nested simulation to provide a comprehensive picture of the event's meteorology and aerosol transport phenomenology. Indeed, while the use of weather models to study BBH has become more popular, more modelling efforts need to be put into studying the June 2013 haze event to identify the mechanisms of long range transport of haze.

A set of 13 sensitivity simulations are run to determine the physics settings which best represent the meteorology over the model domain during the June 2013 haze episode. The physics options used in the sensitivity simulations are selected based on previous WRF physics sensitivity studies and work which include WRF simulations with domains over Asia and SEA. In particular, the microphysics, cumulus parameterisation and planetary boundary layer (PBL) schemes are looked into to obtain the best agreement to observation data. The output from the sensitivity simulations are evaluated with satellite based precipitation retrievals and ground station data over Malaysia. The simulations run with the Lin microphysics scheme, Betts-Miller-Janjić

(BMJ) cumulus parameterisation scheme and Mellor-Yamada-Janjić (MYJ) planetary boundary layer scheme performed best overall. These best settings, based on the sensitivity studies, are then used in the numerical simulations which are evaluated with satellite and ground station data. The evaluation shows that model produces similar patterns and magnitudes of AOT and successfully captures the variations in smoke plume height when compared to MODIS AOD and Cloud-Aerosol Lidar and Infrared Pathfinder Satellite Observation (CALIPSO) aerosol extinction profile datasets.

The analysis of the time series ENSO conditions and MODIS fire count show that while extreme fire events are more characteristic of El Niño years, the MODIS fire count over the MC in June for the years 2001–2015 was highest in 2013 when neutral conditions prevailed. Although, the mean daily precipitation for June 2013 was below average for June for the years 2003–2015. In addition, the highest ratio of 0.89 of fire count for SPM to MC for any month for the period 2001–2015 was recorded in June 2013. An early and active TC season, which could have been the result of a strong transiting MJO, occurred in June 2013. The results show that the combined induced subsidence and flow enhancement due to TC Bebinca and the dry phases of the strong MJO event contributed to the event. The simulations further show that downward vertical motion of at least 6 cm s^{-1} prevailed over Sumatra on 22 June when TC Bebinca was most intense, while upward vertical motion reaching at least 9 cm s^{-1} prevailed over the same region before TC Bebinca on 17 June. Indeed, smoke sources were concentrated under this particular region of subsidence, where surface $PM_{2.5}$ concentrations reached at least 1000 μg m^{-3} on 22 June. Vertical cross-sections across the model domain also show that subsidence during phase 6 of the MJO prevailed over Sumatra. Intense and early TC seasons over the Western North Pacific can therefore be an indication of the occurrence of early and extreme haze events over the MC.

The numerical simulations are also used to study the convective mechanisms which are responsible for uplifting biomass-burning haze in the troposphere. These mechanisms over Sumatra and Peninsular Malaysia are under-studied and their physical mechanisms remain unclear. The $PM_{2.5}$ mass concentration, vertical wind speed plots at different levels and vertical cross-sections of major smoke plumes are analysed and the corresponding convective mechanisms identified. Three main convective mechanisms are identified, namely, orographic motion over the Barisan Mountains of Indonesia, morning convergence over the strait of Malacca and orographic motion over Peninsular

Malaysia. Results show that smoke is lifted to heights of at least 10 km in the atmosphere due to orographic lifting over Peninsular Malaysia while the average plume height increased to higher than 2 km as TC Bebinca subsided, due to the resulting decrease in subsidence. The identified mechanisms are able to uplift the biomass-burning emissions to the upper troposphere and this could have significant long-range transport and global climatic effects.

ACKNOWLEDGEMENT

I start by thanking God Almighty for giving me the drive, knowledge and patience to pursue this doctoral (PhD) work. I would not have made it without His blessing, protection and guidance.

I thank Professor Andy Chan from the bottom of my heart for having been such a supportive and understanding mentor and friend throughout my PhD studies. His sharing of advice, knowledge and guidance during the past few years have been key to finishing this project. Most importantly, I have made a friend for life in Andy.

I would also like to thank Dr Choong Wee Kang, my co-supervisor for his guidance during my PhD studies.

I wish to thank the University of Nottingham Malaysia Campus for offering the research scholarship which made this work possible. I would also like to thank the Ministry of Science Technology and Innovation (MOSTI) of Malaysia for providing financial support for this research work. This work is sponsored under contract number 06-02-12-SF0346. I also wish to thank the University of Nottingham for providing access to its High Performance Computing facility to perform the computational work presented in this thesis.

Above all I would like to thank my family for their unconditional love and support, not only during my PhD years, but also throughout my life. Without the sacrifice that my parents have made, the dedication they have shown and the tremendous effort they have put in raising my brothers and I, I would not be where I am today. I would not be the man I am today. I thank you for the values and discipline that you have inculcated in me. Mum, Dad, Yusha and Yasser, I thank you for having always been there for me. I love you all.

I would also like to thank my friends who have also been of great support during my PhD years. Maggie, I thank you for having been a great friend and colleague. Firas, my best friend, this has been quite a journey. The moments we have had together, I shall cherish forever. Thank you for always being there.

Touriya, my love, my special one, my star, I thank you for having come into my life and making me the happiest man in the world. You are proof that reality can be better than a dream. Thank you for always believing in me. I look forward to our exciting and adventurous future together.

Last but not least, thanks to the good times and happy moments which have made life a joy to live. However, I am even more grateful for the hard times and the life lessons that they have taught me. They have moulded me into the stronger and better person that I am today.

NOMENCLATURE

Latin Letters

C_D	Drag coefficient
C_p	Specific heat at constant pressure for air
$c(z)$	Threshold vertical velocity
D_g	Diameter of graupel
D_r	Diameter of rain
D_s	Diameter of snow
E	Cloud efficiency parameter
$\boldsymbol{F}$	Source and sink terms for momentum
F	Smoke emission flux
H	Injection height
H	PBL height
K	Nondimensional constant
K_c	Eddy diffusivity
L_{wv}	Latent heat of water vapour transition
l	Master length scale
M_n	nth moment of a distribution
m_b	Mass flux at cloud base
m_u	Mass flux for an updraft property u
$m(D)$	Mass relation
N_g	Particle size distribution of graupel
N_I	Number concentration of ice nuclei
N_r	Particle size distribution of rain
N_s	Particle size distribution of snow
N_t	Total numner of particles in the distribution
N_{og}	Intercept parameter of graupel
N_{or}	Intercept parameter of rain
N_{os}	Intercept parameter of snow
p	Pressure
p_h	Hydrostatic component of pressure at a given level in the atmosphere
p_{hs}	Pressure along the model surface
p_{ht}	Pressure along the top of the atmosphere
q	Specific humidity
q_g	Mixing ratio of graupel
q_I	Mixing ratio of cloud ice
q_r	Mixing ratio of rain
q_s	Mixing ratio of snow
q_m	Moisture variables
R	Perfect gas constant

T	Temperature
T_{LCL}	Temperature of parcel at the LCL
T_{ENV}	Ambient temperature
u, v	Horizontal wind components
U_g	Terminal velocity of graupel
U_r	Terminal velocity of rain
U_s	Terminal velocity of snow
$\overline{U_I}$	Mean terminal velocity of falling ice
$\boldsymbol{V}_3$	three-dimensional wind velocity
w	Vertical wind component
w_g	Approximate running-mean grid-resolved vertical velocity at the LCL
Z_{LCL}	Height of the LCL above the ground
Z_{USL}	Height at the base of the USL

Greek Letters

α	Inverse density; ensemble type
β	Constant
γ_c	correction to the local flux to account for the effect of the large eddies
δT_{vv}	Temperature perturbation
η	Vertical pressure coordinate
η_u	Normalised mass flux
κ	Von Karman constant
κ_o	Constant
κ_1	Constant
Λ_o	Constant
Λ_1	Constant
λ_g	Slope parameter of graupel
λ_r	Slope parameter of rain
λ_s	Slope parameter of snow
μ	Column mass; shape parameter
μ_{ue}	Gross fractional entrainment rate
μ_{ud}	Gross fractional detrainment rate
ρ	Air density
ρ_g	Density of graupel
ρ_s	Density of snow
ρ_w	Density of rain
Γ	Gamma function
ΔS	Entropy change
ΔT	Change in temperature
ΔP_B	Single time-step precipitation
Δp	Depths of model layers in terms of pressure

Δq	Change in specific humidity
Δt	Time step
Δz	Vertical grid size
Φ	Geopotential
$\boldsymbol{\Omega}$	Angular velocity vector of the Earth

Common Abbreviations

AOT	Aerosol Optical Thickness
API	Air Pollution Index
ARW	Advanced Research WRF
BBH	Biomass-Burning Haze
BMJ	Betts–Miller–Janjić
CALIOP	Cloud-Aerosol Lidar with Orthogonal Polarisation
CALIPSO	Cloud-Aerosol Lidar and Infrared Pathfinder Satellite Observation
CFL	Courant-Friedrichs-Levy
CMORPH	Climate Prediction Center MORPHing technique
CPC	Climate Prediction Center
DOE	Department of Environment
ECMWF	European Centre for Medium-range Weather Forecast
ENSO	El Niño Southern Oscillation
FDDA	Four-Dimensional Data Assimilation
FLAMBE	Fire Locating and Modeling of Burning Emissions
GD	Grell-Dévényi
GRIB	Gridded Binary
ITCZ	Intertropical Convergence Zone
KF	Kain-Fritsch
LCL	Lifting Condensation Level
MADE	Modal Aerosol Dynamics Model for Europe
MC	Maritime Continent
MEI	Multivariate ENSO Index
MJO	Madden Julian Oscillation
MODIS	Moderate Resolution Imaging Spectroradiometer
MYJ	Mellor-Yamada-Janjić
NAAPS	Navy Aerosol Analysis and Prediction System
NASA	National Aeronautics and Space Administration
NCAR	National Center for Atmospheric Research
NCEP	National Centers for Environmental Prediction
NOAA	National Oceanic and Atmospheric Administration
NWP	Numerical Weather Prediction
PBL	Planetary Boundary Layer
PNNL	Pacific Northwest National Laboratory

PSA	Peninsular Southeast Asia
PSD	Particle Size Distribution
PSI	Pollution Standard Index
RADM2	Second Generation Regional Acid Deposition Model
RRTM	Rapid Radiative Transfer Model
SCS	South China Sea
SEA	Southeast Asia
SORGAM	Secondary Organic Aerosol Model
SPM	Sumatra and Peninsular Malaysia
SWM	Southwest Summer Monsoon
TC	Tropical Cyclone
USL	Updraft Source Layer
WNP	Western Northern Pacific
WPS	WRF Preprocessing System
WRF	Weather Research and Forecasting
WRF-Chem	Weather Research and Forecasting with Chemistry
WSM3	WRF single-moment 3-class microphysics scheme
WSM5	WRF single-moment 5-class microphysics scheme
WSM6	WRF single-moment 6-class microphysics scheme
YSU	Yonsei University

TABLE OF CONTENTS

ABSTRACT ..... **i**

ACKNOWLEDGEMENT ..... **iv**

NOMENCLATURE ..... **vi**

Latin Letters ..... **vi**

Greek Letters ..... **vii**

Common Abbreviations ..... **viii**

TABLE OF CONTENTS ..... **x**

LIST OF FIGURES ..... **xiii**

LIST OF TABLES ..... **xvii**

1. INTRODUCTION **1**

1.1 Background and Literature Review **1**

1.2 Research Gaps **7**

1.3 Aims and Objectives **8**

1.4 Outline of Thesis **9**

2. DATA AND METHODS **11**

2.1 Datasets **11**

2.1.1 Satellite Data 11

2.1.1.1 Active fire hotspot data 11

2.1.1.2 Aerosol Optical Thickness (AOT) 12

2.1.1.3 Vertical aerosol extinction profiles 12

2.1.1.4 CMORPH precipitation 13

2.1.2 Ground Data 13

2.1.3 Meteorological Indices 14

2.2 Model Setup **14**

2.2.1 WRF-Chem Model 16

2.2.2 WRF Pre-processing System (WPS) 17

2.2.3 Real Data Initialisation 19

2.2.3.1 Meteorology 19

2.2.3.2 Emissions 20

2.2.4 Model Physics 21

2.2.5 Model Chemistry 25

3. SENSITIVITY STUDIES AND MODEL EVALUATION 26
3.1 WRF Sensitivity Study 26
3.1.1 Physics options 26
3.1.1.1 Microphysics 35
3.1.1.2 Cumulus parameterisation 40
3.1.1.3 Planetary boundary layer (PBL) 44
3.1.2 Cases 45
3.1.3 Results and Discussion 46
3.2 WRF-Chem Model Evaluation 52
3.3 Summary 57
4. THE UNCHARACTERISTIC OCCURRENCE OF THE JUNE 2013 BIOMASS-BURNING HAZE EVENT IN SOUTHEAST ASIA: COMBINED EFFECT OF THE MADDEN-JULIAN OSCILLATION AND TROPICAL CYCLONE ACTIVITY 59
4.1 Overall Aerosol and Meteorological Environment during the June 2013 Haze Event 59
4.2 2013 in Context: Time-Series of Fire, ENSO and MJO Characteristics 64
4.3 Combined Effect of Tropical Cyclone Bebinca and the MJO 68
4.4 Discussion and Summary 74
5. NUMERICAL STUDY OF THE TRANSPORT AND CONVECTIVE MECHANISMS OF BIOMASS BURNING HAZE IN SOUTH-SOUTHEAST ASIA 77
5.1 Vertical Transport and Convective Mechanisms 77
5.1.1 Orographic Motion over the Barisan Mountains in Sumatra 78
5.1.2 Convection over the Strait of Malacca 82
5.1.3 Orographic Motion over Peninsular Malaysia 84
5.2 Summary 86
6. CONCLUSION AND FUTURE WORK 88
6.1 Conclusion 88
6.2 Future Work 90
REFERENCES 92
APPENDICES 113
Appendix A: namelist.wps 113
Appendix B: namelist.input 115

PUBLICATIONS AND CONFERENCES 125
Journal Publications 125
Conferences 125

LIST OF FIGURES

Figure 1.1 Haze over Sumatra and Peninsular Malaysia in June 2013. (a) Satellite image from NASA's MODIS Aqua satellite on 19 June 2013 (NASA Worldview, 2013). The red dots correspond to the location of fire hotspots detected by MODIS. (b) Time series of observed PM_{10} mass concentrations over Muar in Malaysia from April to November 2013 (Department of Environment Malaysia, 2013a). 4

Figure 2.1 Study area. WRF-Chem model (a) domain d01 (blue) and (b) nest d02 (yellow). (c) Maritime Continent (MC) (red). 11

Figure 2.2 Horizontal and vertical grids of the ARW 16

Figure 2.3 Main components and flow chart of the WRF-Chem Modelling system specific to the current study. The blue boxes represent the main components of the modelling system while the green boxes represent the external data relevant to the system. 17

Figure 2.4 Main components of WPS and the data flow between them. 18

Figure 3.3 AOT at 550 nm, from 20 to 25 June 2013 over the MC from (a) MODIS Terra and (b) WRF-Chem simulations. Also, the comparison of (c) CALIOP-derived vertical profile of extinction coefficient at 532 nm with (d) the WRF-Chem simulated vertical profile of $PM_{2.5}$ smoke concentration along the corresponding portion of the CALIPSO ground track on 24 June 2013. The ground track is indicated by the line XX' on (b). 55

Figure 3.4 Comparison between hourly WRF-Chem simulated smoke (PM_{25}) concentrations near the surface and PM_{10} concentration at (a) Melaka, (b) Muar, (c) Seremban and (d) Cheras. The solid red square on each inset map shows the location of each corresponding site. 57

Figure 4.1 Overview of the aerosol and meteorological environment over the study region from 17 – 25 June 2013. (a) MODIS Terra and Aqua active fire hotspot detections (red dots). (b) CMORPH average daily precipitation. (c) MODIS aerosol optical thickness (AOT) at 550nm overlaid by average surface winds from the WRF-Chem simulations used in this study.....61

Figure 4.3 CMORPH daily precipitation over the region 30°S to 30°N and 30°E to 150°W for the period 10 – 28 June 2013. 63

Figure 4.4 Time series data for ENSO, fire over the MC and MJO. (a) Multivariate ENSO Index (MEI) for 1980 – 2016. The red markers correspond to haze episodes which occurred when El Niño conditions prevailed, from left to right, August - September 1982, September 1983, September 1987, August – September 1991, August to October 1994, August – October 1997, February – May 1998 (Radojevic, 2003), August – September 2002 (Fuller, 2003), August 2004 (Field et al., 2009), August 2005 (Mahmud, 2009), September – October 2006 (Wang et al., 2013), September 2009 (Hamada et al., 2013) and September – October 2015 (Field et al., 2016). The yellow markers in (a), (b) and (c) represent the June 2013 episode. (b) Monthly MODIS fire count for the MC from 2000 – 2015. (c) Monthly MODIS fire count for Sumatra and Peninsular Malaysia (SPM) for 2000 – 2015.....65

Figure 4.5 Time series data for ENSO, precipitation, fire over the MC and SPM, and MJO in June. (a) Multivariate ENSO Index (MEI) for 2001 – 2015 and mean CMORPH daily precipitation rate (mm day-1) over SPM for the years 2003–2015. SPM for CMORPH precipitation rates include data cells over the region 6°S to 7°N and 95°E to 107°E. (b) Monthly MODIS fire count for the MC and SPM, and ratio of MODIS fire count over SPM to that over MC from 2001 – 2015. (c) Wheeler index of MJO phase and color coded amplitude for the years 2003, 2004, 2005, 2009, 2012 and 2013. 67

Figure 4.6 MODIS images from the Terra and Aqua satellites for days between 17 and 26 June 2013 (a-f). The red spots correspond to regions of fire hotspots. (g-l) The corresponding WRF-Chem simulated daily averaged SLP (hPa) and near-surface wind fields (m s^{-1}). (m-r) The daily averaged and vertically integrated $PM_{2.5}$ mass concentration (Darker red plumes indicate higher concentrations of $PM_{2.5}$). The black lines over (j) represent cross-sections YY' and ZZ'. 71

Figure 4.7 Wind fields (m s^{-1}) (arrows) and Vertical wind speed (cm s^{-1}) (shaded colors) on 22 June along (a) YY' and (b) ZZ'. The colored red and blue arrows represent the overall convective cells that occur along each respective cross-section. 72

Figure 4.8 WRF-Chem simulated daily averaged vertical speed (cm s^{-1}) and wind fields (m s^{-1}) at 700 hPa height (left column) and surface $PM_{2.5}$ mass concentration (μg m^{-3}) (right column) for 17 (a-b) and 22 (c-d) June 2013, respectively. 73

Figure 5.1 Smoke plume at 09 UTC and vertical wind speed at 08 UTC on 19 June 2013. Plots of $PM_{2.5}$ mass concentration (μg m^{-3}) at (a) surface, (b) 850 hPa height and (c) 700 hPa height. (d) Isosurface of $PM_{2.5}$ mass concentration over the nest at 5 μg m^{-3}, as seen from south of the nest. (e) Wind fields (m s^{-1}) (arrows) and Vertical wind speed (cm s^{-1}) (shaded colors) at 850 hPa height. Wind fields (m s^{-1}) (arrows), Vertical PM_{10} plume (μg m^{-3}) (shaded colours-left) and Vertical Wind Speed (cm s^{-1}) (shaded colours-right) along the red line in (c). 80

Figure 5.2 Same as Figure 5.1 but for the smoke plume at 11 UTC and vertical wind speed at 10 UTC on 20 June 2013. 81

Figure 5.3 Wind fields (m s^{-1}) (arrows), Vertical PM_{10} plume (μg m^{-3}) (shaded colours-left) at 11 UTC and Vertical Wind Speed (cm s^{-1}) (shaded colours-right) at 10 UTC along the blue line in Figure 5.2(c) on 20 June 2013. 82

Figure 5.4 Same as Figure 5.1 but for the smoke plume at 23 UTC and vertical wind speed at 22 UTC on 24 June 2013. 83
Figure 5.5 Same as Figure 5.1 but for the smoke plume at 10 UTC and vertical wind speed at 09 UTC on 24 June 2013. 85
Figure 5.6 Same as Figure 5.1 but for the smoke plume at 12 UTC and vertical wind speed at 11 UTC on 25 June 2013. 86

LIST OF TABLES

Table 2.1 Grid details of the outer domain and nest used in the study. 18

Table 3.1 Summary of previous relevant sensitivity studies and precipitation/TC studies involving WRF and WRF-Chem, especially over Asia and Southeast Asia. The optimal WRF microphysics, cumulus and PBL parameterisation settings are also included. ..28

Table 3.2 Cases for sensitivity simulations. For each case name, 'SS' stands for 'Sensitivity Study'. 46

Table 3.3 Mean, standard deviation and mean bias of sensitivity simulations accumulated precipitation as compared to CMORPH for 17 to 25 June 2013. 49

Table 3.4 Comparison of hourly observed and model simulated 10m wind speed (m s^{-1}) at Johor, Terengganu, Perak and Kuala Lumpur. 50

Table 3.5 Comparison of hourly observed and model simulated 2m temperature (°C) at Johor, Terengganu, Perak and Kuala Lumpur. 51

1. INTRODUCTION

1.1 Background and Literature Review

Biomass-burning haze (BBH) in Southeast Asia (SEA) is an environmental concern that has attracted much attention during the past decade. Biomass burning has been reported to be a significant source of ozone precursor gases such as nitric oxide (NO), carbon monoxide (CO) and hydrocarbons (Crutzen et al., 1985), and is therefore also an important precursor of tropospheric ozone (Chan et al., 2003, 2000; Fujiwara et al., 1999; Liu et al., 1999). Furthermore, aerosols from such burning have been found to contribute largely to 'atmospheric brown clouds' (Ramanathan and Crutzen, 2003). More importantly, BBH reduces air quality and has alarming detrimental health effects on the populations affected. For instance, Aditama (2000) shows that haze from forest fires in Indonesia significantly increases respiratory conditions and lung function complaints. Betha et al. (2013) estimates the carcinogenic and non-carcinogenic health risk due to exposure due to fine $PM_{2.5}$ particles and suggests that exposure to $PM_{2.5}$ emissions in the vicinity of peat fires poses serious health threats. Ward (1999) also reports that mixture of particles, liquids, and gaseous compounds found in smoke from wildland fires is very complex and therefore increases the potential for adverse health effects. Kim Oanh et al. (2011) shows that the presence of toxic compounds in the particulate matter of burning smoke increases the potential toxic effects of the emission. Kunii et al. (2002) assesses the air quality and health effects of the 1997 haze disaster in Indonesia and determined that gender, history of asthma, and frequency of wearing a mask were associated with severity of respiratory problems. Wiwanitkit (2008) showed that the incidence of respiratory illness correlated with increased PM_{10} levels due to fires in Chiangmai. While the negative health effects of BBH are clear, Quah (2002) reviews the issues and policy responses to the severe damage of BBH on the regional environment and the economy during the extreme haze episode of 1997 (Nichol, 1998) and highlights the need for prompt and effective measures in face of the biomass burning problem. Gao et al. (2015) also performs health impacts and economic

losses assessment of the 2013 severe haze event in Beijing using model simulations of $PM_{2.5}$ concentrations and show that such an extreme event can cause nearly 700 premature deaths and at least 250 million US$ loss. Therefore, the impact of BBH over SEA on the atmospheric environment, economy and general well-being cannot be overstated and is receiving more and more attention, not only regionally but globally.

Numerous studies have since been performed to understand and characterise the occurrence of regularly occurring haze episodes (Field et al., 2009; Giglio et al., 2006; Reid et al., 2012, 2009). Throughout the Maritime Continent (MC), agricultural waste burning, intentional forest fires to convert forests to agricultural land, and related peat burning have been the major causes of extreme haze episodes (Field et al., 2009; Giglio et al., 2006; Quah and Johnston, 2001; Reid et al., 2013). Fire in the MC is most widespread during the drier boreal summer southwest monsoon season with a fire season that usually runs from June to October with the bulk of the fire occurring between August to early October (Reid et al., 2012). Fire activity generally starts earlier in the west of the MC with the start date propagating eastward. In fact, fire activity is a combination of economic factors and environmental opportunities. The economic factors of land clearing and agricultural maintenance are well entrenched in SEA and the meteorology of dry spells provide the opportunity to burn. Thus, if we understand the meteorological phenomenology that leads to favourable fire weather we can then start to understand and predict burning and its consequences.

During El Niño Southern Oscillation (ENSO) years (McBride et al., 2003; Rasmusson and Wallace, 1983), the already prevailing drier conditions are generally intensified, that results in more intense haze events(Field et al., 2016; Field and Shen, 2008; Nichol, 1998; Reid et al., 2012; Wang et al., 2013), the most recent extreme episodes occurring in 1997, 2006, 2009, and 2015. Nichol (1998) reports that the extreme haze episode of 1997 occurred during an intense El Niño year. Field and Shen (2008) examine drought conditions and sea surface temperature in Indonesia for 1997 – 2006 and report that severe drought and fire events are strongly influenced by El Niño events. Reid et al. (2012) further confirms that ENSO is the largest factor that influences burning in the MC. Wang et al. (2013) perform numerical simulations and show that during the period September – October 2006, the dry conditions associated with the prevailing El Niño event caused the next largest biomass burning outbreak after 1997. Field et al. (2016) discusses the even more severe haze event of 2015, reporting its strong sensitivity to

the strong El Niño of 2015. ENSO is a coupled atmosphere-oceanic phenomenon which has a major controlling effect on inter-annual climate variability over the planet. The primary manifestation of ENSO is a seesaw in sea level atmospheric pressure between the Southeast Pacific subtropical high and the region of low pressure which stretches across the Indian Ocean from Africa to northern Australia. Other influences involve surface temperature throughout the tropics and monsoonal rainfall in southern Africa, India, Indonesia and northern Australia. During normal conditions, upwelling of cool water occurs along the west coast of South America as surface winds blow from the south towards the equator. This cool water is replaced by warm water as a warm tropical current flows southward near the end of the calendar year, a condition called El Niño. During most years, the warming usually only lasts for a few weeks to about a month. However, every two to seven years, the warming lasts for many months and occurs over a large area of the tropical Pacific Ocean. This event is referred to as a major El Niño event (Ahrens, 2011).

Normally trade winds blow westward from a region of higher pressure over the eastern Pacific towards a region of lower pressure near Indonesia. As a result, upwelling occurs bringing cold water to the surface in the eastern pacific. Surface water along the equator is cool in the east and warm in the west. As the sea level rises in the western Pacific and lowers in the eastern Pacific a thick layer of warm water forms over the tropical western Pacific Ocean and a weak ocean current, called the countercurrent, flows slowly eastward towards South America. Every two to seven years, the surface atmospheric pressure pattern breaks down (as the Walker Cell breaks down), as air pressure falls over the eastern Pacific and rises over the western Pacific. If the pressure reversal is strong enough, this weakens the trade winds which are gradually replaced by west winds. These west winds strengthen the countercurrent which carry warm water towards South America. This warming effect may last for one to two years after which the pattern reverses. This seesaw pattern is called the Southern Oscillation. Pressure reversals and ocean warming are relatively simultaneous; hence this phenomenon is called El Niño / Southern Oscillation (ENSO). During an El Niño event, a large area of abnormally warm water can affect global wind patterns and the frequency of typhoons can increase over the warm central Pacific. The summer monsoon over India tends to weaken due to El Niño and drought is also felt in Indonesia, Australia and Southern Africa, while heavy rains and floods occur in Ecuador and Peru. A strong subtropical

westerly jet stream also directs storms in California in the northern hemisphere. Therefore, the weather impacts of ENSO can have worldwide economic repercussions. The resulting dry conditions and their contribution to the occurrence of BBH is of particular interest here. After an ENSO event, while the trade winds return to normal they may sometimes become exceptionally strong and result in an intensification of the normal conditions, a phenomenon called La Niña. Cold surface water is carried over the central and eastern pacific while rainy weather occurs over the western tropical Pacific.

While extreme haze events usually occur during ENSO years, severe events can occur in any year, with Central Sumatra and its Riau province being less influenced by ENSO than other regions of the MC (Reid et al., 2012). Indeed, one of the worst cases of BBH also occurred in 2013 (Vadrevu et al., 2014). The Air Pollution Index (API) in Malaysia and the Pollution Standard Index (PSI) in Singapore reached hazardous levels in June 2013 and a state of emergency was declared in Malaysia (Betha et al., 2014). The source was clear. Figure 1.1(a) shows smoke being transported from Moderate Resolution Imaging Spectroradiometer (MODIS) active fire hotspots in Riau Provence, in Central Sumatra over Peninsular Malaysia on 19 June 2013. Resulting PM_{10} concentrations in June over the city of Muar in Malaysia (Figure 1.1(b)) largely exceeded the concentrations recorded for the other months from April to November by over a factor of 4.

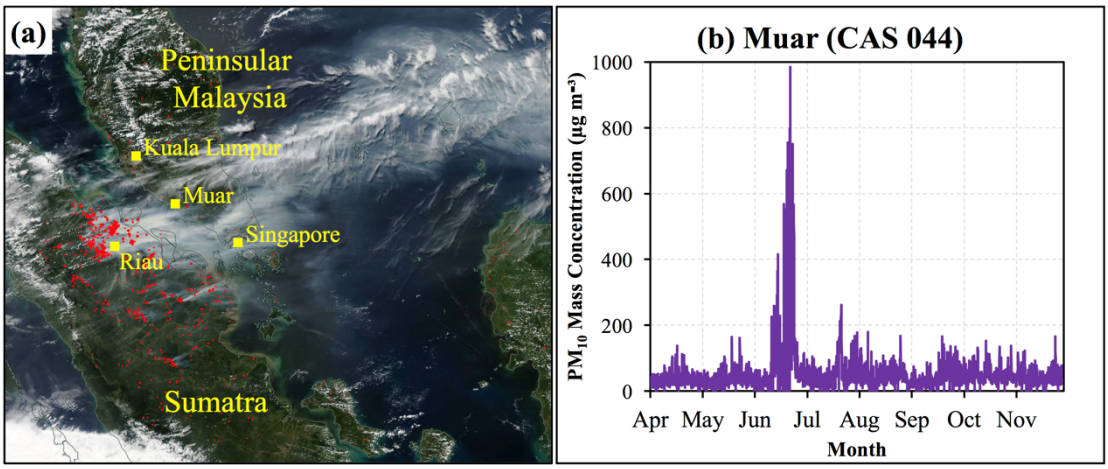


Figure 1.1 Haze over Sumatra and Peninsular Malaysia in June 2013. (a) Satellite image from NASA's MODIS Aqua satellite on 19 June 2013 (NASA Worldview, 2013). The red dots correspond to the location of fire hotspots detected by MODIS. (b) Time series of observed PM_{10} mass concentrations over Muar in Malaysia from April to November 2013 (Department of Environment Malaysia, 2013a).

In addition, while ENSO influences inter-annual fire activity, the wet and dry phases of the Madden-Julian Oscillation (MJO; Madden and Julian, 1971; Zhang, 2005, 2013; Wu and Hsu, 2009) over the MC also modulate intra-seasonal fire activity in the MC (Reid et al., 2015, 2012). The MJO is a 30-90 days large-scale coupled pattern of meso-synoptic scale circulation and deep convection that propagates eastward at a speed of ~ 5 ms^{-1} through regions of the Indian Ocean and the Pacific Ocean where the sea surface is warm (Madden and Julian, 1971; Zhang, 2013, 2005). MJO activity can be classified into eight phases. In phase 1, enhanced convection associated with MJO genesis occurs over Africa and western Indian Ocean. By phases 2 and 3, convection is present over the Indian Ocean and approaches the MC by phase 4. Convection enters the Pacific Ocean during phase 5 which induces significant drying over the MC. Maximum drying occurs over the MC during phases 6 and 7 as convection propagates further over the Pacific Ocean. The convection regime ultimately terminates in phase 8. Fire activity usually peak over the MC during phases 5 to 7 as MJO induced subsidence inhibits precipitation over the region (Reid et al., 2012; Zhang, 2005). The increase in fire activity in the southern MC and transport of smoke over the SCS as tropical cyclones transit the South China Sea (SCS) has also been reported (Reid et al., 2015, 2012).

While the most significant fire events in the MC usually occur between August and early October, fire events in June are not uncommon (Reid et al., 2012). However, the extreme magnitude of this June 2013 haze event is unique in the modern data record and has thus garnered significant attention. Previous studies on the June 2013 haze event mostly include statistical studies of the impacts of haze on air quality and health (Betha et al., 2014; Ho et al., 2014; Velasco and Rastan, 2015). Vadrevu et al. (2014) have assessed the June 2013 episode based on satellite retrievals and shows that the aerosol optical thickness (AOT) for June 2013 is significantly higher than the previous years. However, despite these efforts, to date there has yet to be an overarching discussion of the overall meteorology and physics that led to this unprecedented event. This study therefore seeks to investigate the meteorological environment that prevailed during the haze episode and the parameters which have contributed to its intensification. Here we systematically examine the strong scale dependencies that interact to create such a significant event, starting with inter-seasonal ENSO, followed by the MJO and tropical cyclone (TC) activity over the South China Sea (SCS) (Goh and Chan, 2010; Ying et al., 2014). In 2013, the TC season in the western north Pacific (WNP) was

marked by an above average genesis of TCs and was characterised by an early active TC season in June (Ying et al., 2014). This early and active TC season could have had an important influence on the occurrence of the haze event and its interaction with weather over the MC therefore needs to be investigated.

This study predominantly exercises the Weather Research and Forecasting model with Chemistry (WRF-Chem) (Fast et al., 2006; Grell et al., 2005) to investigate in detail the relative influence of TC activity over the SCS on the intensification of the June 2013 haze event. The WRF-Chem model is an online-coupled regional meteorological model which can simultaneously simulate weather, aerosol life cycle, aerosol-cloud-radiation interactions and gas-phase chemistry. The use of WRF-Chem to simulate BBH has become more extensive during the past few years. Wu et al. (2011a, 2011b) evaluates the performance of WRF-Chem in simulating the distribution and evolution of biomass-burning aerosols and investigates their effects on clouds and precipitation during the dry season in South America. In SEA, Lin et al. (2014) uses WRF-Chem to simulate the transport of biomass-burning plumes from Peninsular Southeast Asia (PSA) and studied their radiative effects on the atmosphere. Wang et al. (2013) simulates the transport of smoke particles over the MC during the September to October 2006 haze episode, looking into the interplay of sea/land breezes, storm and topographic effects, while Ge et al. (2014) simulates the direct and semi-direct radiative impacts of smoke particles for the same episode using WRF-Chem. Gao et al. (2014) also simulates the radiative forcing of aerosols over East Asia using WRF-Chem and show that the model can reproduce the observed spatial distributions of aerosol concentration and AOT from site stations. Aouizerats et al. (2015) uses WRF-Chem to model the haze episode of 2006, focusing on the evolution of the fire plume composition and its interaction with the urban region of Singapore. More recently, Ge et al. (2017) use an ensemble of 24 WRF-Chem simulations to reproduce and study the time series of observed surface $PM_{2.5}$ concentrations observed from the Vasco vessel during September 2011. In this study, WRF-Chem is used to investigate the influence of the prevailing tropical cyclone Bebinca on the June 2013 haze event over SEA.

The WRF-Chem simulations used in this work provide the opportunity to study in detail the transport mechanisms of haze from Sumatra over to Peninsular Malaysia during the 2013 event. In fact, one of the most important phenomena in large-scale haze is deep convection (Lin et al., 2009). This is the most frequently mentioned mechanism for the

transport of biomass-burning products up in the troposphere. Deep convection is able to carry biomass-burning air pollutants to higher altitudes over SEA and is a leading candidate to explain climate change in context (Chan et al., 2003; Folkins et al., 1997). A strong convection mechanism responsible for the uplifting of biomass-burning emissions over Indonesia, Papua New Guinea and Malaysia has also previously been at the centre of discussions (Folkins et al., 1997). Lin et al. (2009) have identified leeside troughs over Indochina as major contributors to the uplifting of the tracer in a tracer modelling study while Cheng et al. (2013) have identified that biomass-burning emissions are lifted due to thermal forcing-induced upward motion and high terrain in the northern part of SEA. While the uplifting mechanisms have been studied in PSA, there is a need to identify the convective mechanisms responsible for the uplifting of biomass-burning emissions in Southern SEA, as literature in this region on the mechanisms remain scarce. Most studies on BBH are restricted to the immediate dispersion and haze trajectories to neighbouring countries (Lin et al., 2009) when measurements show that deep convection in SEA can lift biomass-burning emissions up in the troposphere (Folkins et al., 1997). It is therefore important to get a better understanding of the uplifting mechanisms, and this is a gap that this study also aims to fill.

1.2 Research Gaps

In light of the above, the main identified research gaps are summarised as follows:

a) The June 2013 haze episode is still an understudied smoke event which requires attention. The previous studies on the event are mostly statistical and do not provide a detailed discussion of the meteorology and physical mechanisms of the event and the transport of smoke.
b) While fire events in June are not uncommon, the extreme magnitude of the June 2013 haze event is unique in the modern data record, which raises questions. Is such an event simply a one-off event or could it become a regularity? In any case, the uncharacteristic and unique nature of this event needs to be investigated.
c) While the use of weather models, in particular WRF-Chem, to study biomass burning haze events in detail (spatially and temporally), has become more popular in recent years, more modelling efforts need to be put into studying the

June 2013 haze event to identify the mechanisms of long range transport of smoke and its reach.

d) In addition, most previous modelling efforts on haze transport over the source region, that is Southern SEA, are limited to the immediate dispersion and trajectories of haze. The convective mechanisms that uplift haze up in the troposphere over Southern SEA are yet to be identified and studied in detail.

1.3 Aims and Objectives

In an attempt to fill the gaps described above, the aims and objectives of this work are as follows:

a) To perform a set of sensitivity studies with WRF to identify the physics settings which best represent the meteorological environment during the haze episode. These settings are to be used in the WRF-Chem model to simulate the transport of smoke. Also, to evaluate the performance of the WRF-Chem model with the multiple datasets, namely, satellite datasets (MODIS AOT, vertical aerosol extinction profiles and the Climate Prediction Center (CPC) MORPHing technique product (CMORPH) precipitation) and air quality data from ground stations over Peninsular Malaysia. This serves to provide confidence about the use of WRF-Chem in this study and for the prediction of haze transport over the region.

b) Investigate the overall aerosol and meteorological environment over Southern SEA during the June 2013 haze episode using multiple datasets. These include satellite data (active fire hotspot data, MODIS AOT, vertical aerosol extinction profiles and the Climate Prediction Center (CPC) MORPHing technique product (CMORPH) precipitation), ground data (air quality data from ground stations over Peninsular Malaysia) and meteorological indices (Multivariate ENSO Index (MEI) and MJO phase and amplitude). Also, to investigate in context the 2013 haze episode as compared to previous extreme haze events, and therefore the uniqueness and uncharacteristic nature of this event, using the active fire hotspot data and meteorological indices. In addition, to employ the WRF-Chem model with the Fire Locating and Modeling of Burning Emissions (FLAMBE) dataset to simulate in detail the transport of haze over SEA during the haze event. In particular, the aim is to study in detail the temporal

progression of the haze event and the influence of TC activity on the occurrence and dynamics of the 2013 haze event in Sumatra. Finally, to investigate the interaction between the early and active TC season and other meteorological factors, in particular MJO, which could have contributed to the occurrence of the June 2013 haze event.

c) To demonstrate the influence of topography on air motion and therefore the transport of haze over Sumatra and Peninsular Malaysia, as part of the study of the uplifting mechanisms of smoke. Also, to identify regions of deep convection near and downwind of the forest fire hotspots and therefore the convective mechanisms responsible for vertical BBH plume dispersion.

While the above objectives have been established it is important to highlight the limitations associated with the methods used to achieve them. For instance, the MODIS active fire hotspot data can only be considered semi-quantitatively since cloud cover can block the heat signature of fires (Reid et al., 2013). Furthermore, the MODIS AOT data over the study region can be problematic due to cirrus cover, but nevertheless the location and relative intensity of individual fire events can be tracked (Reid et al., 2013). Finally, the relatively coarse resolution of 27 km model domain used for computational efficiency, can overestimate wind speed due to smoother orography in coarse domains (Gómez-Navarro et al., 2015).

The achievement of the above objectives will improve our understanding of the transport mechanisms and predicting ability of the occurrence of BBH in South SEA and will hopefully help to develop more effective inter-governmental policies on the issue. More importantly, this work may help in the formulation of emission control policies which aim at reducing emissions at times when the prevailing meteorological factors are conducive to the occurrence of extreme haze events. Furthermore, these policies would aim at reducing burning when the biomass burning emissions are likely to be carried over regions of deep convection, thus limiting long range transport of these emissions.

1.4 Outline of Thesis

Chapter 1 discusses the basis of the project by outlining the background and motivation of the present study, reviewing the literature, iterating what has been done, identifying the research gaps and proposing the contributions that the present study can make to

the body of work undertaken in the field of biomass burning haze in Southeast Asia. The objectives and significance of the research are also discussed.

Chapter 2 provides a description of the datasets that are used for the analysis of observations in this study. It also includes a description of the WRF-Chem model used in this work and its different relevant components.

Chapter 3 presents sensitivity studies which were performed with WRF to identify the physics settings which best represent meteorology over Southeast Asia during the June 2013 haze episode. These settings are then used in the WRF-Chem model to simulate haze transport during the event. The WRF-Chem model used in this study is evaluated with the datasets described in Chapter 2.

Chapter 4 contains a detailed description of the phenomenology and progression of the June 2013 haze event based on observations and the WRF-Chem model results. The overall aerosol and meteorological environment during the event is described using the satellite datasets and meteorological indices. A time series of the fire, ENSO and MJO characteristics is then provided to put the 2013 event in context and understand its uncharacteristic nature. This is followed by a detailed analysis of the model results to identify the effects of TC activity and the MJO on the intensification of BBH in June 2013.

Chapter 5 presents the identified vertical transport mechanisms which uplifted haze from Sumatra to the upper troposphere, based on the WRF-Chem model results from the model nest. Smoke concentrations at different levels in the atmosphere are studied, as well as vertical cross-sections of the smoke plumes and vertical wind speed.

Chapter 6 concludes the entire project and deliberates on future research directions. These include conclusions from the sensitivity studies performed with WRF, the WRF-Chem model evaluation, the phenomenology of the June 2013 haze episode and the convective mechanisms which are responsible for the uplifting of haze over Sumatra and Peninsular Malaysia.

2. DATA AND METHODS

The work presented in this thesis includes analysis based on a set of observations and WRF-Chem simulations. The selection of datasets for the analysis of observations is based on the work of Reid et al. (2012). The datasets and WRF-Chem model used in this work are outlined herein. The study area, which covers the MC and SCS, is shown in Figure 2.1.

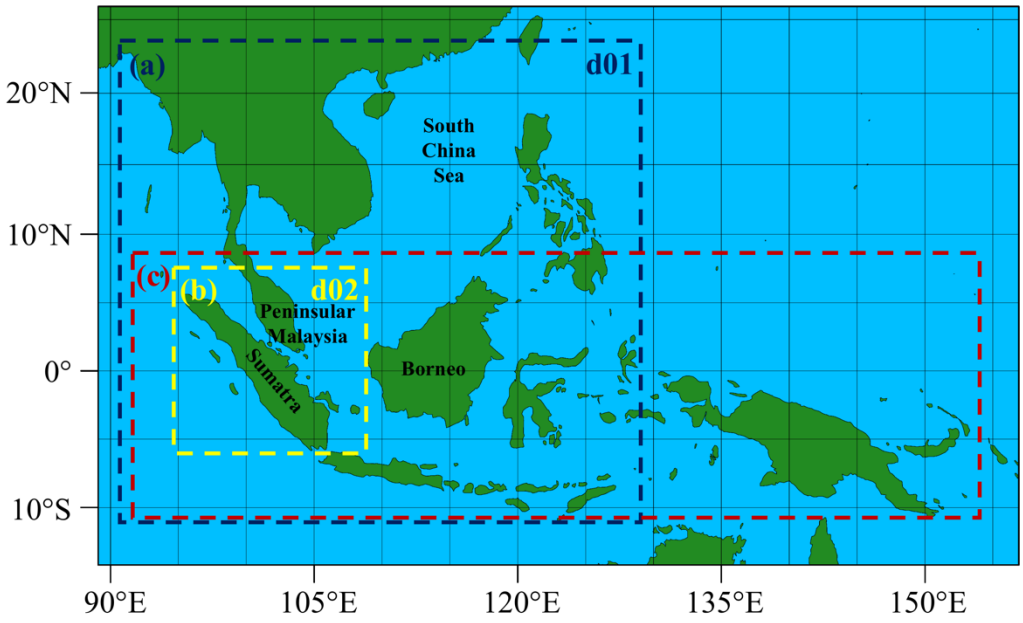


Figure 2.1 Study area. WRF-Chem model (a) domain d01 (blue) and (b) nest d02 (yellow). (c) Maritime Continent (MC) (red).

2.1 Datasets

2.1.1 Satellite Data

2.1.1.1 Active fire hotspot data

In this study, the active fire hotspot data of MODIS Terra (~10:30 LST) and Aqua (~13:30 LST) are used to show fire activity for the years 2000–2015, for which a complete record exists (Giglio et al., 2003; Justice et al., 2002). The MODIS Terra MOD14CM1 (GES DISC Northern Eurasian Earth Science Partnership Initiative Project, 2006a) and Aqua MYD14CM1 (GES DISC Northern Eurasian Earth Science

Partnership Initiative Project, 2006b) 1 degree gridded monthly active fire products are used for the temporal analysis of fire activity while combined MODIS Terra and Aqua 1 km daily active fire products are used to depict the overall fire activity during the June 2013 haze episode. Reid et al. (2013) have pointed out that these data can only be considered semi-quantitatively since cloud cover can block the heat signature of fires. Fires in the MC are also sometimes too small to be detected by fire hotspot satellite products (Miettinen and Liew, 2009).

2.1.1.2 Aerosol Optical Thickness (AOT)

AOT at 550 nm obtained from the National Aeronautics and Space Administration (NASA) MODIS col 6 Level 3 data product are also used in this study (Levy et al., 2013). The col 6 aerosol datasets are created from three separate retrieval algorithms which operate over different types of surfaces. The 'Dark Target' algorithm is used for retrievals over ocean and vegetated/dark-soiled land, which are both dark in the visible. The 'Deep Blue' algorithm is used for retrievals over desert/arid land which is bright in the visible. The 1 degree global-gridded daily MODIS Terra MOD08_D3 and MODIS Aqua MYD08_D3 combined Dark Target and Deep Blue AOT products are used for analysis and model evaluation. Like fire data, AOT data in this region can be problematic due to high cirrus cover but nevertheless can track the location and relative intensity of individual fire events (Reid et al., 2013). The AOT datasets used in this work can be obtained from NASA's GIOVANNI website (NASA Giovanni, 2013).

2.1.1.3 Vertical aerosol extinction profiles

Vertical profiles from the Cloud-Aerosol Lidar with Orthogonal Polarisation (CALIOP; Winker et al., 2010) instrument on board the Cloud-Aerosol Lidar and Infrared Pathfinder Satellite Observation (CALIPSO) satellite are used to evaluate the vertical distribution and height of smoke plumes in the WRF-Chem simulations. CALIPSO differentiates itself from other Earth observing satellites like MODIS by its ability to collect data about clouds and aerosols along the vertical. CALIOP is three-channel lidar which collects 532 nm parallel, 532 nm perpendicular and 1064 nm light scattered from clouds and aerosols in the atmosphere. Since CALIOP is a nadir-only instrument, it only collects data along the ground track of the satellite. The CALIOP level-2 product containing 532 nm extinction coefficient data at a horizontal and vertical resolution of 5 km and 60 m, respectively, under 20 km is used in this study. The CALIPSO data

product can be downloaded from the CALIPSO Search and Subsetting Web Application (NASA Calipso, 2013).

2.1.1.4 CMORPH precipitation

Precipitation data is obtained from the high resolution CMORPH (Joyce et al., 2004). The CMORPH method uses motion vectors which are derived from half-hourly geostationary satellite infrared imagery to propagate the high-quality precipitation estimates which are derived from passive microwave satellite scans. Examples of passive microwave instruments which provide precipitation estimates are the Advanced Microwave Sounding Unit-B (AMSU-B), the Special Sensor Microwave Imager (SSM/I) and the TRMM Microwave Imager (TMI). In this work, the 3-hour interval and 0.25° resolution CMORPH data are used for analyses. CMORPH data are used as they best represent the temporal and spatial patterns of tropical precipitation (Dinku et al., 2008; Janowiak et al., 2005; Sapiano and Arkin, 2009; Shen et al., 2010). Dinku et al. (2008) evaluate several high resolution satellite products over Ethiopia and Zimbabwe and find CMORPH to perform best over both regions. Janowiak et al. (2005) use CMORPH data to examine the diurnal cycle of precipitation regionally and globally. Sapiano and Arkin (2009) compare global precipitation from five high resolution datasets and show that CMOPRH has the highest correlations with the validation data. Finally, Shen et al. (2010) evaluate the performance of six high resolution satellite products over China and show that CMORPH performs best at depicting the spatial pattern and temporal variations of precipitation.

2.1.2 Ground Data

Observed data recorded at ground stations over Peninsular Malaysia, provided by the Malaysia Department of Environment (DOE Malaysia), are also used to evaluate the WRF-Chem model in this study. DOE Malaysia operates a network of 52 air quality monitoring stations. Air quality is monitored using an Air Pollutant Index (API) which is calculated based on the concentration of air pollutants, namely, sulphur dioxide (SO_2), nitrogen dioxide (NO_2), carbon monoxide (CO), ozone (O_3) and particulate matter of less than 10 microns in size (PM_{10}) recorded at the stations. The data that are of interest for the evaluation of the WRF-Chem model are 10 m wind speed, 2 m temperature and PM_{10} mass concentration. More information on the DOE air quality monitoring stations and the API can be obtained on the official DOE website

(Department of Environment Malaysia, 2013b). A summary of the API categories is also listed in Table 2.1.

Table 2.1 Summary of the ranges of index values and the corresponding categories for the Malaysian API system (Department of Environment Malaysia, 2017)

API	Category
< 50	Good
51 – 100	Moderate
101 – 200	Unhealthy
201 – 300	Very Unhealthy
> 300	Hazardous

2.1.3 Meteorological Indices

The multivariate indices of Wolter and Timlin (1998) and Wheeler and Hendon (2004) are used for the temporal analysis of ENSO and MJO respectively. The multivariate ENSO Index (MEI) is a measure of the ENSO signal which is based on six observed variables over the tropical pacific, namely, sea-level pressure, surface zonal and meridional wind components, sea surface temperature, surface air temperature and cloudiness (Wolter and Timlin, 1998). On the other hand, the seasonally independent index for monitoring the MJO is based on a pair of empirical orthogonal functions (EOFs) of the combined fields of near-equatorially averaged 850-hPa zonal wind, 200-hPa zonal wind, and satellite-observed outgoing longwave radiation (OLR) data. By combining the wind and cloud data at these two levels, a measure of the location and strength of the MJO can be obtained, that is, the MJO phase and amplitude. Monthly MEI data from the year 1950 onwards can be obtained from the MEI page on the National Oceanic and Atmospheric Administration (NOAA) website (NOAA, 2015) while data for the MJO phases and amplitude can be found on the MJO page of the Bureau of Meteorology website (Bureau of Meteorology, 2013).

2.2 Model Setup

Numerical Weather Prediction (NWP) is a discipline developed in the second half of the twentieth century which involves the use of computational techniques to solve equations that describe the behaviour of the atmosphere. The characteristic parameters of the atmosphere are computed from initial values which are obtained from

meteorological observations. The equations used in atmospheric models are obtained by simplifying the basic general equations of fluid dynamics (Coiffier, 2011). These simplifications are justified by the scale of the atmosphere to be studied. Furthermore, the traditional approximation in meteorology approximates the atmosphere to a thin layer which leads to a system of non-hydrostatic equations which are capable of handling mesoscale atmospheric motion. The non-hydrostatic equations are obtained from the Euler equations which describe the behaviour of a non-viscous fluid. Atmospheric models are built from the equations of motion (momentum equations), the mass conservation equation (continuity equation), the energy conservation equation (thermodynamic equation), the water vapour equation, equation of state. For unit mass, with a frame of reference attached to the Earth and having its origin located at the Earth's centre, the equations (Coiffier, 2011) take the form,

$$\frac{d\boldsymbol{V_3}}{dt} = -2\boldsymbol{\Omega}\times\boldsymbol{V_3} - \frac{1}{\rho}\boldsymbol{\nabla_3}p - \boldsymbol{\nabla_3}\Phi + \boldsymbol{F}, \text{ momentum equations,} \tag{2.1}$$

$$\frac{dT}{dt} = \frac{R}{C_p}\frac{T}{p}\frac{dp}{dt} + \frac{Q}{C_p}, \text{ energy equation,} \tag{2.2}$$

$$\frac{d\rho}{dt} = -\rho\boldsymbol{\nabla_3}\cdot\boldsymbol{V_3}, \text{ continuity equation,} \tag{2.3}$$

$$\frac{dq}{dt} = M, \text{ water vapour equation,} \tag{2.4}$$

$$p = \rho RT, \text{ equation of state,} \tag{2.5}$$

where $\boldsymbol{V}_3$ represents the three-dimensional wind velocity, $\boldsymbol{\Omega}$ is the angular velocity vector of the Earth, Φ is the geopotential, ρ is the air density, p is pressure, T the temperature, q the specific humidity, R and C_p the perfect gas constant and specific heat at constant pressure for air. The symbol $\boldsymbol{\nabla}_3$ denotes the gradient operator, $\boldsymbol{\nabla}_3\cdot$ denotes the divergence operator and $\frac{d}{dt}$ the total derivative operator whose expression depends on the system of coordinates adopted. $\boldsymbol{F}$, Q and M represent the source and sink terms for momentum, heat and specific humidity, respectively.

The WRF-Chem model (Fast et al., 2006; Grell et al., 2005) is employed in this work. It is an online-coupled regional meteorological model which can simultaneously simulate weather, aerosol life cycle, aerosol-cloud-radiation interactions and gas-phase chemistry. The meteorological and chemistry components are fully consistent with each other, using the same transport scheme (mass and scalar preserving), the same

horizontal and vertical grids, the same physics schemes for subgrid-scale transport and the same time step.

2.2.1 WRF-Chem Model

The fully compressible, Eulerian and non-hydrostatic Advanced Research WRF (ARW) model version 3.6.1 coupled with Chemistry (WRF-Chem) is used in this study. The main developers include NOAA, National Center for Atmospheric Research (NCAR) and the Pacific Northwest National Laboratory (PNNL), among others. More information on the ARW solver and WRF-Chem can be found on the WRF user's page (UCAR, 2017) and WRF-Chem page respectively (NOAA, 2016).

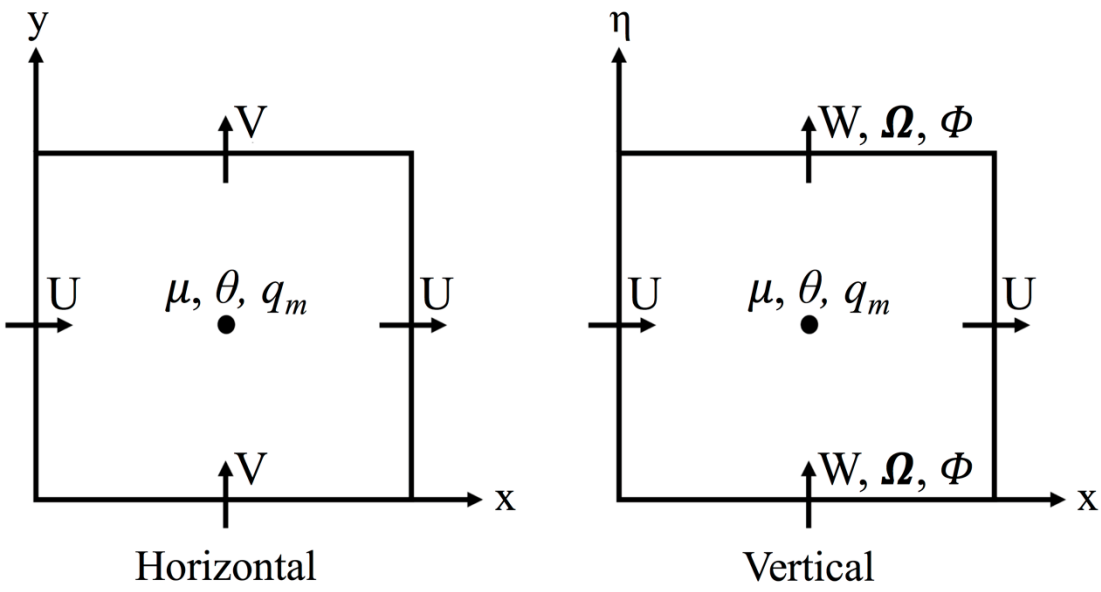


Figure 2.2 Horizontal and vertical grids of the ARW

The WRF-ARW solver uses the terrain-following, dry hydrostatic pressure for vertical coordinates and the Arakawa C-grid staggering for horizontal grids. Skamarock *et al.* (2008) give a description of the horizontal and vertical grids used in WRF-ARW which are shown in Figure 2.2. The normal velocities are staggered at one-half grid length from the thermodynamic variables. The points where the potential temperature, θ, is located are denoted as the mass points while the locations of u, v and w are denoted as the u points, v points and w points, respectively. The column mass μ and the moisture variables q_m are defined at the mass points while the Φ and $\boldsymbol{\Omega}$ are defined at the w points. The diagnostic variables used in the model, that is, pressure p and inverse density α, are computed at the mass points. η represents the vertical pressure coordinates.

Time-integration is performed using the second and third-order Runge-Kutta scheme with a time-split smaller time-step scheme for acoustic and gravity-wave models while second to sixth order advection schemes are used in the horizontal and the vertical (Skamarock et al., 2008). The model supports multiple dynamics solvers and physics modules. The three main components of the WRF-Chem model are the WRF Pre-processing System (WPS), real data initialisation and the WRF ARW solver (including chemistry). These are shown in Figure 2.3, in addition to the components which are specific to this study.

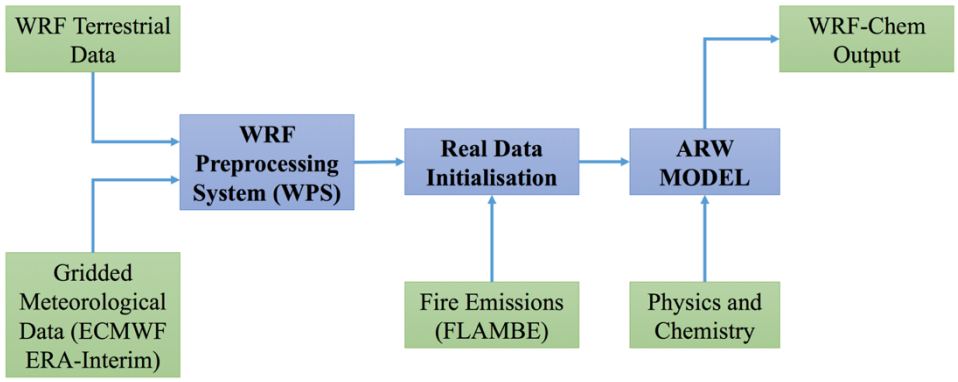


Figure 2.3 Main components and flow chart of the WRF-Chem Modelling system specific to the current study. The blue boxes represent the main components of the modelling system while the green boxes represent the external data relevant to the system.

2.2.2 WRF Pre-processing System (WPS)

The WRF Pre-processing System (WPS) is a set of programs which is used to prepare input data for the real program for real data initialisation. These programs include geogrid, ungrib and metgrib, respectively. Geogrid defines the model domain and interpolates static geographical data to the domain while ungrib extracts meteorological data from Gridded Binary (GRIB) formatted files. Metgrid combines the output from both geogrid and ungrib by horizontally interpolating meteorological data extracted by ungrib onto the model domain defined by geogrid.

Figure 2.4 shows the data flow between the components of WPS. All WPS programs read parameters from a common namelist file (namelist.wps). This file contains separate namelist sections for each of the WPS programs as well as a shared section, which altogether define parameters which are used by the WPS programs. The shared section contains information about the WRF model solver (in this case, ARW), the number of domains to be used in the simulation, the start and end dates of the

simulation, the time resolution of the input meteorological data and the input/output format. The namelist.wps file can be found in Appendix A.

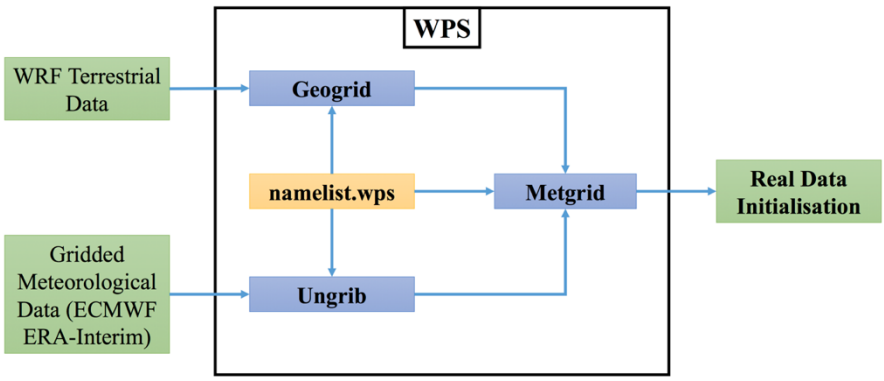


Figure 2.4 Main components of WPS and the data flow between them.

As mentioned above, the purpose of the geogrid program is to define the simulation domains and to interpolate terrestrial data to these domains. This is achieved by defining the domain parameters under the geogrid section in namelist.wps, that is, the number of grid points in the west-east and north-south direction, spatial resolution, map projection, the reference latitude and longitude for the domain, the location and resolution of the static terrestrial data to be used for the simulation. The model supports several conformal projections. In this work, the Mercator projection is used since it best represents the areas next to the equator. The Mercator projection projects the terrestrial sphere on a cylinder with its axis along the North-South Pole axis, such that the meridians are represented by equidistant parallel lines while parallels are represented by parallel line segments which are perpendicular to the meridians. In addition, geogrid also interpolates soil categories, land use category, terrain height, deep soil temperature, vegetation fraction and albedo from global datasets. In this work, 10 and 5 min (approximately 19 and 9 km, respectively) MODIS datasets are used for the model domain and nest. The model domain (d01) used in this study, centred at 6° N, 110° E, and a nest (d02) are shown in Figure 2.1. The coarse domain covers the Peninsular Southeast Asia (PSA), the SCS and the MC while the nest covers Sumatra and Peninsular Malaysia (SPM). The grid details are given in Table 2.2.

Table 2.2 Grid details of the outer domain and nest used in the study.

Domain	Resolution	Grid
d01	27 km	160 x 150
d02	9 km	172 x 172

The next step in setting up the model simulation involves using the ungrib program to read and "degrib" GRIB files and rewriting them in the intermediate format. GRIB files are typically output from other regional or global models. In this study, the meteorological fields in the model are initialised with the European Centre for Medium-range Weather Forecast (ECMWF) ERA-Interim analyses (Berrisford et al., 2009) with a resolution of 0.7° at 6 hour intervals. Typically, GRIB files contain more fields than actually required to initialise WRF. Therefore, the ungrib program uses a variables table called Vtable to extract only the required variables from the GRIB files. 2 sets of ERA-Interim analyses data are downloaded for this study, namely surface data and model level data. The corresponding Vtable, that is, Vtable.ERA-interim.ml, is used by ungrib to extract geopotential, temperature, wind, specific humidity, surface and sea-level pressure, and soil and terrain properties.

Finally, outputs from geogrid and ungrib are combined using the metgrib program. Metgrid horizontally interpolates the meteorological data extracted by ungrib on the model domain defined by geogrid. The output from metgrid is then used by the WRF real program to initialise the simulation. Real data initialisation in WRF-Chem consists of two main steps. First, the model is initialised with meteorological and terrestrial output data from WPS. The emissions required in the model are then prepared so that the emission fields can be included in the initialisation of the model.

2.2.3 Real Data Initialisation

2.2.3.1 Meteorology

The real-data pre-processor in WRF, that is, the program real, generates initial and lateral boundary conditions from the output from WPS. The initialisation process involves the computation of a base state or reference profile for geopotential and column pressure, from which the perturbations are calculated. Real then initialises the meteorological variables u, v, potential temperature and water vapour mixing ratios. The program real also interpolates data to the model's vertical coordinate. WRF uses a terrain-following hydrostatic-pressure vertical coordinate η which is defined as

$$\eta = \frac{p_h - p_{ht}}{p_{hs} - p_{ht}}, \tag{2.6}$$

where p_h is the hydrostatic component of the pressure at a given level in the atmosphere while p_{hs} and p_{ht} refer to values of pressure along the model surface and the top of the

atmosphere, respectively. The mass per unit area within a column in the model, μ, is defined as

$$\mu = p_{hs} - p_{ht}. \tag{2.7}$$

This coordinate system, proposed by Laprise (1992), is also called a mass vertical coordinate. The compressible non-hydrostatic Euler equations integrated by the ARW solver are in fact formulated from this vertical coordinate system. The value of η ranges from 1 at the surface to 0 at the model top. The model used in this work consists of 50 vertical sigma levels with about 12 layers concentrated in the lowest 1km of the atmosphere and a model top set at 50 hPa (approximately 25 km). The corresponding η values can be found in the namelist file required for real data initialisation (namelist.input) in Appendix B.

In addition, the program real vertically interpolates soil properties to the required levels based on the selected land surface scheme to prepare the soil fields in the model. It also verifies that soil categories, land use, land mask, soil temperature and sea surface temperature are consistent with each other. Finally, real generates the lateral boundary conditions which include u, v, potential temperature, water vapour mixing ratio, total temperature along with total column pressure, based on the time periods specified in WPS.

2.2.3.2 Emissions

The transport of biomass burning emissions is a major focus of this work. Therefore, the required biomass burning emissions need to be included in the model after the meteorological initialisation is completed by real. The Fire Locating and Modeling of Burning Emissions (FLAMBE) database is used in this work to specify the smoke emissions in the simulations, based on the parameterizations described by Reid et al. (2009) and Wang et al. (2013). The FLAMBE algorithm estimates the smoke emission flux as a function of the total amount of fuel mass available for combustion, the combustion factor, the average mass fraction of carbon, the total area burned and the $PM_{2.5}$ emission factor. The emission factors used by FLAMBE are based on the review of Reid et al. (2005) while the biomass characteristics are obtained from the land surface database described in Reid et al. (2009). For the study region, FLAMBE derives fire hotspot data from the MODIS Active Fire Hotspot Detection product from Terra and Aqua to estimate near-real-time hourly fire emission. For each fire pixel that MODIS

detects, FLAMBE assumes a fire area of 62.5 ha (0.625 km^2). Since fire detection data are only obtained 3 – 4 times daily over the tropics and mid-latitudes, assumptions need to be made about the lifetime of a satellite-detected fire so that FLAMBE emission data can be used in a chemistry transport model like WRF-Chem. This is because WRF-Chem requires the smoke emission rate as a function of time. Typically, in FLAMBE MODIS fires are assigned a duration of 24 h from the hour of detection and a diurnal cycle is applied so that about 90% of the emissions are released during the day (Reid et al., 2004). In order to match the smoke release timing used in the Navy Aerosol Analysis and Prediction System (NAAPS) transport model (Reid et al., 2009), the FLAMBE estimated smoke emission for each fire is distributed equally within 6h in WRF-Chem. The specification of smoke emission rate within a grid cell area A (m^2) in WRF-Chem in this study follows Wang et al. (2006) and is defined as

$$\left(\frac{\partial C}{\partial t}\right) = \frac{\sum_j F_j}{A \cdot H \cdot \Delta t}, \tag{2.8}$$

where *j* represents the *j*th fire within that grid, *F* is the smoke emission flux (kg) and H is the injection height (m). Δt is 1h since hourly emissions is used. In addition, since the lifetime of a fire is assumed to be 6h, the emission rate for a fire pixel, detected at hour t, is kept constant between t and t + 5 h. The emissions injection height is set at 0.8 km based on the sensitivity studies done by Wang et al. (2013) and it is assumed that the smoke aerosols are uniformly distributed within that height. The FLAMBE smoke emission values are tripled before being integrated in the simulations since FLAMBE emissions have a low bias over the study region (Fisher et al., 2010; Reid et al., 2009; Wang et al., 2006). It is important to note that since the focus of this study is the transport of smoke particles, background aerosols and aerosol radiative feedback are not included in the simulation.

The simulations are initialised at 00UTC on 14 June 2013 and ended at 00UTC on 27 June 2013. The FLAMBE emissions are updated for each day of simulation and the first 3 days of run are considered as spin-up.

2.2.4 Model Physics

The WRF physics options can be categorised as follows: microphysics, cumulus parameterisation, planetary boundary layer (PBL), land-surface model and radiation. These are described below. However, the options selected for the parameterisation of

microphysics, convection and PBL are discussed in Chapter 3, which covers the WRF physics sensitivity studies for the simulations.

Microphysics: The WRF-Chem model includes several microphysics schemes to explicitly resolve water vapour, cloud and precipitation processes. Condensed water particles in the atmosphere exist as a variety of basic species and sizes and are far too numerous to individually track. Therefore, the microphysics schemes which have been developed are either of the spectral or bulk variety. In spectral microphysics schemes, the particle size distribution (PSD) is partitioned into discrete bins, and the evolution of particles through these partitions is modelled. However spectral schemes are computationally demanding. Consequently, bulk schemes are most commonly used, where the PSD for each species is specified separately. Single and double moment microphysics schemes are available in WRF. Single moment schemes predict only the mixing ratios of prognostic species of water (i.e., cloud, ice, rain, snow, graupel and hail) while double moment schemes also predict the number concentrations of these variables in addition to their mixing ratios.

Cumulus Parameterisation: Cumulus parameterisation schemes are responsible for sub-grid scale effects of convective and/or shallow clouds and are intended to represent vertical fluxes due to unresolved updrafts and downdrafts. They operate on individual columns where the selected scheme is triggered and provide vertical heating and moistening profiles. Cumulus parameterisations are usually used for coarse grid sizes (>10 km) where they are required to release latent heat properly on a realistic time scale on the convective columns. They should not be used at grid resolutions of less than 5 km since the model can resolve the convective eddies itself. However, cumulus schemes can help trigger convection at resolutions of 5 – 10 km.

Planetary Boundary Layer (PBL): The PBL scheme is responsible for vertical sub-grid scale fluxes which occur due to eddy transports in the whole atmospheric column. Since the PBL scheme handles the whole atmospheric column and not only the boundary layer, explicit vertical diffusion is deactivated when a PBL scheme is activated. The surface fluxes are provided by the surface layer and land-surface schemes, which are described below. PBL schemes determine the flux profiles within a well-mixed boundary layer and the stable layer, thus providing atmospheric

tendencies of temperature, moisture and horizontal momentum along the whole atmospheric column.

Surface Layer: The surface layer schemes provide the friction velocities and exchange coefficients which are used by the land-surface models and PBL schemes to calculate surface heat and moisture fluxes, and surface stress, respectively. The surface fluxes and surface diagnostic fields over water surfaces are computed in the surface layer scheme itself. Since each surface layer option is tied to a particular PBL scheme, the related surface layer options are also described in Chapter 3.

Land Surface Model: Land surface models use atmospheric information from the surface layer scheme, radiative forcing from the radiation scheme and precipitation forcing from the microphysics and convective schemes, along with internal information on land-surface properties, to provide heat and moisture fluxes over land and sea points. These fluxes in turn provide a lower boundary condition to the PBL scheme so that it may compute the vertical transport. The land surface model updates the land's state variables which include ground temperature, soil temperature profile, soil moisture profile, snow cover and canopy properties. The Noah land surface model (Chen and Dudhia, 2001), jointly developed by NCAR and National Centers for Environmental Prediction (NCEP), is used in the model setup for this work. It is a four-layer (10, 30, 60 and 100 cm from the top down) soil temperature and moisture model and can predict canopy moisture and snow cover. The scheme also includes root zone, evapotranspiration, soil drainage, and runoff, and considers vegetation categories, monthly vegetation fraction and soil texture. In addition, it provides latent heat fluxes to the PBL scheme.

Atmospheric Radiation: Radiation schemes provide atmospheric heating due to radiative flux divergence and surface downward longwave and shortwave radiation for the ground heat budget. Longwave radiation includes infrared or thermal radiation absorbed and emitted by gases and surfaces. The upward longwave radiative flux from the ground is determined by the surface emissivity, which depends on the type of land-use and the ground temperature. Shortwave radiation includes visible and surrounding wavelengths which make up the solar spectrum. The main processes included in the radiation schemes are absorption, reflection and scattering in the atmosphere and at surfaces. The upward flux for shortwave radiation is reflection due to surface albedo.

In the atmosphere, radiation is affected by the presence of model-predicted cloud, water vapour, carbon dioxide, ozone and trace gas concentrations. The new versions of the Rapid Radiative Transfer Model (RRTM) radiation schemes, i.e., the RRTM longwave and shortwave radiation schemes (Iacono et al., 2008) for global climate models (GCMs), RRTMG, are used in this study. The longwave RRTMG scheme is a 16-spectral band scheme which uses the correlated-*k* method and uses pre-set tables to accurately represent longwave processes due to water vapour, ozone, carbon dioxide and trace gases. The scheme also accounts for cloud optical depth. The shortwave RRTMG scheme uses a 14-band spectral method and uses an ozone and carbon dioxide profile like the RRTMG longwave scheme. Both the longwave and shortwave RRTMG scheme include the Monte Carlo Independent Column Approximation (MCICA) method of random cloud overlap which is a statistical method to resolve sub-grid scale cloud variability.

Four-Dimensional Data Assimilation (FDDA): In addition to the above categories of WRF physics, since four-dimensional data assimilation (FDDA) applies extra forcing to the model equations, it is treated in a similar way to physics and is also included in this section. FDDA, also known as nudging, is a method used to keep simulations close to analyses and/or observations during an integration. Two methods of FDDA are available in WRF-Chem, namely, analysis nudging and observation nudging. Analysis nudging forces the simulation towards a series of analyses grid-point by grid-point while observation nudging forces the model simulation towards observational data. Analysis nudging is used in this study to nudge the model towards the ERA-Interim analyses. In this form of FDDA, the model is nudged towards spatially and temporally interpolated analyses using a point-by-point relaxation term. Analysis nudging [*Stauffer and Seaman*, 1990] has several major advantages. Firstly, the model can be run for long periods of time to provide a four-dimensional meteorologically self-consistent dataset that stays on track with the driving analyses. Such datasets are particularly useful when running chemistry models to ensure that wind fields are properly simulated to avoid erroneous transport of chemical species. Secondly, if the outer domain is run with analysis nudging during a nested run, the nest will receive better temporal detail at its boundary as compared to it being directly driven from linearly interpolated analyses. Finally, analysis nudging can be used for dynamic initialisation of the model in order to reduce the spin-up time of the model and allow a smooth start up at forecast time

zero. The four nudged fields in WRF-Chem are the u and v horizontal wind components, temperature and specific humidity. The nudging coefficient controls the strength of nudging. If nudging is too strong, it may offset the mesoscale features created by the model and if it is too weak, the observations may not have any influence on the model state thus allowing the phase and amplitude errors to grow. The nudging coefficient is usually chosen to be small, in the range 0.0001 s^{-1} – 0.0005 s^{-1} for optimum nudging (Yesubabu et al., 2014). Therefore, a nudging coefficient of 0.0003 s^{-1}, corresponding to a timescale of one hour, is used for the present simulations.

2.2.5 Model Chemistry

This section describes the main chemistry settings used to setup the model for this study. The two main components of the model chemistry include the gas phase mechanism and the aerosol scheme. The selection of these settings is based on the works of Sessions et al. (2011), Wang et al. (2013) and Ge et al. (2014), which all use the FLAMBE dataset to simulate the forest fire smoke emissions with WRF-Chem. More importantly, the work of Wang et al. (2013) and Ge et al. (2014) focus on the forest fire emissions over the same model domain as this study.

The Second Generation Regional Acid Deposition Model (RADM2) (Stockwell et al., 1990) gas phase chemistry mechanism and the Modal Aerosol Dynamics Model for Europe with Secondary Organic Aerosol Model (MADE/SORGAM) (Ackermann et al., 1998; Schell et al., 2001) are used to simulate the aerosol processes in the simulations. RADM2 is a state-of-the-art gas phase mechanism that has been extensively used and tested for modelling atmospheric chemistry on a regional scale. The inorganic species in the mechanism include 14 stable species, 4 reactive intermediate, and 3 abundant stable species, namely, oxygen, nitrogen and water. Atmospheric organic chemistry is represented by 26 stable species and 16 peroxy radicals. MADE is an aerosol module in which the size distribution of the sub-micrometre aerosol is represented by two overlapping lognormal modes. It also allows a more detailed treatment of aerosol effects in WRF-Chem, in particular the direct aerosol effect. However, since the focus of this study is the transport of smoke particles, background aerosols and aerosol radiative feedback are not included in the simulation. The aerosol parameterisation used in the model therefore facilitates the inclusion and transport of the $PM_{2.5}$ concentrations provided by the FLAMBE dataset.

3. SENSITIVITY STUDIES AND MODEL EVALUATION

The previous chapter describes the datasets that are key to this study and the WRF-Chem setup for the simulations, including the model domain, the meteorological and emission datasets, and the physics and chemistry parameterisations. However, the model physics are only partly discussed in Chapter 2. The first part of this chapter discusses the WRF sensitivity studies performed to determine the microphysics, cumulus and PBL settings which are most suitable to represent the meteorology over the study domain during the June 2013 haze episode. This is then followed by an evaluation of the WRF-Chem model used to simulate the episode with the same physics settings. The output from the WRF sensitivity studies and WRF-Chem model are evaluated with the datasets described in Chapter 2.

3.1 WRF Sensitivity Study

To simulate haze transport using weather models, it is essential to ensure that the meteorology of that particular event is suitably simulated with minimal error. Not only do the winds which drive the transport of haze, need to be properly simulated, but it is also important that the location and magnitude of convection are correctly parameterised by the model. This is because modelling convection is critical in simulating the vertical transport of haze (Rivière et al., 2006). To this end, sensitivity simulations are run with different physics settings to determine the model set-up which best represents the meteorology over the study region from 17 to 25 June 2013. The nudging settings described in Chapter 2 are kept unchanged for all the simulations. A brief description of the relevant physics options is given in this section.

3.1.1 Physics options

The physics schemes selected for microphysics, cumulus parameterisation and PBL (as well as the corresponding surface layer scheme) in the sensitivity simulations are described in this section. The role of microphysics, cumulus parameterisation and PBL

schemes are also described in Chapter 2. For the sensitivity simulations in this study, the choice of options is based on previous WRF physics sensitivity studies and work which include WRF simulations with domains over Asia and SEA. Particular attention is also given to WRF studies that focus on the prediction of precipitation and TCs. A summary of these studies and the selected microphysics, cumulus parameterisation and PBL options is given in Table 3.1.

A few key points can be highlighted from the studies summarised in Table 3.1. First, the microphysics and cumulus parameterisation schemes have a critical influence on WRF simulated precipitation and cyclone intensity. Taylor (2011) reports that the choice of cumulus parameterisation is critical when simulating the convective transport of biomass burning emissions using WRF-Chem, which is an essential part of this study. In addition, despite the fact that many of the studies in Table 3.1 are performed over Asia and Southeast Asia, the final selection of physical parameterisation varies largely. For instance, both Yu *et al.* (2011) and Choi *et al.* (2015) perform sensitivity studies to investigate the impact of cumulus parameterisation on precipitation in East China. The former finds that a combination of the Grell-Devenyi (GD) (Grell and Dévényi, 2002) cumulus scheme and WRF single-moment 6-class microphysics scheme (WSM6; Hong and Lim, 2006) work best while the later found that a combination of Kain-Fritsch cumulus scheme with an alternative trigger function weighted by moisture advection, KFtr, (Ma and Tan, 2009) and the WRF single-moment 3-class microphysics scheme, WSM3, (Hong et al., 2004) produced the best results. Indeed, model parameters such as domain resolution and boundary conditions can also influence the model output. This essentially highlights the importance of performing sensitivity studies for specific research work since the parameters for each study may vary to a large extent.

Table 3.1 Summary of previous relevant sensitivity studies and precipitation/TC studies involving WRF and WRF-Chem, especially over Asia and Southeast Asia. The optimal WRF microphysics, cumulus and PBL parameterisation settings are also included.

Source	Summary	WRF physics (best performance)		
		Microphysics	**Cumulus Scheme**	**PBL scheme**
(Rajeevan et al., 2010)	WRF was used to simulate the features associated with a severe thunderstorm observed over Gadanki, over southeast India, and its sensitivity to four different microphysical schemes, namely, Thompson (Thompson et al., 2004), Lin (Lin et al., 1983), WRF single-moment 6-class scheme, WSM6, (Hong and Lim, 2006) and Morrison (Morrison et al., 2009), was investigated. While the Thompson scheme simulated the observed features of the updraft/downdraft cores reasonably well, all the four schemes underestimated the strength and vertical extent of the updraft cores. In addition, the Thompson scheme simulated surface rainfall distribution closer to observations while the other three schemes overestimated observed rainfall.	Thompson	Betts–Miller–Janjić (BMJ; Janjić, 2000, 1994)	-
(Chotamonsak et al., 2011)	Projected climate change over Southeast Asia is simulated using WRF. Dynamical downscaling of a global climate model is applied at 60-km horizontal resolution to project changes from 1990–1999 to 2045–2054 of temperature and precipitation over Southeast Asia.	WSM6	BMJ	Yonsei University (YSU)

				(Hong et al., 2006)
(Duda, 2011)	Mesoscale convective systems are studied using both idealised and real data WRF simulations using grid spacings in the range from 0.5 km to 12 km with an emphasis on 3 km to determine the necessity of a convective parameterization scheme. Kain–Fritsch, KF, (Kain, 2004) is used as it is considered to give the best forecasts of precipitation in mesoscale models. The microphysics schemes tested were: Thompson, Morrison, Lin, WSM6, WRF Double Moment 6-class (WDM6; Lim and Hong, 2010), and Eta (Ferrier) (Rogers et al., 2001).	Thompson	KF	Mellor-Yamada-Janjić (MYJ; Janjić, 2002, 1996)
(Raju et al., 2011)	WRF sensitivity studies of physical parameterisations on prediction of tropical cyclone Nargis over the Bay of Bengal are performed. 5 microphysics schemes (Kessler (Kessler, 1969), Lin, Eta, WSM6, Thompson), 3 cumulus schemes (KF, BMJ, Grell-Devenyi ensemble (GD) (Grell and Dévényi, 2002)) and 2 PBL schemes (MYJ and YSU) were used to run 11 different sensitivity simulations. The cyclone tracks and intensity are compared against the Joint Typhoon Warning Center (JTWC) estimates.	Eta	KF	YSU

(Taylor, 2011)	KF, BMJ and GD cumulus schemes were compared to investigate which cumulus parameterisation scheme performed better. Precipitation fields were compared to the Global Precipitation Climatology Project (GPCP). Daily averaged total column CO were also compared against the Atmospheric InfraRed Sounder (AIRS). The results show that the choice of cumulus parameterisation is critical when simulating the convective transport of biomass burning emissions using WRF-Chem.	Lin	KF	YSU
(Wu et al., 2011a)	WRF-Chem was used to simulate the distribution and evolution of aerosol, clouds, precipitation and chemistry during the dry season in South America. The model is evaluated using multiple data sets, mostly from satellite observations. Surface precipitation is also in reasonable agreement with observation. The model simulations overestimate the magnitude of water vapour in the upper troposphere while the magnitude of cloud water content is lower than measurements from satellites, which may indicate problems in the cumulus and microphysical parameterisations.	Lin	GD	MYJ

(Yu et al., 2011)	The BMJ, GD and KF cumulus schemes was used in WRF simulations to investigate the impacts of different cumulus convective parameterisation schemes on summer monsoon precipitation simulation over China. The results show that all the schemes have the capability to reasonably reproduce the spatial and temporal distributions of summer monsoon precipitation and the corresponding background circulation. However, detailed comparison indicates that GD gives a better performance than the others.	WSM6	GD	YSU
(Chotamonsak et al., 2012)	WRF sensitivity studies was performed to simulate precipitation over Thailand for the year 2005. The simulations were run with 4 cumulus schemes, namely, BMJ, GD, G3D (improved GD), and KF, with and without nudging applied to the main domain. Results were evaluated both against station data and gridded observations. In general, the experiments with nudging perform better than un-nudged experiments and the BMJ cumulus scheme with nudging yields the smallest bias relative to observations.	WSM6	BMJ	YSU
(Kumar et al., 2012)	The configuration and evaluation of WRF-Chem simulations of the meteorology over the South Asian region is given. Temperature, water vapour and wind are evaluated against radiosonde and satellite-borne observations.	Thompson	KF	MYJ

(Osuri et al., 2012)	WRF sensitivity studies were performed with different physical parameterisation schemes for the simulation of tropical cyclones over North Indian Ocean. Six combinations of physical parameterisation schemes which include 2 PBL Schemes, YSU and MYJ, and 3 cumulus schemes, KF, BMJ, and GD were employed in WRF to obtain the optimum combination for the prediction of TCs over North Indian Ocean. It was found that the combination of YSU PBL scheme with KF convection scheme (YKF) provides a better prediction of intensity, track, and rainfall consistently.	WRF single-moment 3-class scheme (WSM3; Hong et al., 2004)	KF	YSU
(Wang et al., 2013)	WRF-Chem was used to simulate the transport of smoke particles over the Southeast Asian MC during September–October 2006. Dry conditions during that period were associated to El Niño. Smoke emission is specified according to the FLAMBE and is evaluated with surface PM10 measurements. The interplay of sea/land breezes, typhoons and storms over the subtropical western Pacific Ocean, trade winds, and topographic effects are shown in the model simulation.	WRF single-moment 5-class scheme (WSM5; Hong et al., 2004)	GD	YSU
(Heath and Fuelberg, 2014)	WRF was used to examine regions where convection impacts the Asian summer monsoon anticyclone. The summer monsoon is associated with an upper level anticyclone into which convection can rapidly transport boundary layer air.	Thompson	GD	YSU

(Raktham et al., 2014)	This study evaluated WRF's ability to simulate major weather phenomena over East and Southeast Asia, namely, dry conditions, tropical cyclones (TCs) and monsoonal flow. The sensitivity tests include different cumulus (KF and BMJ) and microphysics (Lin, WSM3, WSM6 and Thompson) schemes which were used together with different placements of lateral boundaries to understand and identify a suitable model configuration for weather and climate simulations over Asia. The dry season showed little sensitivity to any configuration choice, while the TC case showed high sensitivity to the cumulus scheme and low sensitivity to the microphysical scheme.	Lin	KF	-
(Choi et al., 2015)	The capability to simulate the diurnal variation of precipitation over East Asia during the summer of 2011 was investigated using 5 different cumulus parameterisation schemes with WRF. These are KF, BMJ, Simplified Arakawa-Schubert (SAS) scheme (Han and Pan, 2011; Pan and Wu, 1995; Sunny Lim et al., 2014), Tiedtke scheme (TDK; Tiedtke, 1989; Zhang et al., 2011), and Kain-Fritsch scheme with an alternative trigger function weighted by moisture advection (KFtr; Ma and Tan, 2009). The KFtr scheme based on moisture advection provides slightly better results in terms of alleviating the overestimated precipitation rate and frequency and delaying the afternoon peaks.	WSM3	KFtr	YSU

(Patil and Pradeep Kumar, 2016)	WRF sensitivity studies were performed to identify a combination of the best physics options suited for simulating intense western disturbances over North West India. Five experiments were carried out using different microphysics parameterisation schemes, namely, WSM3, WSM5, Eta, Stony Brook University (SBU-YLin; Lin and Colle, 2011) and National Severe Storms Laboratory 1-moment (NSSL 1-momlfo; Gilmore et al., 2004).	NSSL 1-momlfo	KF	YSU
(Zhong et al., 2016)	Two existing emissions inventories, namely, the Regional Emission Inventory in ASia version 2 (REAS) and the Emissions Database for Global Atmospheric Research version 4.2 (EDGAR) were compared in China using WRF-Chem.	Lin	G3D	-

Based on the physics options given in Table 3.1, the following physics options which performed best at predicting convection, and therefore precipitation, are selected for the sensitivity study. Four microphysics schemes (Lin (Lin et al., 1983), WRF single-moment 6-class scheme (WSM6; Hong and Lim, 2006), Thompson (Thompson et al., 2004) and Morrison (Morrison et al., 2005)), three cumulus parameterisation schemes (Kain–Fritsch (KF; Kain, 2004), Betts–Miller–Janjić (BMJ; Janjić, 1994, 2000)) and Grell 3D – an improved version of Grell-Devenyi ensemble (GD; Grell and Dévényi, 2002)) and two PBL schemes (Mellor-Yamada-Janjić (MYJ; Janjić, 1996, 2002) and Yonsei University (YSU; Hong, Noh and Dudhia, 2006)) are chosen. All four selected microphysics schemes are commonly used schemes, which are selected based on their ability to predict precipitation as shown in Table 3.1, as well as the differences between them which include variations in their PSD equations and the number of moments which are computed. The selected cumulus schemes on the other hand use different methods to compute vertical motion, namely, temperature perturbations, entropy change and an ensemble method. While the microphysics and cumulus parameterisation settings are given more attention in the studies summarised in Table 3.1, it can be seen that the two most commonly used PBL settings are MYJ and YSU. Therefore, they are also included in this study. A brief summary of each of these selected options is also given here.

3.1.1.1 Microphysics

Lin (Chen and Sun, 2002; Lin et al., 1983)**:** Six classes of hydrometeors are simulated in this scheme, namely, water vapour, cloud water, rain, cloud ice, snow, and graupel. The scheme uses a 'bulk water' microphysical parameterisation technique to represent precipitation fields, which are all assumed to follow exponential size distribution functions. All the parameterisation production terms are based on Lin et al. (1983) and Rutledge and Hobbs (1984) with some modifications which include saturation adjustment following Tao et al. (1989) and ice sedimentation. The cloud water and cloud ice particles are assumed to be small enough that their terminal velocities can be neglected as compared to the velocity of air, rain, snow and graupel. Rain, snow and graupel possess appreciable terminal velocities and their size distributions, N_r, N_s and N_g are hypothesised as

$$N_r(D_r) = N_{or}\exp(-\lambda_r D_r), \tag{3.1}$$

$$N_s(D_s) = N_{os}\exp(-\lambda_s D_s), \tag{3.2}$$

$$N_g(D_g) = N_{og}\exp(-\lambda_g D_g), \tag{3.3}$$

where N_{or}, N_{os} and N_{og} are the intercept parameters of rain, snow and graupel size distributions, respectively (Chen and Sun, 2002).

D_r, D_s and D_g are the diameters of rain, snow and graupel particles, respectively. λ_r, λ_s and λ_g are the slope parameters of rain, snow and graupel size distributions and are written as

$$\lambda_r = \left(\frac{\pi\rho_w N_{or}}{\rho q_r}\right)^{1/4}, \tag{3.4}$$

$$\lambda_s = \left(\frac{\pi\rho_s N_{os}}{\rho q_s}\right)^{1/4}, \tag{3.5}$$

$$\lambda_g = \left(\frac{\pi\rho_g N_{og}}{\rho q_g}\right)^{1/4}, \tag{3.6}$$

where ρ_w, ρ_s and ρ_g are the densities of rain, snow and graupel, respectively. q_r, q_s and q_g are the mixing ratios of rain, snow and graupel, respectively (Chen and Sun, 2002). The terminal velocities of rain, snow and graupel particles, that is, $U_r(D_r)$, $U_s(D_s)$ and $U_g(D_g)$, respectively are

$$U_r(D_r) = aD_r^b\left(\frac{\rho_o}{\rho}\right)^{1/2}, \tag{3.7}$$

$$U_s(D_s) = cD_s^d\left(\frac{\rho_o}{\rho}\right)^{1/2}, \tag{3.8}$$

$$U_g(D_g) = \left(\frac{4g\rho_g}{3C_D\rho}\right)^{1/2} D_g^{1/2}, \tag{3.9}$$

where $b = 0.8$, $a = 2115 \times 0.01^{(1-b)}$, $d = 0.25$, $c = 152.93 \times 0.01^{(1-d)}$, $\rho_o = 1.29$ kg m^{-3}, and a drag coefficient $C_D = 0.6$ (Chen and Sun, 2002). The mass-weighted mean

terminal velocities of rain, snow and graupel, that is, U_r, U_s and U_g, respectively are obtained by integrating equations 3.7 – 3.9 (Chen and Sun, 2002) and are expressed as

$$U_r = \frac{a\Gamma(4+b)}{6\lambda_r^b}\left(\frac{\rho_o}{\rho}\right)^{1/2}, \tag{3.10}$$

$$U_s = \frac{c\Gamma(4+d)}{6\lambda_s^d}\left(\frac{\rho_o}{\rho}\right)^{1/2}, \tag{3.11}$$

$$U_g = \frac{\Gamma(4.5)}{6\lambda_g^{0.5}}\left(\frac{4g\rho_g}{3C_D\rho}\right)^{1/2}. \tag{3.12}$$

where Γ is the gamma function.

WRF single-moment 6-class scheme (WSM6) (Hong et al., 2004; Hong and Lim, 2006)**:** The 6-class scheme extends the WRF single-moment 3-class (WSM3) and 5-class (WSM5) schemes. WSM3 is a simple-ice scheme which predicts only three categories of hydrometeors: vapour, cloud water/ice and rain/snow. WSM5 on the other hand is a mixed-phase scheme which handles vapour, rain, snow, cloud ice and cloud water in five different ways, allowing supercooled water to exist, and a gradual melting of snow falling below the melting layer. WSM6 extends both schemes by including graupel and its associated processes. The parameterisation of graupel in the scheme is taken from Lin et al. (1983) and therefore WSM6 uses the same equations for graupel as the Lin microphysics scheme. The parameterisation terms in WSM6 are based on Lin et al. (1983) and Rutledge and Hobbs (1983), which diagnose ice number concentrations from cloud temperature without the effect of ice sedimentation. The inclusion of ice processes, in particular, ice sedimentation, is important to prevent too much ice in anvil and cirrus clouds in order to represent the cloud-radiation feedback more realistically (Hong et al., 2004). To include the sedimentation of ice crystals WSM6 adopts the following equation proposed by Heymsfield and Donner (1990) for the mean terminal velocity of falling ice, $\overline{U_I}$, which can be expressed as

$$\overline{U_I} = 3.29(\rho q_I)^{0.16}, \tag{3.13}$$

where ρ is the air density and q_I is the mixing ratio of cloud ice. As the ice crystals fall, they are removed by sublimation, accretion and autoconversion, depending on the environment in which they fall. Also, by taking into consideration the uncertainty in the definition of the ice number concentrations and its effects in ice processes, in WSM6

the cloud ice number concentration is diagnosed from the mixing ratio to more realistically represent the ice microphysical processes. The number concentration of ice nuclei, N_I, can be expressed as

$$N_I = c(\rho q_I)^d, \tag{3.14}$$

where c and d are coefficients depending on the ice crystal habit (Hong and Lim, 2006). Out of the three schemes, that is, WSM3, WSM5 and WSM6, the latter is the most suitable for cloud-resolving grids, considering its efficiency and theoretical backgrounds (Hong and Lim, 2006).

Thompson (Thompson et al., 2008)**:** The Thompson scheme is a single-moment bulk microphysical scheme which includes a large number of improvements to both physical processes and computer coding as compared to earlier single-moment schemes. In addition to explicitly predicting the mixing ratios of cloud water, rain, cloud ice, snow and graupel, this scheme also predicts the number concentration of cloud ice. Therefore, it is a single-moment scheme with the exception of the double-moment cloud ice variable. The Thompson scheme differentiates itself from other WRF microphysics schemes by assuming that each hydrometeor species, except snow, conforms to a generalised gamma distribution instead of an exponential distribution. This gamma distribution, $N(D)$, can be expressed as

$$N(D) = \frac{N_t}{\Gamma(\mu+1)} \lambda^{\mu+1} D^{\mu} e^{-\lambda D}, \tag{3.15}$$

where N_t is the total number of particles in the distribution, D is the particle diameter, λ is the distribution's slope and μ is the shape parameter (Thompson et al., 2008). The distribution becomes the classic exponential distribution when μ = 0. In addition, all water and ice species use the power-law to describe their mass and terminal velocity

(Thompson et al., 2008) as a function of diameter. The mass relation, $m(D)$, is expressed as

$$m(D) = aD^b, \tag{3.16}$$

while the velocity relation, $U(D)$, is given by

$$U(D) = \left(\frac{\rho_o}{\rho}\right)^{1/2} \alpha D^{\beta} e^{-fD}, \tag{3.17}$$

and the values for the constants in equations 3.16 and 3.17 can be obtained from Thompson et al. (2008). Unlike other microphysics schemes, the assumed snow size distribution in this scheme depends on both ice water content and temperature and is represented as a sum of exponential and gamma distributions. The resulting number density function (Field et al., 2005), $N_I(D_I)$, can be expressed as

$$N_I(D_I) = \frac{M_2^4}{M_3^3}\left[\kappa_o e^{-\frac{M_2}{M_3}\Lambda_o D} + \kappa_1 \left(\frac{M_2}{M_3} D\right)^{\mu_s} e^{-\frac{M_2}{M_3}\Lambda_1 D}\right], \tag{3.18}$$

where κ_o, κ_1, Λ_o, Λ_1 and μ_s are constants whose values are provided in Thompson et al. (2008), and M_n is the *n*th moment of the distribution given by

$$M_n = \int D^n N_I(D_I) dD. \tag{3.19}$$

The first term in brackets in equation 3.18 represents an exponential form while the second term represents a gamma function. In addition, in this scheme, snow assumes a non-spherical shape with a bulk density that varies inversely with diameter as compared to nearly all other microphysics schemes which assume spherical snow with constant density. Details about the advantageous features of this scheme can be found in Skamarock et al. (2008).

Morrison (Morrison et al., 2009)**:** The Morrison scheme is based on the two-moment bulk microphysics scheme of Morrison et al. (2005) and Morrison and Pinto (2006). It is an extensively tested scheme which predicts the mass mixing ratios and number concentrations of cloud droplets, cloud ice, rain, snow, and graupel. Since the Morrison scheme is double-moment, it allows for a more robust treatment of the PSDs, which is key for calculating the microphysical process rates and cloud/precipitation evolution. PSDs are treated using gamma functions, with the associated intercept and slope

parameters derived from the predicted mixing ratio and number concentration. These PSDs are expressed as

$$N(D) = N_o D^{\mu} e^{-\lambda D}, \tag{3.20}$$

where N_o, λ and μ are the intercept, slope and shape parameters of the size distribution, respectively, while D is the particle diameter (Morrison et al., 2009). The parameters N_o and λ are derived from the predicted number concentration N and the mixing ratio q, as well as the specified μ for each species, as follows

$$\lambda = \left[\frac{cN\Gamma(\mu+d+1)}{q\Gamma(\mu+1)}\right]^{1/d}, \tag{3.21}$$

$$N_o = \frac{N\lambda^{\mu+1}}{\Gamma(\mu+1)}, \tag{3.22}$$

where Γ is the Euler gamma function and the parameters c and d are given by the assumed power-law mass diameter ($m - D$) relationship of the hydrometeors for each species (Morrison et al., 2009)**,** $m(D)$, where

$$m(D) = cD^{d}. \tag{3.23}$$

Comparing this two-moment microphysics scheme to one-moment bulk microphysics schemes, it produces a much more widespread and prominent region of trailing stratiform precipitation due to reduced rain evaporation rates in the stratiform regions in the two-moment scheme. Conversely increased rain evaporation rates in the convective region at mid-levels which leads to a reduction in the intensity of convective updrafts, are produced in the two-moment scheme as compared to one-moment schemes. The result of these differences in rain evaporation rates between these two types of schemes correspond to surface disdrometer measurements in midlatitude and tropical systems (Morrison et al., 2009)**.**

3.1.1.2 Cumulus parameterisation

Kain–Fritsch (KF) (Kain, 2004)**:** This is a mass-flux type scheme which uses a simple cloud model with moist updrafts and downdrafts, including the effects of detrainment, entrainment, and relatively simple microphysics. A minimum entrainment rate is imposed to suppress widespread convection in marginally unstable, relatively dry environments. In this scheme, shallow convection is allowed for any updraft that does

not reach the minimum cloud depth for precipitating clouds. The downdraft source layer is the entire 150 – 200 mbar deep layer just above cloud base. Finally, detrainment is specified to occur in the updraft source layer and below. The main component of the KF scheme is its convective trigger function. The first task of the scheme is to identify potential source layers for convective clouds, also called, updraft source layers (USLs). The USL in WRF consists of adjacent model layers where the depth of the mixture from the surface is about 60 hPa. The mean thermodynamic characteristics of this mixture and the temperature and height of a parcel of air in this mixture at its lifting condensation level (LCL) are computed through the trigger function. The LCL is the height at which a parcel of air becomes saturated when it is lifted dry-adiabatically. To determine whether convective initiation will take place, the parcel temperature T_{LCL} is compared with the ambient temperature T_{ENV} at the parcel LCL. Since the parcel will typically be colder than its environment, it will be negatively buoyant. Vertical motion will therefore be favoured by background vertical motion, and a temperature perturbation based on the magnitude of grid-resolved vertical motion is assigned to the parcel. This perturbation, δT_{vv} is given by

$$\delta T_{vv} = k[w_g - c(z)]^{1/3} \tag{3.24}$$

where k is a unit number with dimensions K $s^{1/3}$ $cm^{-1/3}$, w_g is an approximate running-mean grid-resolved vertical velocity at the LCL (cm s^{-1}), and $c(z)$ is a threshold vertical velocity given by

$$c(z) = \begin{cases} w_o\,(Z_{LCL}/2000), & Z_{LCL} \leq 2000 \\ w_o\,, & Z_{LCL} > 2000, \end{cases} \tag{3.25}$$

where w_o = 2 cm s^{-1} and Z_{LCL} is the height of the LCL above the ground (m) (Kain, 2004). The use of the above perturbation term allows for computational efficiency since it eliminates most parcels as candidates for deep convection. This elimination process involves adding the computed temperature perturbation to the parcel temperature at the LCL. If the resulting temperature is still less than the environmental value, then this parcel is not considered for deep convection. The test is then repeated for a new potential USL. However, if the resulting temperature is higher than the temperature of the environment, this parcel is considered for deep convection. The parcel is then released at its LCL with its original temperature and moisture content. Its vertical

velocity is however derived from the perturbation temperature. The initial vertical velocity of the parcel, w_{po}, is given by

$$w_{po} = 1 + 1.1[(Z_{LCL} - Z_{USL})\delta T_{vv}/T_{ENV}]^{1/2} \quad (3.26)$$

where Z_{USL} is the height at the base of the USL (Kain, 2004).

Betts–Miller–Janjić (BMJ) (Janjić, 2000, 1994)**:** This scheme is derived from the Betts-Miller (BM) convective adjustment scheme (Betts, 1986; Betts and Miller, 1986) but differs in a few aspects. For instance, the deep convection profiles and the relaxation time are variable and depend on the cloud efficiency (Janjić, 1994). The cloud efficiency is a non-dimensional parameter that characterises the convective regime and it depends on the entropy change, precipitation, and mean temperature of the cloud. In fact, the cloud efficiency is a measure of the ability of the convective column to transport the enthalpy upward while producing as little precipitation as possible. It is required that the entropy change be small and nonnegative so that the shallow convection moisture profile can be derived. In particular, this scheme seeks to improve the production of precipitation as compared to the BM scheme, which produces heavy spurious precipitation over warm water, as well as widely spread light precipitation over oceans. The entropy change is used as a measure of the intensity of convective mixing and the entropy change from cloud top to cloud bottom, ΔS, is given by

$$\Delta S = \sum \left(\frac{c_p \Delta T + L_{wv} \Delta q}{T}\right) \Delta p, \quad (3.27)$$

where Δp are the depths of the model layers in terms of pressure, and c_p and L_{wv} are the specific heat at constant pressure and the latent heat of water vapour transition, respectively (Janjić, 1994). ΔT and Δq represent the changes in temperature and specific humidity, respectively, within a convection time step Δt. T is defined as the mean temperature over that time step. The cloud efficiency parameter, E, is defined as

$$E = K \frac{\bar{T} \Delta S}{c_p \sum \Delta T \Delta p}. \quad (3.28)$$

where K is a nondimensional constant and $\bar{T}$ is the mean temperature of the cloud (Janjić, 1994). The expression $c_p \sum \Delta T \Delta p$ is proportional to the single time-step precipitation denoted as ΔP_B. Equation 3.28 shows that the cloud efficiency is

proportional to the mean cloud temperature and the entropy change, but is inversely proportional to the single time-step precipitation.

Grell 3D (G3D)– an improved version of Grell-Dévényi ensemble (GD) (Grell and Dévényi, 2002)**:** This cumulus scheme is a mass-flux type scheme which is derived from the Grell-Dévényi scheme. While G3D also uses an ensemble mean approach, the quasi-equilibrium approach is no longer included among the ensemble members. The main components of this ensemble approach are static control, feedback and dynamic control. Static control refers to the cloud model that is used to determine the cloud properties, feedback refers to the modulation of the environment by convection and dynamic control relates to the modulation of the convection by the environment. The model-cloud properties such as normalised mass flux, normalised condensation and evaporation profiles, moist static energy, and liquid water content for and ensemble type α are determined from the following entrainment hypothesis

$$\mu_{ue}(z,\alpha) - \mu_{ud}(z,\alpha) = \frac{1}{m_u(z,\alpha)} \frac{\delta m_u(z,\alpha)}{\delta z}, \tag{3.29}$$

where μ_{ue} is the gross fractional entrainment rate, μ_{ud} is the gross fractional detrainment rate and m is the mass flux (Grell and Dévényi, 2002). The subscript u in each term designates an updraft property. The mass flux for an updraft property u is given by

$$m_u(z,\alpha) = m_b(\alpha)\eta_u(z,\alpha). \tag{3.30}$$

where m_b is the mass flux at cloud base and η_u is the normalised mass flux (Grell and Dévényi, 2002). In order to determine the cloud base mass flux, the G3D scheme employs closures that exist in the literature, namely, Arakawa and Schubert (1974), Brown (1979), Krishnamurti et al. (1983) and Kain and Fritsch (1992). The relevant equations are listed in Grell and Dévényi **(**2002**).** The G3D scheme also allows subsidence effects to be spread to neighbouring grid columns, thus making it more suitable for grid sizes which are less than 10km, as compared to other cumulus schemes

which lack this function. G3D can also be used for larger grid sizes where subsidence occurs within the same grid column as the updraft.

3.1.1.3 Planetary boundary layer (PBL)

Yonsei University (YSU) (Hong et al., 2006)**:** This scheme uses the counter-gradient terms to represent fluxes due to non-local gradients in addition to the explicit treatment of the entrainment layer at the PBL top. The turbulent diffusion equation is given by

$$\frac{\delta C}{\delta t} = \frac{\delta}{\delta z}\left[K_c\left(\frac{\delta C}{\delta z} - \gamma_c\right) - (\overline{w'c'})_h\left(\frac{z}{h}\right)^3\right] \tag{3.31}$$

where C is the diagnosed variable, K_c is the eddy diffusivity, γ_c is a correction to the local flux to account for the effect of the large eddies, h is the PBL height, $(\overline{w'c'})_h$ is the flux at height h and z is height from the surface (Hong et al., 2006). The term on the right is the entrainment flux which is made proportional to the surface buoyancy flux while the PBL top is defined using a critical bulk Richardson number. Therefore, the PBL top is dependent on the buoyancy profile, in which the PBL top is defined at the maximum entrainment layer. A smaller magnitude of the counter-gradient mixing in the YSU scheme produces a well-mixed boundary-layer profile. The surface layer scheme used in conjunction with YSU is the MM5 Similarity Theory scheme which uses stability functions from Paulson (1970), Dyer and Hicks (1970) and Webb (1970) to compute surface exchange coefficients for heat, moisture, and momentum.

Mellor-Yamada-Janjić (MYJ) (Janjić, 2002, 1996)**:** This scheme parameterises turbulence in the PBL and in the free troposphere by implementing the Mellor-Yamada Level 2.5 turbulence closure model (Mellor and Yamada, 1982) through a full range of atmospheric turbulent regimes. An upper limit which depends on the turbulent kinetic energy (TKE) which is denoted by $q^2/2$, and the buoyancy and shear of the driving flow, is imposed on the master length scale. In the unstable range, the functional form of the upper limit is derived from the requirement that the TKE production be non-singular in the case of growing turbulence while in the stable range, the upper limit is derived from the requirement that the ratio of the variance of the vertical velocity deviation and TKE cannot be smaller than that corresponding to the regime of vanishing turbulence. Within the PBL, that is, $z \leq h$, the master length scale (denoted by l) is estimated using the following diagnostic formula

$$l = \frac{l_0 \kappa z}{\kappa z + l_0}, \tag{3.32}$$

where

$$l_0 = 0.25 \frac{\int_0^h |z| q dz}{\int_0^h q dz}, \tag{3.33}$$

and κ is the von Karman constant (Janjić, 2002). Above the PBL, that is, $z > h$, l is computed as a fraction of the vertical grid size Δz using

$$l = 0.23 \Delta z. \tag{3.34}$$

The TKE production/dissipation differential equation is solved iteratively over a time step. The Eta surface layer scheme (Janjić, 2002, 1996), based on the similarity theory (Monin and Obukhov, 1954), is used in conjunction with MYJ. The viscous sub-layer in the scheme is parameterised explicitly based on (Janjić, 1994), over water while over land, the effects of the viscous sub-layer are considered through the variable roughness height for temperature and humidity as proposed by Zilitinkevich (1995).

3.1.2 Cases

Table 3.2 shows the simulation cases that are run for this sensitivity study. The sensitivity study includes a set of 13 simulation combinations. The model physics, other than microphysics, cumulus parameterisation and PBL are all kept the same. These settings are summarised in Chapter 2. All simulations are initialised at 00UTC on 14 June 2013 and end at 00UTC on 27 June 2013, and are run for the outer domain only. It takes approximately 12 – 18 hours for WRF-Chem to spin up (Wang et al., 2009). Therefore, to provide realistic initial conditions in the simulations, the first three days of simulation are considered as spin-up. To ensure that the model satisfies the Courant-Friedrichs-Levy (CFL) stability criterion (Courant *et al*., 1928) the time step for all the simulations is set at 90 s (less than the recommended maximum of 6 × grid spacing). The model results are output every hour.

Table 3.2 Cases for sensitivity simulations. For each case name, 'SS' stands for 'Sensitivity Study'.

Cases	Microphysics	Cumulus Parameterisation	PBL
SS01	Morrison	G3D	MYJ
SS02	Morrison	KF	MYJ
SS03	Morrison	BMJ	MYJ
SS04	Lin	G3D	MYJ
SS05	Lin	KF	MYJ
SS06	Lin	BMJ	MYJ
SS07	Thompson	G3D	MYJ
SS08	Thompson	KF	MYJ
SS09	Thompson	BMJ	MYJ
SS10	WSM6	G3D	MYJ
SS11	WSM6	KF	MYJ
SS12	WSM6	BMJ	MYJ
SS13	Lin	BMJ	YSU

3.1.3 Results and Discussion

The sensitivity simulations are evaluated by comparing the simulation results to CMORPH precipitation data and observed data from ground stations over Malaysia. First, the co-located WRF accumulated precipitation for each sensitivity simulation was compared to CMORPH accumulated precipitation for the period 17 to 25 June 2013 as shown in Figure 3.1. The corresponding statistics, that is mean, standard deviation and mean bias are given in Table 3.3. The mean bias is selected as it provides information on the overestimation/underestimation of mean precipitation over the domain (Kumar et al., 2012).

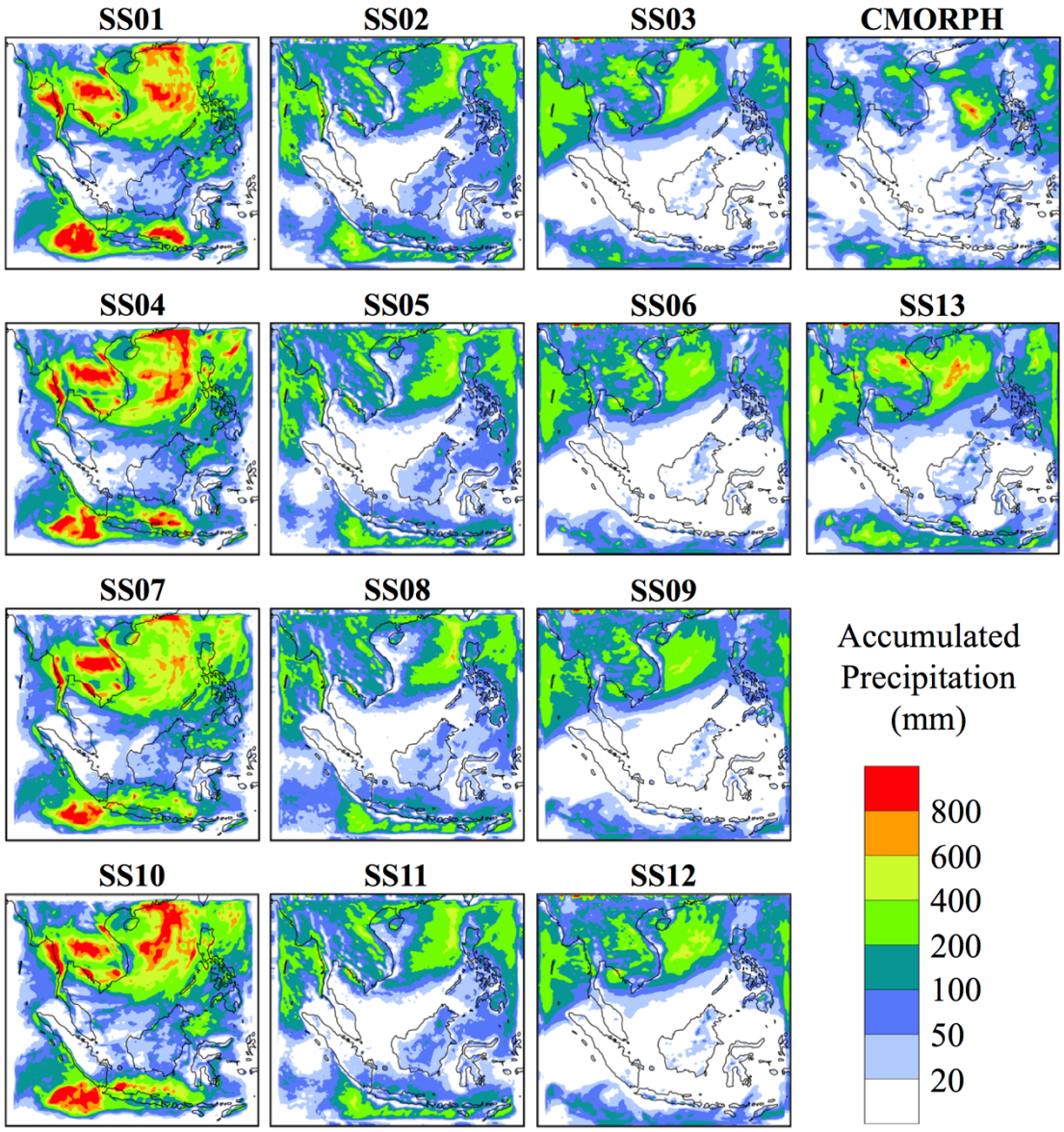


Figure 3.1 Co-located accumulated precipitation (mm) for sensitivity simulations SS01 to SS13 and CMORPH for the period 17 to 25 June 2013.

The domain wide mean value for accumulated precipitation recorded by CMORPH is 60.6 mm. SS06 performed best with a domain wide mean of 73.8 mm of accumulated precipitation for the period 17 – 25 June 2013 and a mean bias of only 13.2 mm as compared to CMORPH. In contrast, SS01 performs the worst with a mean of 197.7 mm and a difference of 137.2 mm. In general, simulations run with G3D cumulus parameterisation highly overestimate precipitation throughout the domain, overestimating the accumulated precipitation for the study period by at least 400 mm over the SCS and the top half of the domain in general, as well as south of Sumatra. Simulations run with KF and BMJ outperform all simulations run with G3D and

showed similar distribution of accumulated precipitation. This suggests that KF and BMJ perform better at a relatively coarse resolution of 27 km over the study region, despite the ensemble nature of G3D and its ability to perform at both fine and coarse resolutions. However, a slight westward phase shift in intensity can be observed for KF and BMJ simulations, even though simulations run with BMJ performed better than simulations run with KF. KF simulations tend to overestimate precipitation south of Sumatra and underestimate precipitation on the left edge of the domain, suggesting that KF does not perform very well near the domain edges as compared to BMJ. BMJ was also reported to simulate precipitation with better accuracy than KF and G3D at 30 km grid resolution (Pennelly et al., 2014). In addition, the results in Pennelly et al. (2014) indicate a similar phase shift in intensity with the KF scheme at 30 km resolution, which does not occur when simulations are run with a grid resolution of 15 km. This suggests that the phase shift in intensity in the sensitivity simulations occurred as a result of the relatively coarse grid resolution of 27 km. The better prediction of precipitation by the BMJ scheme over the ocean can be explained by the use of the cloud efficiency parameter as explained in the description of the scheme.

Changing the microphysics scheme did not seem to have much effect on accumulated precipitation, even though simulations run with Lin and Thompson generally performed better and had smaller Mean Bias as compared to simulations run with Morrison and WSM6 as shown in Table 3.3. Comparing SS01, SS04, SS07 and SS10, noticeable differences in intensities can be observed due to the change in microphysics settings. In particular, precipitation intensities over the SCS with the Thompson scheme were more comparable to CMORPH as compared to the other microphysics schemes. This may be due to the incorporation of relationships of PSD moments and air temperature which are based upon over 9000 observed samples of ice spectra in various synoptic environment, which help improve the prediction of precipitation (Thompson et al., 2008). In contrast, the use of the double-moment Morrison scheme produces the largest bias when comparing all simulations run with different microphysics schemes, despite its ability to predict the number concentration of cloud species in addition to their mixing ratios, thus highlighting its inadequacy for use in the study region.

To compare data from selected air quality monitoring stations over Malaysia, the respective grid index corresponding to the geographic location of each station is first determined. The model value of the required variables at the estimated grid index is

then calculated by bilinear interpolation from the surrounding four model grid points. Tables 3.4 and 3.5 show the comparison between hourly 10 m wind speed and 2 m temperature recorded at 4 of the 52 air quality monitoring stations operated by DOE Malaysia, namely Johor (CAS 019; 1.495°N, 103.736°E), Terengganu (CAE 034; 5.308°N, 103.120°E), Perak (CAN 041; 4.201°N, 100.664°E) and Kuala Lumpur (CAC 058; 3.212°N, 101.682°E) and the model. These four stations are selected since they are sparsely located over Peninsular Malaysia as follows; south, east, north and west regions respectively. The location of each station is shown in Figure 3.2. The metrics used in the analysis are the coefficient of determination (r^2) and root mean square error (RMSE).

Table 3.3 Mean, standard deviation and mean bias of sensitivity simulations accumulated precipitation as compared to CMORPH for 17 to 25 June 2013.

Accumulated precipitation (17 – 25 June 2013)	**Mean**	**Standard Deviation**	**Mean Bias**
CMORPH	60.6	73.8	-
SS01	197.7	248.4	137.2
SS02	91.4	96.9	30.8
SS03	84.4	105.7	23.9
SS04	189.7	247.4	129.2
SS05	86.2	91.4	25.7
SS06	73.8	94.9	13.2
SS07	174.9	215.2	114.4
SS08	83.5	90.6	22.9
SS09	74.3	92.9	13.7
SS10	194.1	247.4	133.5
SS11	88.2	95.6	27.6
SS12	76.2	98.8	15.6
SS13	109.3	128.6	48.8

Among the simulations run with BMJ, SS06 has higher correlations at Terengganu (0.52) and Kuala Lumpur (0.59) while better correlations are obtained at Johor (0.78) and Perak (0.39) for SS09. In addition, only simulations run with BMJ produced relevant correlations when comparing wind speed to data recorded at Perak as shown in Table 3.4. However, comparing RMSEs for SS06 and SS09, RMSEs for SS06 are either smaller or equal to those of SS09. Therefore, SS06 performs best at simulating wind speed among all simulation cases. With respect to microphysics, no distinguishable patterns can be observed when comparing wind speed data.

Table 3.4 Comparison of hourly observed and model simulated 10m wind speed (m s^{-1}) at Johor, Terengganu, Perak and Kuala Lumpur.

Station	**Johor (CAS 019)**		**Terengganu (CAE 034)**		**Perak (CAN 041)**		**Kuala Lumpur (CAC 058)**	
Metrics	r^2	RMSE	r^2	RMSE	r^2	RMSE	r^2	RMSE
SS01	0.49	2.4	0.45	3.2	0.00	3.1	0.45	1.5
SS02	0.55	1.7	0.28	1.1	0.22	1.2	0.57	1.1
SS03	0.65	1.0	0.36	1.6	0.27	1.6	0.5	1.8
SS04	0.56	2.6	0.34	3.3	0.00	2.7	0.59	1.6
SS05	0.61	1.6	0.29	1.2	0.08	1.5	0.50	1.3
SS06	0.76	1.3	0.52	1.4	0.37	1.3	0.59	1.4
SS07	0.52	2.7	0.39	3.4	0.01	2.4	0.56	1.5
SS08	0.60	1.7	0.30	1.2	0.04	1.4	0.56	1.1
SS09	0.78	1.4	0.38	1.4	0.39	1.4	0.46	1.7
SS10	0.52	2.7	0.35	3.1	0.00	2.6	0.55	1.6
SS11	0.61	1.6	0.29	1.1	0.07	1.4	0.50	1.2
SS12	0.73	1.3	0.52	1.4	0.30	1.4	0.46	1.7
SS13	0.61	1.1	0.19	1.2	0.05	1.7	0.46	1.3

Table 3.5 shows the comparison of hourly simulated temperature for all sensitivity simulations with ground station data. In general, all simulations perform well at simulating hourly temperature at all stations. All KF simulations perform best at Johor with the best correlation values and smallest RMSEs. Three of the BMJ simulations (except SS03) perform best at Terengganu with the best correlation values and smallest RMSEs. SS06 performs best at Perak with an r^2 value of 0.80 and RMSE of 1.7 °C. All

simulations perform very well at Kuala Lumpur with correlations of at least 0.83 and highest RMSE of 1.4 °C. Overall simulations run with KF seem to represent temperature better performing best over Johor as well as Kuala Lumpur. SS11 produces the best results overall with an r^2 value of 0.91 and RMSE of 0.9 °C over Kuala Lumpur. However, BMJ simulations (SS06 and SS12) perform best over Perak and Terengganu.

Table 3.5 Comparison of hourly observed and model simulated 2m temperature (°C) at Johor, Terengganu, Perak and Kuala Lumpur.

Station	**Johor (CAS 019)**		**Terengganu (CAE 034)**		**Perak (CAN 041)**		**Kuala Lumpur (CAC 058)**	
Metrics	r^2	RMSE	r^2	RMSE	r^2	RMSE	r^2	RMSE
SS01	0.71	1.5	0.81	1.2	0.39	2.0	0.83	1.4
SS02	0.77	1.3	0.81	1.3	0.80	1.8	0.88	1.0
SS03	0.64	1.6	0.80	1.4	0.71	1.8	0.87	1.1
SS04	0.75	1.3	0.74	1.9	0.55	1.9	0.87	1.0
SS05	0.81	1.1	0.80	1.4	0.74	1.8	0.90	0.9
SS06	0.73	1.3	0.86	1.2	0.80	1.7	0.89	0.9
SS07	0.75	1.3	0.71	2.0	0.55	1.9	0.87	1.1
SS08	0.81	1.1	0.83	1.4	0.79	1.8	0.90	0.9
SS09	0.74	1.3	0.85	1.3	0.79	1.7	0.90	0.9
SS10	0.76	1.3	0.71	1.8	0.56	1.9	0.88	1.0
SS11	0.81	1.1	0.80	1.4	0.77	1.8	0.91	0.9
SS12	0.72	1.4	0.87	1.1	0.77	1.7	0.88	1.0
SS13	0.72	1.3	0.85	1.0	0.66	1.9	0.86	1.1

Considering sensitivity simulations SS01 to SS12 which are all run with the MYJ PBL scheme, SS06 performs best at predicting accumulated precipitation and wind speed. It also performs very well at predicting 2 m temperature. Therefore, the microphysics and cumulus parameterisation settings for SS06, that is, Lin microphysics scheme and BMJ cumulus scheme are selected for further analysis. To determine which PBL scheme performed best, an additional run, SS13 is run with the same physics settings as SS06, except for PBL scheme. SS13 is run with YSU PBL scheme. Figure 3.1 shows that SS13 produces precipitation over the same regions as SS06 but largely over-predicts accumulated precipitation as compared to CMORPH with a wetter bias than SS06. In

fact, the domain wide mean accumulated precipitation for SS13 is 109.3 mm, as compared to SS06 and CMORPH which produces 73.8 mm and 60.6 mm of accumulated precipitation respectively, as shown in Table 3.3. A previous study (Que et al., 2016) which compares different physics schemes in WRF over the Asian summer monsoon region also shows that MYJ reproduces a better distribution of rain belts as compared to YSU which strongly overestimates precipitation intensity. Comparing the predicted wind speed, while SS13 produces smaller RMSEs in general as compared to SS06, wind speeds produced by SS06 are more highly correlated to observations. For instance, the r^2 value at Perak is 0.37 for SS06 while SS13 wind speeds do not correlate with the observations. Finally, SS06 out-performs SS13 at predicting 2 m Temperature at all 4 stations. Therefore, the physics options used for SS06 are used in the WRF-Chem model to simulate biomass burning haze from Sumatra over the model domain. The WRF-Chem model used in this study is evaluated in the following section.

3.2 WRF-Chem Model Evaluation

The performance of the WRF-Chem model used in this study is evaluated by comparing the model results to CMORPH precipitation data, observed data from ground stations and satellite data from the CALIPSO and MODIS satellites. The variables considered for the meteorological evaluation of the model are the same as those used for the sensitivity simulations evaluation. Firstly, the co-located WRF-Chem accumulated precipitation is compared to CMORPH accumulated precipitation for the period 17 to 25 June 2013 as shown in Figure 3.2. Comparing Figures 3.2(a) and (b), overall, WRF-Chem successfully captures the location and magnitude of precipitation over the northern domain area, but with a slight westward phase shift in intensity, as is the case with SS06 in the previous section. However, slight differences in precipitation intensity can be observed between SS06 and WRF-Chem and the corresponding domain wide mean accumulated precipitation were 73.8 mm and 75.0 mm, respectively. This indicates that the inclusion of the Chemistry module in WRF can affect the prediction of meteorology, even though negligible. Here it results in a difference in precipitation of 1.6%.

Since the model is nudged to ERA-Interim analyses, a plot of ERA-Interim accumulated precipitation is included in Figure 3.2(c). While ERA-Interim successfully captures the overall location of precipitation patterns, it fails to capture the regions of

high precipitation over the SCS as compared to CMORPH and WRF-Chem. This indicates that the cumulus parameterisation in WRF-Chem is able to resolve convection over the model domain. While ERA-Interim underestimates precipitation over the SCS and Peninsular SEA, it overestimates precipitation over the MC. The mean accumulated precipitation for CMORPH and ERA-Interim are 60.6 mm and 69.2 mm, respectively. CMORPH, WRF-Chem and ERA-Interim all show that while precipitation prevails over the northern half of the domain, a distinct region of dryness can be observed over Peninsular Malaysia, Sumatra and Borneo. This precipitation pattern is indeed characteristic of the southwest summer monsoon (SWM) season (Chang et al., 2005; Moron et al., 2009; B. Wang et al., 2009), as it is later described in Chapter 4. The WRF-Chem model 10 m wind speed and 2 m temperature are evaluated using the method used in Section 3.1. The model successfully reproduced the diurnal variation of both variables at all 4 stations for the period of 17 – 25 June 2013 as shown in Figures 3.2 (d–g). However, WRF overestimates the magnitude of the model wind speed at all four stations. While sensitivity tests performed by Kwun et al. (2009), Menendez et al. (2014) and Santos-Alamillos et al. (2013) show that the PBL schemes play a major role in simulating surface winds, WRF has been found to have the tendency to overestimate wind speed (Cheng and Steenburgh, 2005; Jiménez and Dudhia, 2012; Mass and Ovens, 2011). This particularly occurs in areas of complex terrain where topographic features cannot be explicitly considered by the coarse resolution of the model. This implies that smoother orography underestimates the terrain roughness, which eventually leads to an excess of wind speed (Gómez-Navarro et al., 2015). Therefore, the overestimation of the 10 m wind speed in this study can be attributed to the relatively coarse 27 km resolution of the domain. Nevertheless, for 10 m wind speed, the highest correlation, $r^2 = 0.98$, is observed at the Johor station while the lowest r^2, recorded over Kuala Lumpur, is at least 0.80. The lowest root mean square error (RMSE), RMSE = 1.0 ms^{-1} was recorded at Perak. The highest correlation and lowest RMSE for 2 m temperature, are also observed at Perak and were $r^2 = 0.96$ and RMSE = 0.7 °C, respectively. The respective correlations and RMSEs for each station are shown at the bottom of each figure in Figures 3.2 (d–g).

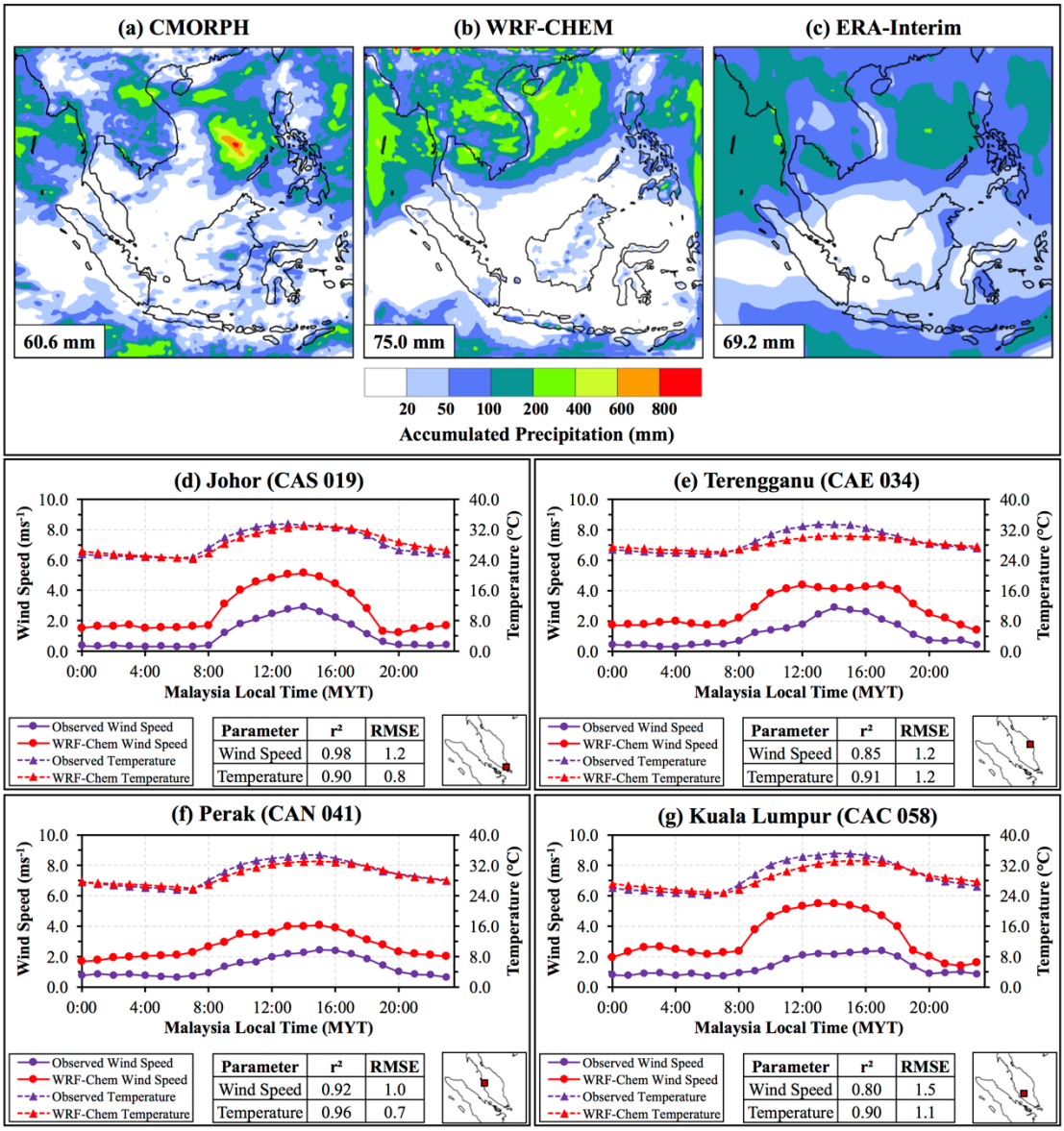


Figure 3.2 Meteorological evaluation for the period 17 to 25 June 2013. Co-located accumulated precipitation (mm) from (a) CMORPH (b) WRF-Chem and (c) ERA-Interim. The mean accumulated precipitation values are shown at the bottom left corner of each plot. Comparison of hourly averaged observed and model simulated 10m wind speed (m s^{-1}) and 2m temperature (°C) at (d) Johor, (e) Terengganu, (f) Perak and (g) Kuala Lumpur. The solid red square on each inset map shows the location of each corresponding site.

The smoke emissions produced by the model are evaluated by comparing the AOT, aerosol vertical profile and smoke mass concentration at selected ground stations as shown in Figures 3.3 and 3.4. The AOT at 550 nm simulated by the model is compared to retrievals from MODIS Terra satellite for 20 – 25 June 2013 in Figure 3.3 (a–b). Figure 3.3 (a–b) shows that the model succeeded at producing similar patterns and magnitudes of AOT over the MC. However, it is important to note that the MODIS AOT retrieval in Figure 3.3(a) is an aggregation of six days of individual retrievals from MODIS Terra. These aggregates contain missing cells of AOT data for the model

domain, particularly for very high AOT smoke in which the retrieval fails. This explains the relatively low AOT values retrieved from MODIS Terra as compared to the model. Observed AOT over the domain are at least 2.4 while the WRF-Chem simulations produced AOTs of at least 3 over the corresponding regions. Overall it is clear from both MODIS AOT and the simulated AOT that smoke is being transported in a northeasterly direction towards the SCS. The WRF-Chem simulated $PM_{2.5}$ emissions on 24 June 2013 at 07:00 UTC extracted along the corresponding CALIPSO track are then compared with CALIOP-derived extinction coefficient at 532 nm as shown in Figures 3.3(c–d). Both plots show that the smoke particles are confined to within 3 km in height along the CALIPSO track. The model also successfully captures the variations in plume height as shown by the plume peaks between latitudes 1°S and 2°N, and 4°N and 7°N. The plume peaks in these two regions reached 3 km in height.

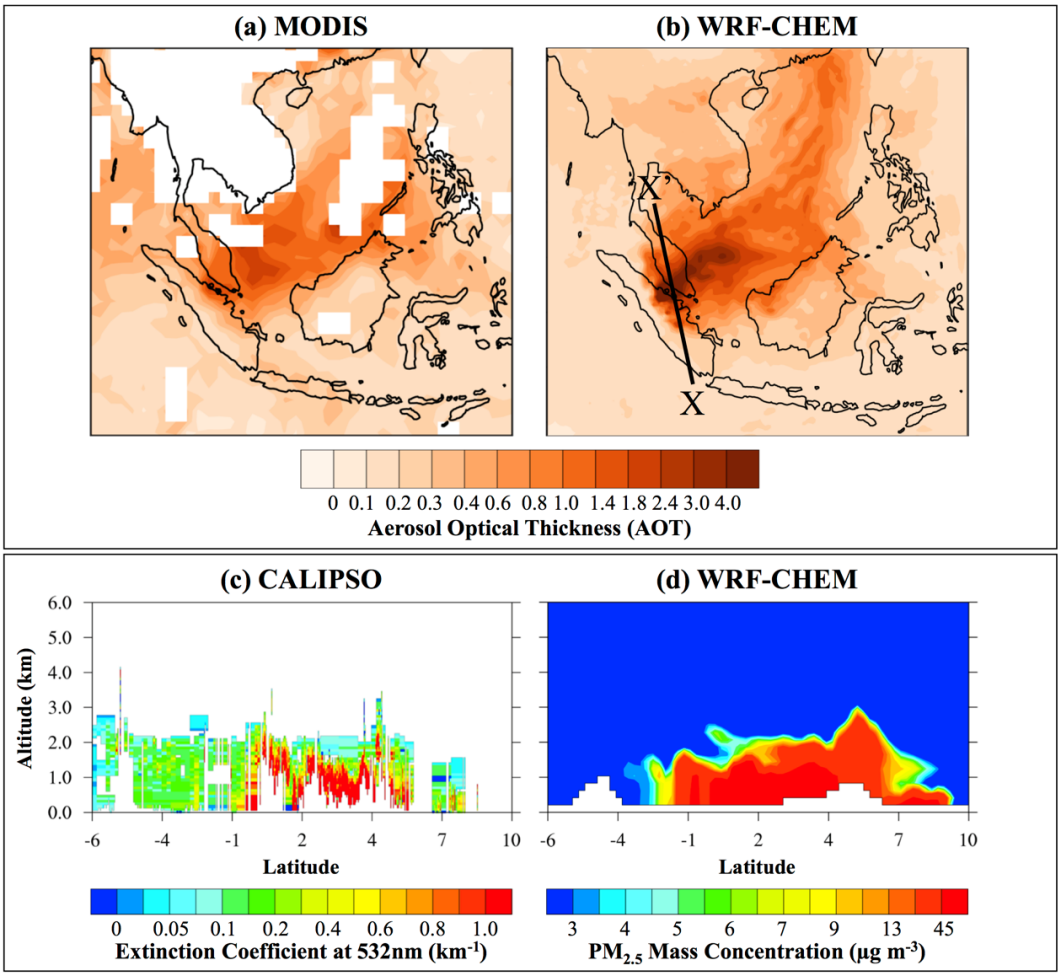


Figure 3.3 AOT at 550 nm, from 20 to 25 June 2013 over the MC from (a) MODIS Terra and (b) WRF-Chem simulations. Also, the comparison of (c) CALIOP-derived vertical profile of extinction coefficient at 532 nm with (d) the WRF-Chem simulated vertical profile of $PM_{2.5}$ smoke concentration along the corresponding portion of the CALIPSO ground track on 24 June 2013. The ground track is indicated by the line XX' on (b).

The $PM_{2.5}$ concentrations produced by the model are also evaluated by comparing the model hourly $PM_{2.5}$ concentrations and the hourly PM_{10} concentrations measured at Melaka (CAS 006; 2.259°N, 102.173°E), Muar (CAS 044; 2.062°N, 102.593°E), Seremban (CAC 047; 2.724°N, 101.968°E) and Cheras (CAC 054; 3.106°N, 101.718°E) ground stations over Malaysia. Since air quality monitoring stations in Malaysia only record PM_{10} concentrations, the model produced $PM_{2.5}$ can only be evaluated with PM_{10} concentrations. In addition, Wang et al. (2013) also evaluated the WRF-Chem modelled $PM_{2.5}$ with measured PM_{10} from ground stations over Malaysia, owing to the same limitation. Figure 3.4 shows the corresponding concentration plots for 20 – 26 June 2013. API readings obtained from the Malaysian DOE (Department of Environment Malaysia, 2013b) indicate that the haze episode became apparent on 15 June when API readings were first categorized as 'Unhealthy' in Melaka City and Muar during that period. 'Hazardous' readings were first recorded on 20 June in Muar while Melaka City was hit with readings reaching 415 on 23 June. In fact, the highest API reading of 746 was recorded on 23 June at Muar. 'Moderate' readings were then recorded on 24 and 25 June in these two most affected cities. During these two days, high 'moderate' readings were also recorded over Seremban and Cheras. Hence, PM_{10} concentrations measured at the above four cities are selected for comparison with the modelled $PM_{2.5}$ concentrations. Since $PM_{2.5}$ and PM_{10} represent fine and coarse particles respectively, only a qualitative comparison is performed to show the diurnal variation of their respective concentrations. In general, the model succeeded at reproducing the diurnal variation of smoke concentration at all four stations as well as the higher concentrations recorded at Melaka and Muar and the comparatively lower concentrations recorded at Seremban and Cheras.

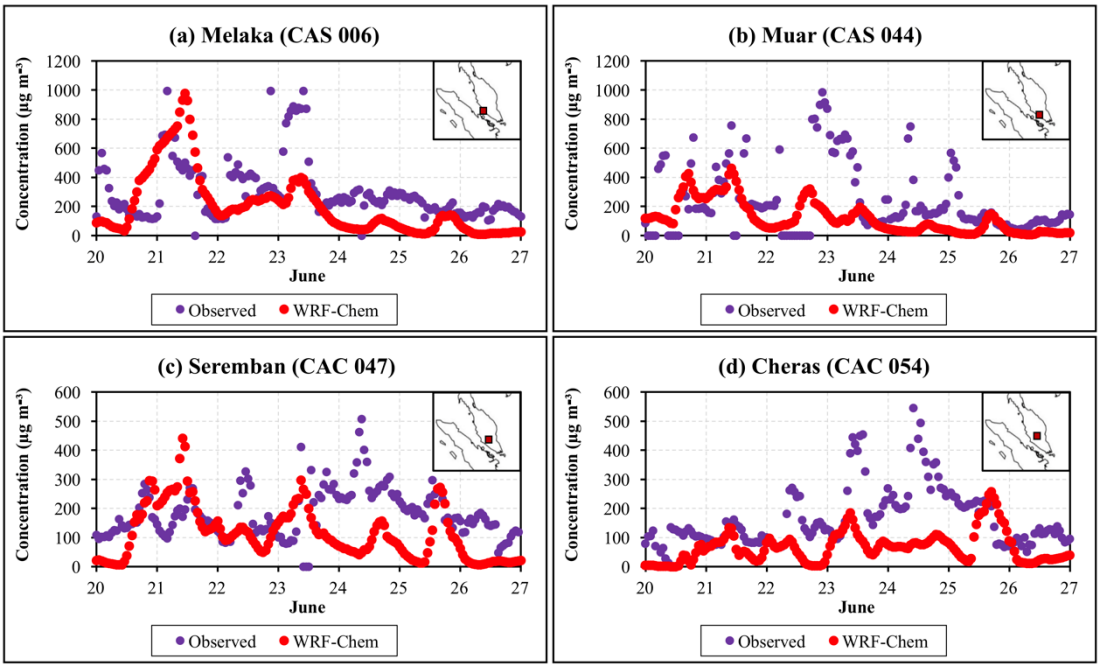


Figure 3.4 Comparison between hourly WRF-Chem simulated smoke (PM_{25}) concentrations near the surface and PM_{10} concentration at (a) Melaka, (b) Muar, (c) Seremban and (d) Cheras. The solid red square on each inset map shows the location of each corresponding site.

3.3 Summary

This chapter presents the sensitivity studies performed to identify the WRF physics settings which best represent the meteorology over the model domain during the June 2013 haze episode. It also includes the evaluation of the WRF-Chem model used to simulate haze transport during that episode.

The physics schemes investigated for the sensitivity study are microphysics, cumulus parameterisation and PBL. The physics options used in the sensitivity simulations are selected based on previous WRF physics sensitivity studies and work which include WRF simulations with domains over Asia and SEA as well as WRF studies related to precipitation and TCs. A set of 13 simulations (SS01 – SS13) are designed from the selected schemes for the sensitivity study and the results are compared for 17 to 25 June 2013.

The output from the sensitivity simulations are evaluated with CMORPH precipitation data and observed data from ground stations over Malaysia. When comparing accumulated precipitation, simulations run with BMJ are found to outperform all simulations run with G3D and produce better accumulated precipitation than KF simulations as well, even though KF performed better than G3D simulations. Changing

the microphysics settings do not seem to have much effect on accumulated precipitation. Comparing modelled 10 m wind speed to ground station data, G3D simulations perform worst once again, having the highest RMSEs at most stations and showing no correlation at some. BMJ simulations perform best with at least one of its simulations having the highest correlation at all the four stations. In contrast, the choice of microphysics scheme does not have much effect on the prediction of 10 m wind speed. Comparing 2 m temperature, all simulations perform very well at all stations. Among cases SS01 to SS12, SS06 which is run with the Lin microphysics, BMJ cumulus scheme and MYJ PBL scheme performs best. To determine which PBL scheme performs better, SS13 is run with the YSU PBL scheme, with all other settings kept the same as SS06. SS06 outperforms SS13 at predicting accumulated precipitation, 10 m wind speed and 2m temperature. Therefore, the physics settings used for SS06 are used in the WRF-Chem simulation.

The WRF-Chem model is run for the same time period as the sensitivity simulations and is evaluated with CMORPH precipitation data, ground station data, and satellite data from CALIPSO and MODIS satellites. The model accumulated precipitation is compared to CMORPH and ERA-Interim, showing that WRF-Chem is able to resolve convection over the model domain. The model also successfully simulates the diurnal variation of 10 m wind speed and 2 m temperature. The smoke emissions are evaluated with MODIS AOT data and WRF-Chem succeeded at producing similar patterns and magnitudes of AOT over the MC. The model also successfully captures the variations in plume height when compared to the CALIPSO aerosol extinction profile. Finally, the WRF-Chem model succeeds at reproducing the diurnal variation of smoke concentration at all ground stations included in the evaluation.

4. THE UNCHARACTERISTIC OCCURRENCE OF THE JUNE 2013 BIOMASS-BURNING HAZE EVENT IN SOUTHEAST ASIA: COMBINED EFFECT OF THE MADDEN-JULIAN OSCILLATION AND TROPICAL CYCLONE ACTIVITY

In this chapter, we analyse satellite derived datasets and meteorological indices to investigate the aerosol and meteorological characteristics over the study region in June 2013. The peculiarity of the June 2013 haze event with regards to past extreme haze events in terms of its timing, ENSO and MJO conditions and fire count ratios is also outlined. Finally, we investigate the influence of the tropical cyclone Bebinca on the June 2013 haze event based on the WRF-Chem model results.

4.1 Overall Aerosol and Meteorological Environment during the June 2013 Haze Event

The start of the biomass burning season in the MC generally starts in Riau Province, Central Sumatra in June through early August (Reid et al., 2012). While significant events existed in 2004 and 2005, the worst biomass burning haze episodes to affect air quality in major cities of the MC occurred in June 2013 (Betha et al., 2014; Ho et al., 2014; Oozeer et al., 2016; Vadrevu et al., 2014; Velasco and Rastan, 2015). To reiterate, Figure 4.1(a) shows the MODIS fire hotspot detections over SEA during the study period. Fire activity was largely concentrated over the Riau region in Central Sumatra

while sparse hotspots occurred over Peninsular Malaysia and Borneo during the study period.

Reid et al. (2012) gives an overview of the seasonal fire behaviour in the MC and note that fire activity peaks over the MC as the Intertropical Convergence Zone (ITCZ) migrates northward during the SWM. The SWM season in SEA usually occurs from April to October and prevailing surface winds generally blow from the southwest over the MC towards the monsoonal trough east of the Philippines, as described in Chang et al. (2005), Moron et al. (2009), and Wang et al. (2009). The summer monsoonal trough extends from the West Pacific, through the Northern SCS and further over land in PSA and into the Indian monsoon. However, part of the monsoonal trough precipitation is a result of cyclone activity rather than simple ITCZ convection, as was the case when tropical storm Bebinca occurred over the SCS. Figure 4.2(a) shows the storm tracks of TCs that prevailed in June 2013, including storm Bebinca. The CMORPH precipitation fields in Figure 4.1(b) for the 17 to 25 June 2013 event period show that precipitation was a maximum over the SCS and Eastern PSA while a distinct region of dryness prevailed over Sumatra, Peninsular Malaysia and Western Borneo during the period. In fact, as Figure 4.1 shows, Central Sumatra received less than 2 mm of rainfall per day. TC activity over the SCS and its associated induced dryness over the MC in June 2013 is further discussed in Section 4.4. In addition, the observed fire activity corresponded with high AOT values over the region, as can be seen in Figure 4.1(c). AOT retrievals, at 550 nm, of at least 1.8 can be observed over Central Sumatra and all across southern Peninsular Malaysia through Southern SCS. Figure 4.1(c) also shows that smoke was transported all over the SCS by the prevailing southwesterlies and was eventually scavenged out by precipitation associated with tropical storm Bebinca. These winds were intensified as a result of TC activity over the SCS and the associated inflow arm enhancement, to be discussed in Section 4.4.

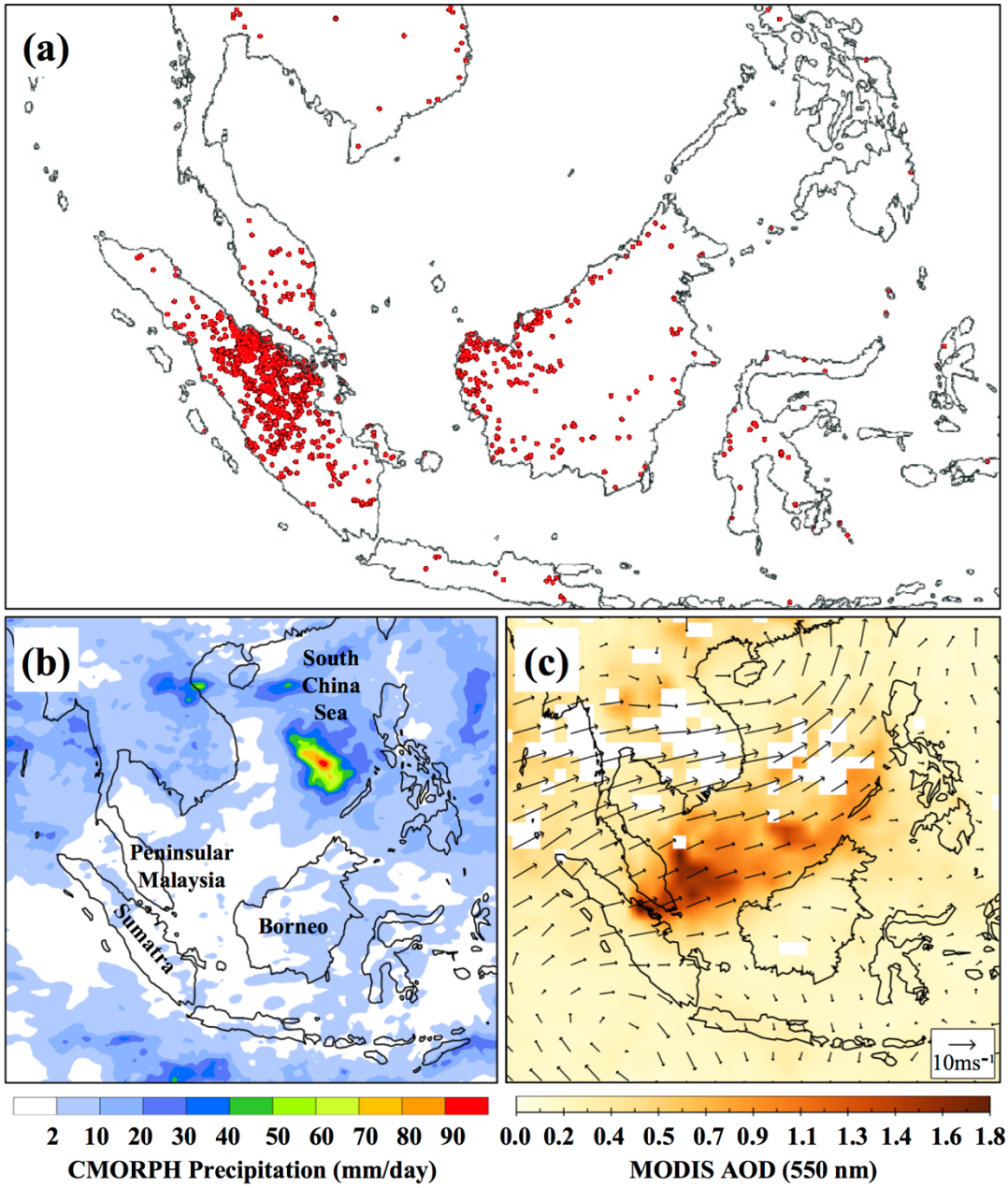


Figure 4.1 Overview of the aerosol and meteorological environment over the study region from 17 – 25 June 2013. (a) MODIS Terra and Aqua active fire hotspot detections (red dots). (b) CMORPH average daily precipitation. (c) MODIS aerosol optical thickness (AOT) at 550nm overlaid by average surface winds from the WRF-Chem simulations used in this study.

Figure 4.2(b) shows the Wheeler and Hendson (2004) product of MJO phase and amplitude for the months of May, June and July 2013 while Figure 4.3 shows the CMORPH precipitation plots for the period 10 to 28 June 2013 over the region 30°S to 30°N and 30°E to 150°W. Generally, MJO exists when amplitudes are higher than 1 and is deemed strong when amplitudes exceed 1.5. On 10 June, a weak phase 3 of the MJO prevailed and precipitation occurred along Eastern Indian Ocean as shown in Figure 4.3(a). Phase 4 of the MJO then prevailed until 14 June as convection and daily

precipitation gradually shifted from Central MC towards Eastern MC as shown in Figures 4.3(b – c). Precipitation then increased over the Western Pacific Ocean as phase 5 of the MJO prevailed from 15 to 18 June. The occurrence of the haze episode over SPM between 17 and 25 June 2013 coincided with the dry phases of the MJO over the MC. The MJO transitioned from phase 5 to phase 6 from 18 to 19 June, and from phase 6 to 7 on 21 June. During these periods, maximum drying due to induced subsidence can be observed over the MC while precipitation due to TC Bebinca prevailed over the SCS as shown in Figures 4.3(f – g). The amplitude of the MJO was higher than 1 throughout the haze episode and exceeded 1.5 from 23 June onwards. The MJO transitioned to phase 8 on 24 June marking the end of the dry phase over the MC. Figures 4.3(h – j) indeed show that precipitation gradually increased over the MC from 24 to 28 June. Similar mechanisms are also described in Reid et al. (2015, 2016), showing the contribution of MJO related subsidence to increased biomass burning over the MC.

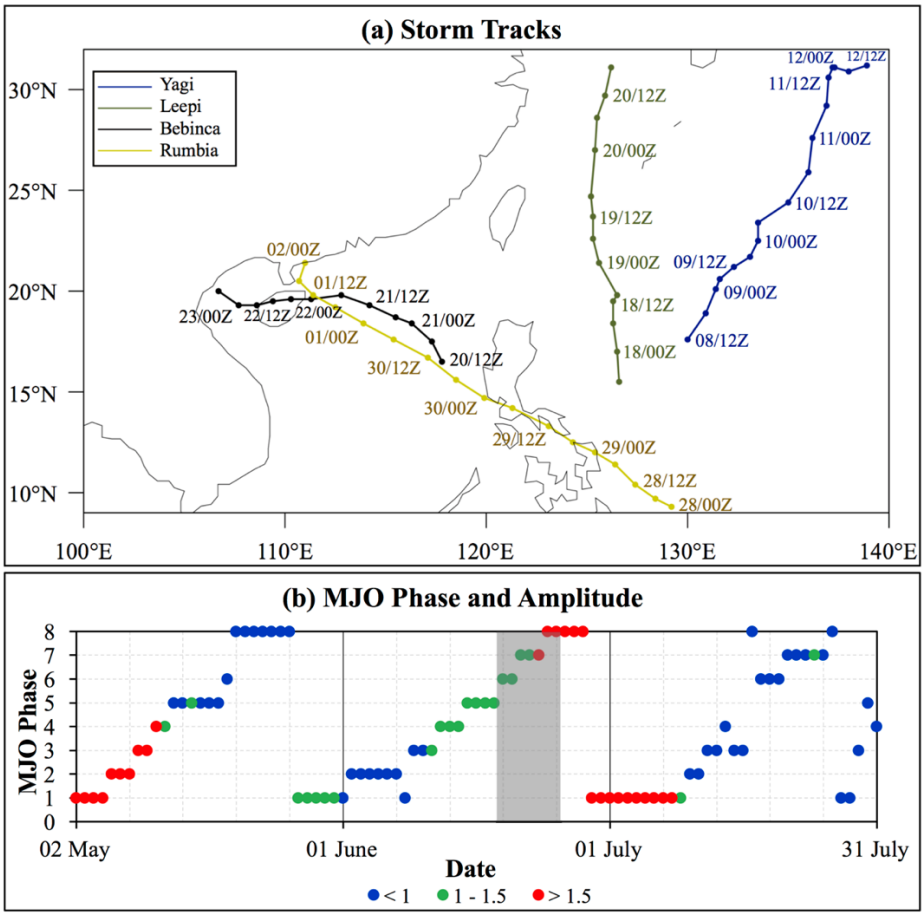


Figure 4.2 Storm tracks and MJO phase and amplitude. (a) Storm track of Yagi, Leepi, Bebinca and Rumbia over the Western North Pacific (WNP) in June 2013 (Unisys, 2013). The dates and times for each storm are also included. (b) Wheeler index of MJO phase and color coded

amplitude for May–July 2013, based on Reid et al. (2016), where amplitudes greater than 1 and 1.5 are considered as significant and strong, respectively. The grey shaded area represents the period 18–25 June when the haze episode occurred.

Figure 4.2(b) also shows that the strong MJO event of June 2013 is lagged and followed by weak MJO events with amplitudes of less than 1 from mid-May to beginning of June and for most of July. This behaviour of the MJO is discussed in Napitu et al. (2015) where it is suggested that it is the result of vigorous cooling of the sea surface temperature (SST) by the previous strong MJO. The migration of the MJO from the 17 to 25 June also coincided with the passage of tropical storm Bebinca over the SCS. This is further discussed in section 4.4.

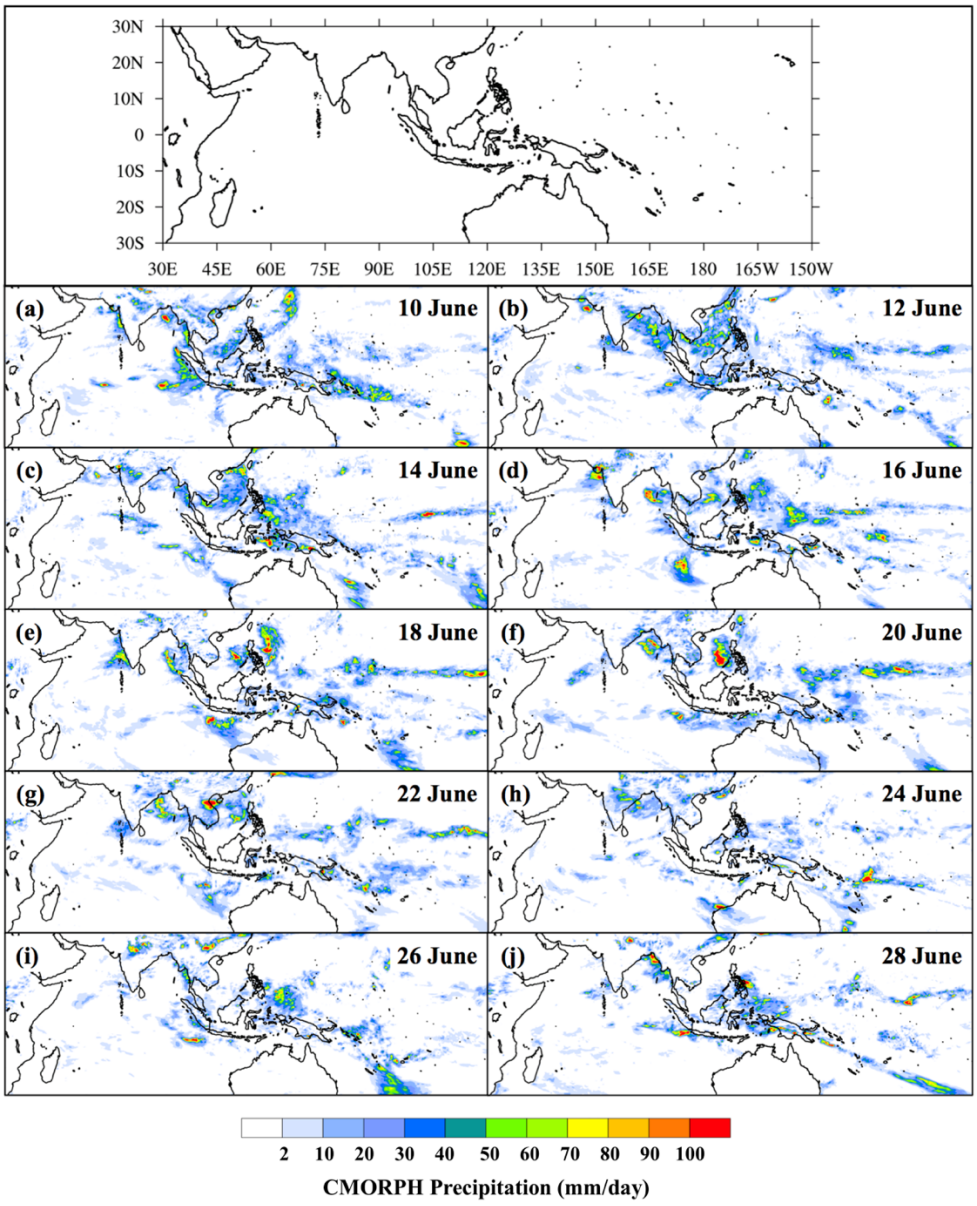


Figure 4.3 CMORPH daily precipitation over the region 30°S to 30°N and 30°E to 150°W for the period 10 – 28 June 2013.

4.2 2013 in Context: Time-Series of Fire, ENSO and MJO Characteristics

The MEI time-series for the years 1980 to 2016 is shown in Figure 4.4(a). Also included are markers which represent major haze episodes which have occurred during that time period. Red markers represent episodes which occurred during ENSO warm phases while the yellow marker represents the June 2013 episode. As highlighted by Reid et al. (2012), inter-annual fire variability is highly correlated to the ENSO warm phase, which can be observed in Figure 4.4(a). The worst episodes occurred in 1982–1983, 1997–1998 and 2015 (Field et al., 2016; Radojevic, 2003) and the peak MEI values during these 3 episodes were 2.909, 3.038 and 2.527, respectively, as shown in Figure 4.4(a). Typically, El Niño events correspond to MEI values of greater than 0.5. Interestingly, the June 2013 haze episode which is classified as one of the worst haze episodes in the region (Betha et al., 2014) occurred when neutral ENSO conditions prevailed. The MEI value during that month was -0.144. In contrast, all major red marked haze episodes occurred when the warm phase of ENSO since drier than normal conditions prevail during these periods (Reid et al., 2012).

In this section, the inter-annual MODIS fire counts are also compared to show that the occurrence of the intense haze episode of June 2013 was indeed anomalous. While short pulses of fire activity over Central Sumatra in June are not new (Reid et al., 2012), major fire episodes usually occur between August and October, as seen on Figure 4.4(a). Figure 4.4(b) shows the Aqua and Terra MODIS fire counts for the years 2000 to 2015 for the MC. Since neutral ENSO conditions prevailed in June 2013, as expected, the overall fire count for that period ranked low as compared to fire counts for the burning months for the years 2002, 2004, 2006, 2009, 2014 and 2015 which were all El Niño years. However, the fire count for June 2013 was comparable to the fire counts for the bulk burning months in 2003, 2005, 2007, 2008, 2010, 2011, which were non El Niño years. More interestingly, the fire count over only Sumatra and Peninsular Malaysia (SPM) in June 2013 was comparable to the El Niño correlated episodes of 2002 and 2006 as shown in Figure 4.4(c).

While the fire count during the burning season in 2015 over SPM was substantially higher than that of June 2013, it is clear that the June 2013 episode has one of the highest fire counts recorded by MODIS satellites over SPM. The MODIS fire count over the

MC and SPM in June for the years 2001–2015 are shown in Figure 4.5(b). While bearing in mind that MODIS fire products may only be considered semi-quantitatively, it is important to note that the fire counts recorded by both Aqua and Terra over the MC and SPM for the month of June were higher in 2013 than for any other year since both satellites came into operation. In fact, the average fire counts over SPM recorded by Aqua and Terra for the month of June since they came into operation are 2745 and 1692, respectively. In contrast, for June 2013, Aqua and Terra fire counts over SPM were 7453 and 6928, respectively. In addition, a ratio of fire count for SPM to MC, for the years 2001–2015, shows that the highest recorded ratio of 0.89 occurred in June 2013. Therefore, fire activity over SPM in June 2013 was indeed anomalous for that period of the year under the prevailing neutral ENSO conditions.

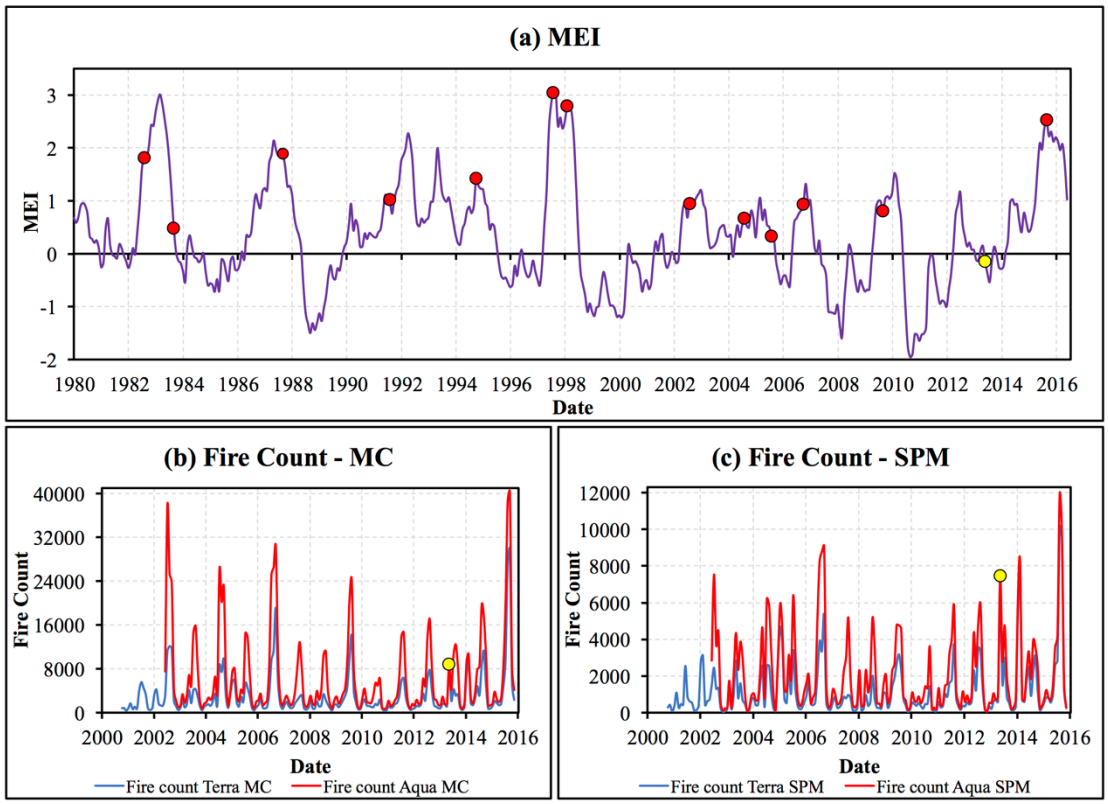


Figure 4.4 Time series data for ENSO, fire over the MC and MJO. (a) Multivariate ENSO Index (MEI) for 1980 – 2016. The red markers correspond to haze episodes which occurred when El Niño conditions prevailed, from left to right, August - September 1982, September 1983, September 1987, August – September 1991, August to October 1994, August – October 1997, February – May 1998 (Radojevic, 2003), August – September 2002 (Fuller, 2003), August 2004 (Field et al., 2009), August 2005 (Mahmud, 2009), September – October 2006 (Wang et al., 2013), September 2009 (Hamada et al., 2013) and September – October 2015 (Field et al., 2016). The yellow markers in (a), (b) and (c) represent the June 2013 episode. (b) Monthly MODIS fire count for the MC from 2000 – 2015. (c) Monthly MODIS fire count for Sumatra and Peninsular Malaysia (SPM) for 2000 – 2015.

Figure 4.5 shows the time series data for ENSO, precipitation, fire count and the MJO in June. While ENSO is a good indicator of seasonal burning, it cannot explain all dry spells and corresponding burning episodes. Figure 4.5(b) shows that intense fire episodes over the MC also occurred in June for the years 2003, 2004, 2005, 2009 and 2012. The average ratio of fire count for SPM to MC from both Aqua and Terra satellites was at least 0.60 in June for these years showing that most burning occurred over the SPM as compared to the rest of the MC. The MEI values in June for the years 2001–2015 and the mean CMORPH daily precipitation rates over SPM in June for the years 2003–2015 are shown in Figure 4.5(a). The average precipitation rate over SPM in June for that period was 1.6 mm day^{-1}. In contrast, the precipitation rates in June for the years 2003 (0.9 mm day^{-1}), 2004 (1.3 mm day^{-1}), 2009 (1.4 mm day^{-1}), 2012 (1.2 mm day^{-1}) and 2013 (1.5 mm day^{-1}) were all lower than the average, except for the year 2005 (1.8 mm day^{-1}). In 2003, 2004, 2005 and 2013 neutral conditions prevailed while the MEI values for 2009 and 2012 were 0.880 and 0.941, respectively. Therefore, in June 2009 and 2012 years, the low precipitation rates can be largely explained by the prevailing ENSO conditions as shown in Figure 4.5(a). In June 2003 and 2004, the daily precipitation rates were particularly low at 0.9 and 1.3 mm day^{-1}, respectively, despite the prevailing neutral ENSO conditions. Positive El Niño Modoki conditions reported by Reid et al. (2012) during these two years could have contributed to subsidence over the MC. Positive Modoki events represent a phenomenon of positive SST anomalies over the Central Pacific which results in increased surface pressure over the MC (Ashok et al., 2007). In addition, MODIS on both Aqua and Terra recorded a higher fire count in 2003 and 2004 (neutral ENSO conditions) than 2009 and 2012 (positive ENSO conditions) for both MC and SPM. The only exception was the MODIS Terra fire count for the MC in June 2004 which was comparable to that of June 2012. This shows that while ENSO is a good indicator of seasonal burning, the intensity of burning activity does not only depend on ENSO conditions. Comparing June 2013 to June 2003 and 2004, the daily precipitation rate over SPM were only slightly higher in 2013 at 1.5 mm day^{-1}. However, it needs to be reiterated that interestingly, the highest fire count in June was recorded in 2013 for the period 2001–2015. This indicates that the days during which the haze episode occurred in June 2013 were much drier than the rest of the month, since very dry conditions must have prevailed to sustain the intense episode of June 2013.

The MJO phase and amplitude in June for the years 2003, 2004, 2005 and 2013 are compared in Figure 4.5(c). A transition to a new MJO cycle occurred in June 2003 as phases 8 and 1 were predominant during that time period. This shows that subsidence over the region during time period was not a result of the MJO cycle. In contrast, phases 2 and 3 dominated June in 2005 at amplitudes of less than 1 showing that a weak MJO prevailed during that period. More importantly, it can be seen that a complete MJO cycle occurred in 2004 and 2013. As mentioned in Section 4.2, the strong MJO event of June 2013 coincided with the occurrence of the haze episode over SPM. While amplitudes of higher than 1 prevailed in June 2013, the MJO event of June 2004 was dominated by amplitudes of lower than 1 until the end of the month when amplitudes of higher than 1.5 prevailed during phase 7. Therefore, the stronger MJO event of 2013 could have contributed to the much higher fire count as compared to June 2004.

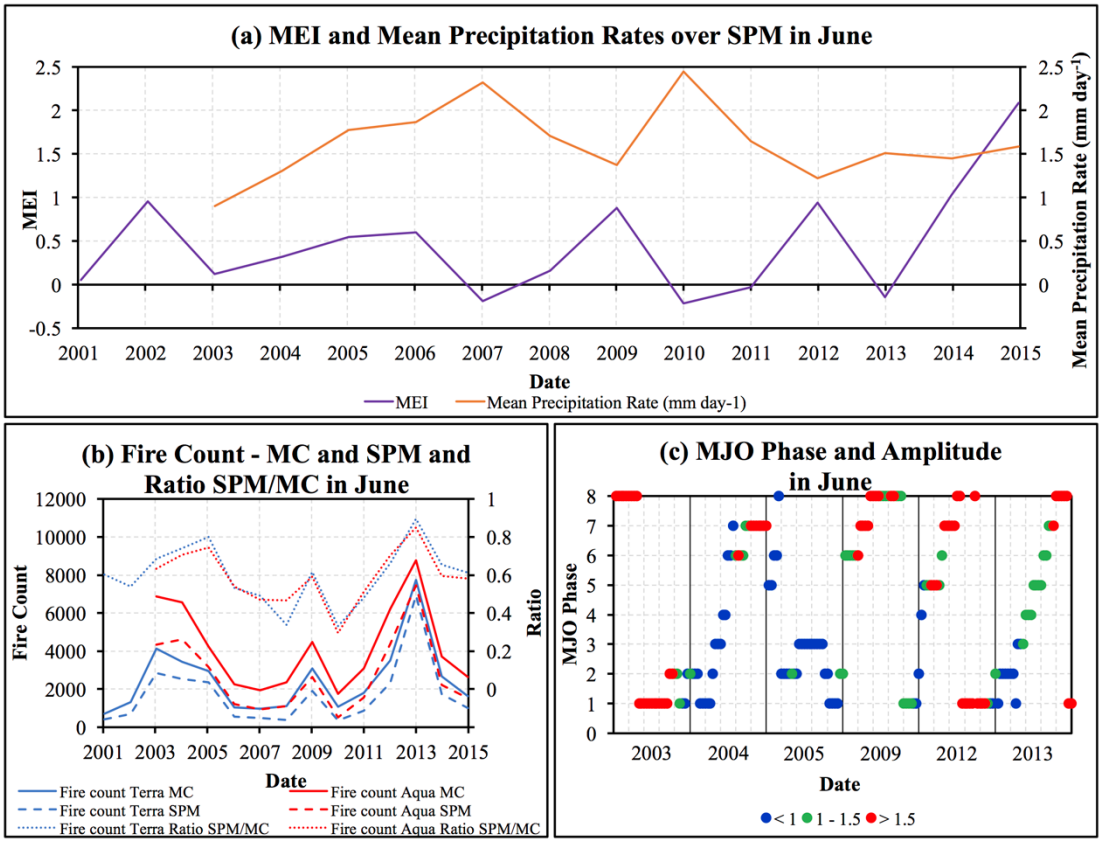


Figure 4.5 Time series data for ENSO, precipitation, fire over the MC and SPM, and MJO in June. (a) Multivariate ENSO Index (MEI) for 2001 – 2015 and mean CMORPH daily precipitation rate (mm day-1) over SPM for the years 2003–2015. SPM for CMORPH precipitation rates include data cells over the region 6°S to 7°N and 95°E to 107°E. (b) Monthly MODIS fire count for the MC and SPM, and ratio of MODIS fire count over SPM to that over MC from 2001 – 2015. (c) Wheeler index of MJO phase and color coded amplitude for the years 2003, 2004, 2005, 2009, 2012 and 2013.

4.3 Combined Effect of Tropical Cyclone Bebinca and the MJO

During the summer monsoon, as the ITCZ migrates northwards, southwesterlies tend to prevail over the western MC and the SCS. Furthermore, the Western North Pacific (WNP) is the most active basin of tropical cyclogenesis (Neumann, 1993) and 80% of the TCs develop within or in the surroundings of the ITCZ, where low-level convergence occurs between the trade easterlies and the southwesterlies (Chen and Ding, 1979; Gray, 1979). In 2013, the TC season in the WNP was marked by an above average genesis of TCs and was characterised by an early active TC season in June (Ying et al., 2014). In fact, four TCs were generated in June 2013, which is twice the climatological average of 1.8 TCs (Ying et al., 2014). These four TCs, namely Tropical Storm Yagi (8–12 June), Tropical Storm Leepi (17–20 June), Tropical Storm Bebinca (20–23 June) and Typhoon Rumbia (28 June–2 July) are shown in Figure 4.2(a). Bebinca, which coincided with the extreme haze event over Sumatra, Singapore and Malaysia, began to develop on 18 June and rapidly intensified into a Tropical Depression (TD) migrating northwards over the SCS. By 21 June Bebinca had intensified into a Tropical Storm (TS) and started migrating westwards towards PSA and maximum wind speeds of 18 m s^{-1} were recorded. By 24 June Bebinca had lost strength as it made landfall over PSA. More details about the mentioned storms can be found in the Joint Typhoon Warning Center Annual Tropical Cyclone Report for 2013 (Joint Typhoon Warning Center, 2013).

The increase in fire activity in the southern MC and transport of smoke over the SCS as TCs transit the SCS has been reported by Reid et al. (2012, 2015). Wang et al. (2013) also showed how cyclone Xangsane enhanced southwesterly winds and induced large scale subsidence over the MC, which contributed to fire propagation over Kalimantan and Sumatra in October 2006. However, these events occurred when TCs climatologically are more prevalent in the SCS/Philippines region. In June, the storm tracks are typically further north. In June 2013, however, TCs were abnormally south. Weather in the MC was influenced by an intensification of the low pressure belt of the northern ITCZ, which drew stronger winds from the Indian Ocean towards the northeast (Oozeer et al., 2016). This intensification was in fact Bebinca. The co-evolution of Bebinca and the haze event is depicted in Figure 4.6, which shows MODIS images from the Terra and Aqua satellites for 17 to 26 June 2013, the corresponding WRF-Chem

simulated daily averaged sea level pressure (SLP) and near-surface wind patterns, as well as daily averaged and vertically integrated $PM_{2.5}$ concentrations (Darker red plumes indicate higher concentrations of $PM_{2.5}$). On 17 June, very few fire hotspots can be observed over the MC with westerlies and southwesterlies blowing over Sumatra and Peninsular Malaysia as shown in Figures 4.6(a) and 4.6(g). On 19 June, increased cloud cover can be observed over the SCS, as Bebinca gradually generated into a TD near 16°N and 115°E over the SCS, while the reverse occurred over Sumatra and Peninsular Malaysia as shown in Figure 4.6(b). An increase in fire hotspots over Central Sumatra can also be observed as well as smoke being transported in a northeasterly direction from the hotspots over Sumatra to Western Borneo and the SCS by enhanced monsoonal flow. The eastward motion of the emissions plume is aided by winds associated with the Sumatran low located near 5°S and 105°E as shown in Figures 4.6(h) and 4.6(n) as well as the prevailing westerlies which persist over Sumatra during the dry phase of the MJO over the MC.

By 21 June, cyclone Bebinca had intensified into a TS as shown by increased cloud cover over the SCS in Figure 4.6(c) and reduced SLP and stronger associated winds as shown in Figure 4.6(i). As Bebinca started moving westward towards PSA, relatively dry weather persisted over Central Sumatra, except for some scarce clouds associated with Bebinca. A high number of fire hotspots prevailed over Sumatra as well as continued haze propagation over the MC. Despite the fact that part of the smoke seemed to be confined within the clouds in Figure 4.6(c), a similar widespread smoke pattern is simulated by the model as shown in Figure 4.6(o). On 22 June, the intense TC Bebinca had already reached the east coast of PSA and the winds over Sumatra and Peninsular Malaysia had shifted to higher flow in a north-northeasterly direction. This also resulted in a gradual shift in the plume flow from Sumatra as shown in Figure 4.6(p). In fact, the most intense and widespread emissions seem to have occurred between 21 and 22 June as shown by Figures 4.6(o) and 4.6(p). This period also corresponds to the period during which TC Bebinca was the strongest as shown in Figures 4.6(i) and 4.6(j). Figure 4.7 shows the vertical velocity over cross-sections YY' and ZZ', which are marked on Figure 4.6(j), on 22 June. The wind fields for each cross-section were calculated from the horizontal velocity along that cross-section and 10 times the vertical velocity. The intensification and propagation of hotspots and emissions over Sumatra can be attributed to the large-scale subsidence and induced

dryness due to cyclone Bebinca as shown in Figure 4.7(a). Deep convection can also be observed between 15°N and 22°N resulting in large scale divergence near the upper troposphere. Air over Sumatra, near the equator, is in turn accelerated towards the convection centre of Bebinca through the inflow arm of the cyclone. Upper level winds are accelerated towards the equator where upper level convergence occurs, resulting in subsidence over Sumatra and the formation of a deep convective cell between the equator and 22°N along cross-section YY'. Orographic motion over the mountains of Sumatra can also be observed. The influence of dry air due to mountain flow on increased fire activity over Central Sumatra in June 2013 is discussed in Oozeer et al. (2016).

To further investigate the subsidence induced by TC Bebinca over Riau, the vertical speed maps at 700 hPa are plotted for 17 and 22 June as shown in Figure 4.8. These dates were selected since Bebinca only started to develop on 18 June and reached maximum intensity between 21 and 22 June. The plots in Figure 4.8 were extracted from the model output for the nest d02. Comparing Figures 4.8(a) and 4.8(c), it is clear that TC Bebinca induced significant subsidence over Riau. On 17 June, upward vertical motion prevailed at speeds reaching 9 cm s^{-1} while on 22 June, downward vertical motion prevailed at speeds of at least 6 cm s^{-1} over the same region. In addition, reduced horizontal wind speed at 700 hPa can be observed over Riau as a result of subsidence. Figures 4.8(b) and 4.8(d) also show that the daily averaged surface $PM_{2.5}$ concentrations increased drastically over the region as a result of fire activity. More interestingly, Figure 4.8(d) shows that the smoke sources over Riau were concentrated specifically over the regions where subsidence prevailed but not where upward vertical motion occurred between the equator and 2 °N. The surface $PM_{2.5}$ concentrations reached at least 1000 μg m^{-3} over that region on 22 June.

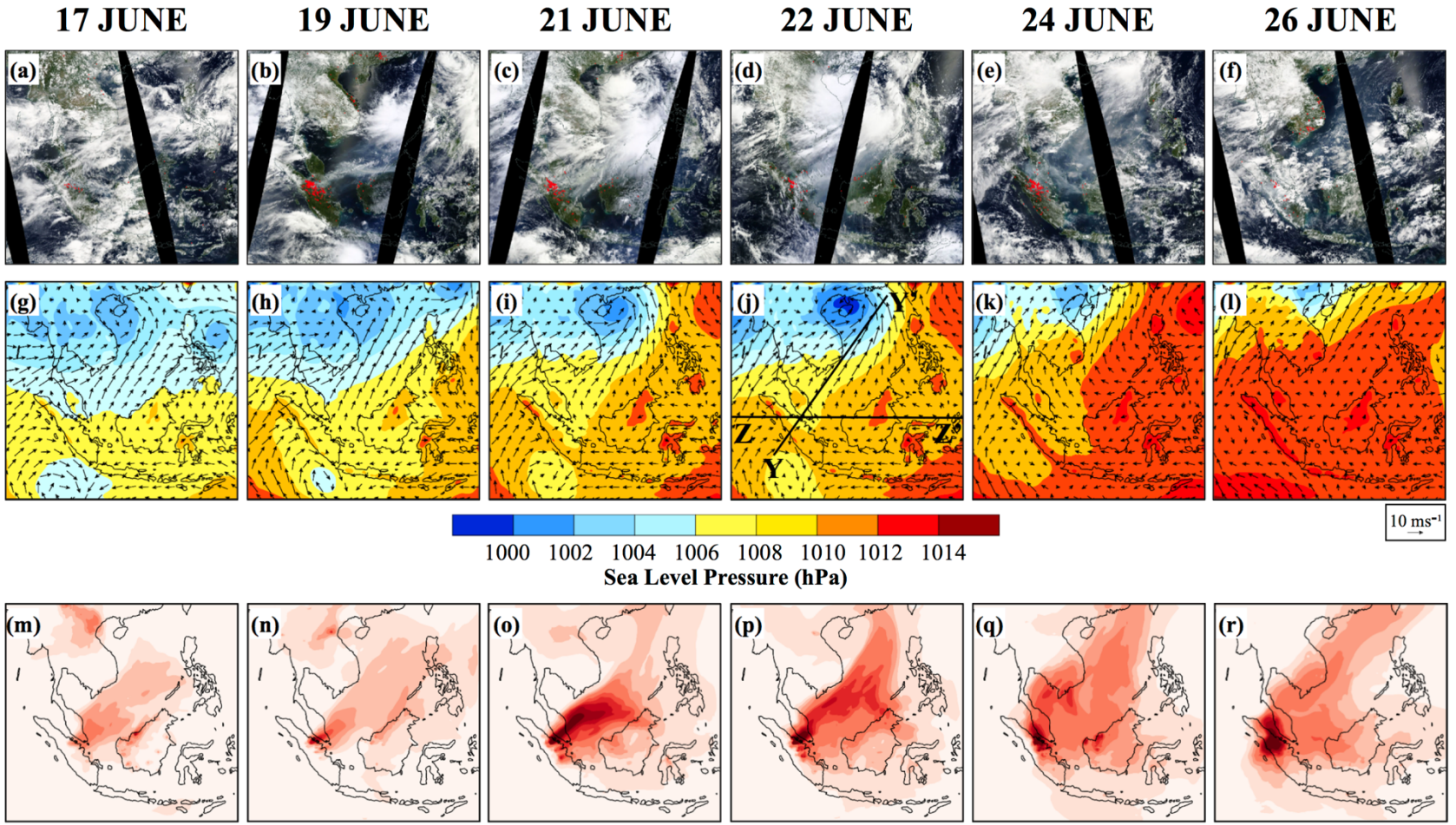


Figure 4.6 MODIS images from the Terra and Aqua satellites for days between 17 and 26 June 2013 (a-f). The red spots correspond to regions of fire hotspots. (g-l) The corresponding WRF-Chem simulated daily averaged SLP (hPa) and near-surface wind fields (m s^{-1}). (m-r) The daily averaged and vertically integrated $PM_{2.5}$ mass concentration (Darker red plumes indicate higher concentrations of $PM_{2.5}$). The black lines over (j) represent cross-sections YY' and ZZ'.

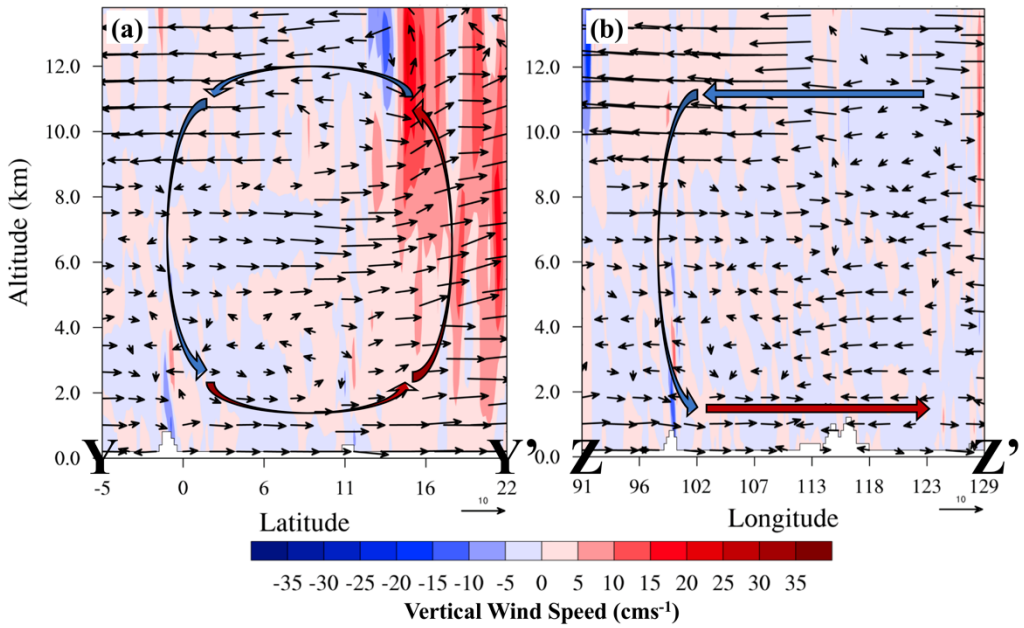


Figure 4.7 Wind fields (m s^{-1}) (arrows) and Vertical wind speed (cm s^{-1}) (shaded colors) on 22 June along (a) YY' and (b) ZZ'. The colored red and blue arrows represent the overall convective cells that occur along each respective cross-section.

Figure 4.6(k) shows that cyclone Bebinca had lost in intensity by 24 June but induced subsidence and dryness prevailed over Sumatra and emissions were still strong on that day with the plume flowing in a northerly direction. By 26 June Bebinca had weakened into a low-pressure system and the subsidence over Sumatra had subsided as shown by the increase in cloud cover in Figure 4.6(f). Fire hotspots had also drastically reduced over Sumatra and so did the smoke concentrations as a result. A 12-hour interval plot of SLP plots with wind vectors and surface $PM_{2.5}$ concentrations is given in Appendix C. The weakening of cyclone Bebinca marked the end of the haze episode over Peninsular Malaysia and Sumatra thus indicating a significant correlation between the intensification and propagation of forest fires and the transport of BBH over the MC due to TC activity over the SCS. More importantly, this shows that improving the ability to predict extreme TC episodes over the SCS can in turn help improve our ability to model and predict intense BBH episodes over the MC.

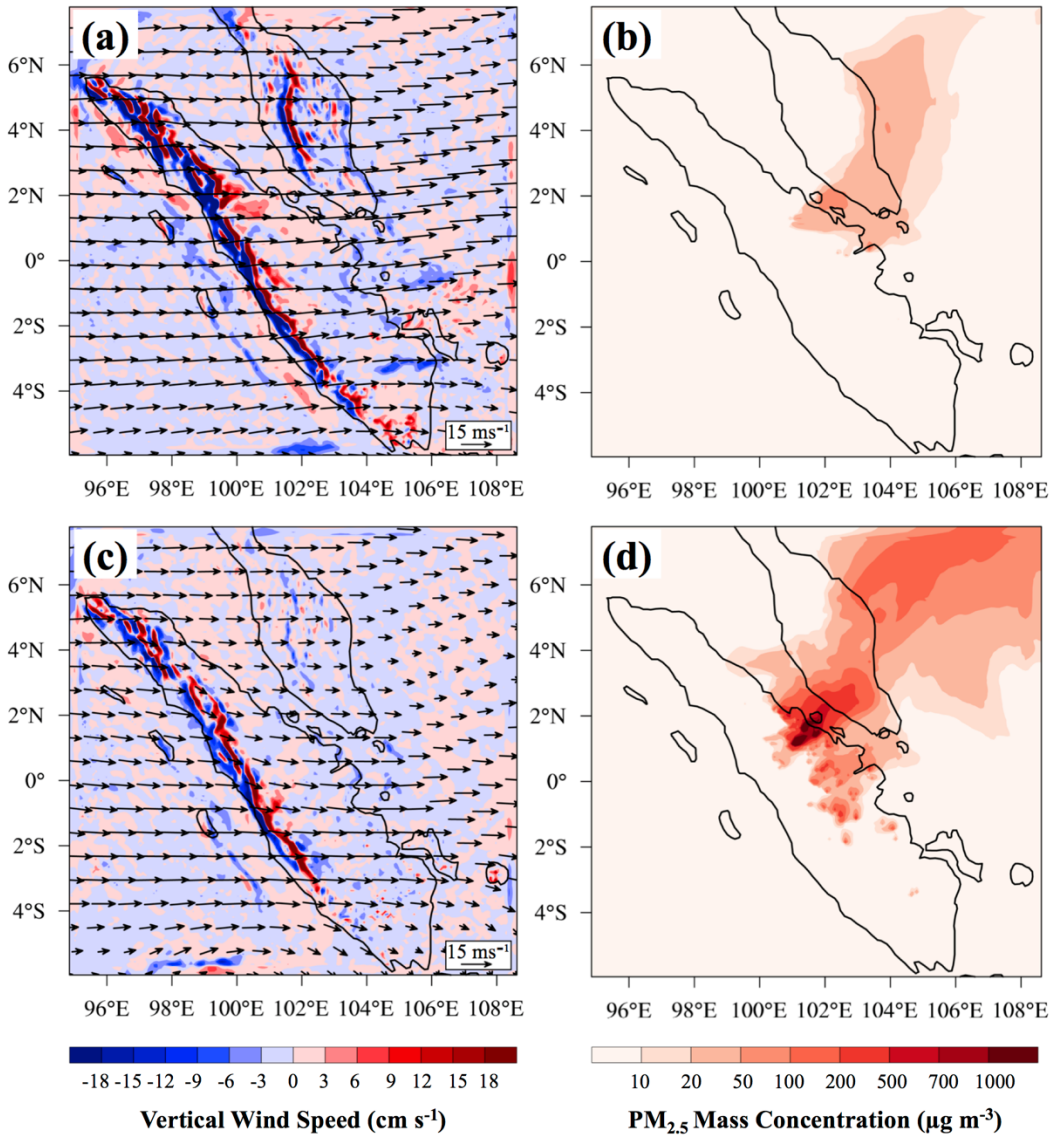


Figure 4.8 WRF-Chem simulated daily averaged vertical speed (cm s^{-1}) and wind fields (m s^{-1}) at 700 hPa height (left column) and surface $PM_{2.5}$ mass concentration (µg m^{-3}) (right column) for 17 (a-b) and 22 (c-d) June 2013, respectively.

It is also important to note that the migration of the MJO discussed in Section 4.2 and 4.3 coincided with the train of TC activity over the SCS and NWP in June 2013 as was the case in Reid et al. (2015) during the Vasco Cruise in September 2011. Maloney and Hartmann (2001) reports that the transit and departure of the MJO from the MC is often associated with an increase in TC formation in the region. The favourable conditions for TC formation set by the transit of the MJO in June 2013, that is growing eddies, strong surface convergence and high sea surface temperatures (Maloney and Hartmann, 2001) could therefore have contributed to the formation of the 4 TCs shown in Figure 4.2(a). Two characteristics of the MJO-TC relationship for June 2013 are of note. Firstly, out of the four TCs, only Bebinca and Rumbia crossed the SCS while Yagi and

Leepi migrated northwards over WNP, as shown in Figure 4.2(a) and the seesaw shift of the preferable cyclogenesis region discussed in Kim et al. (2008) can be observed in June 2013. Usually, when the MJO related convection centre is located over the Indian Ocean TCs tend to migrate eastward, and westward when the MJO convection centre occurs over the WNP. As seen in Figure 4.2, Yagi occurred during phases 2–4 of the MJO, Leepi occurred during phase 5, Bebinca occurred during phases 6–7 and Rumbia occured during phase 8. This leads to the second characteristic of the MJO-TC relationship over the MC in June 2013. The migration of Bebinca over the SCS coincided with the dry phases of the MJO over the MC and therefore the combined subsidence due to Bebinca and the MJO lead to intense fire activity occurring over Central Sumatra. Figure 4.7(b) shows the cross-section ZZ' marked over Figure 4.6(j). Low level westerlies and upper level easterlies can be observed along ZZ' with subsidence occurring throughout the cross-section over the MC, especially between 96°E and 107°E. The convective centre is not visible in Figure 4.7(b) since by phases 6–7 of the MJO, convection occurs to the east of the model domain. It is also interesting to note that no major haze event occurred when Rumbia, which had intensified into a Category 1 Typhoon with maximum wind speeds of 36 ms^{-1} (twice as fast as Bebinca), migrated westwards over the SCS. This suggests that Rumbia related subsidence was not enough to suppress the MJO related convection over the MC. Rumbia coincided with phase 8 of the MJO when the MJO cycle is about to terminate over the Pacific and restart over the Indian Ocean. MJO amplitudes were higher than 1.5 from 23 June to 8 July. The uncharacteristically early and strong June 2013 event therefore occurred as a result of the combined subsidence from Bebinca and the MJO.

4.4 Discussion and Summary

One of the worst episodes of biomass-burning haze over the MC occurred in June 2013. However, the magnitude for this timing was uncharacteristic of the seasonality of extreme fire events in the region. In order to study this peculiar case, the aerosol and meteorological characteristics over SEA during the study period of 17 to 25 June were investigated. MODIS fire hotspot detections showed that fire activity was concentrated over Central Sumatra during the haze episode, which corresponded to high AOD retrievals of at least 1.8 over the region. CMORPH precipitation fields for the same period also showed that precipitation was a maximum over the SCS while Central Sumatra was particularly dry. The AOT retrievals indicated that smoke was transported

by southwesterlies, which prevail during the SWM season, towards the SCS where it was eventually scavenged out by precipitation associated with TC Bebinca.

Fire activity is a combination of economic need and meteorological opportunity. By the start of the drier southwest monsoon season, farmers begin to clear land and prepare for burning. This chapter focused on three features of interest that created highly favourable fire weather in the study region, namely, ENSO, the MJO and TC activity. The MEI time-series from 1980 to 2016 showed that neutral ENSO conditions prevailed during the June 2013 haze episode with an MEI value of -0.144 for that month. In contrast, the three worst episodes over the MC during that period occurred in 1982–1983, 1997–1998 and 2015 when warm conditions prevailed. Major fire episodes usually occur between August and October in the MC. Therefore, the overall MODIS fire count over the MC in June 2013 expectedly ranked low as compared to bulk-burning months which occurred during El Niño years but were comparable to those during non El Niño years. Comparing fire counts that occurred over only SPM, June 2013 was surprisingly comparable to El Niño correlated episodes of 2002 and 2006. MODIS fire counts observed over SPM and the MC for June were the highest in 2013 as compared to any other year that MODIS Aqua and Terra satellites have been in operation and the highest ratio of fire count for SPM to MC was recorded in June 2013. The nature of fire activity over SPM in June 2013 was therefore uncharacteristic for that period of the year under neutral ENSO conditions.

The mean daily precipitation for the month of June for the years 2003–2015 were also compared. In particular, data for June in 2003, 2004, 2005, 2009, 2012 and 2013 were investigated since notable fire episodes occurred during these periods. While dry conditions can be attributed to positive El Niño conditions in June 2009 and 2012, June 2003 and 2004 were particularly dry despite the prevailing neutral ENSO conditions, possibly due to positive Modoki conditions during these 2 years. Interestingly, the fire count over SPM in June 2013 was much higher than in the drier months of June in 2003 and 2004. The MJO phase and amplitude time-series showed that phases 6–7 of the MJO prevailed over the MC in June 2013, inducing subsidence over the region. In contrast, the wet phase of the MJO prevailed in June 2003 while a weaker MJO event occurred in June 2004 as compared to June 2013. The MJO induced subsidence over SPM therefore contributed to increased burning over the region.

WRF-Chem was used to investigate the influence of TC Bebinca over the SCS on the haze event and was run from 14 to 27 June 2013. In 2013, the TC season over WNP was marked by an above average number of TCs. TC Bebinca was generated over the SCS during this active and early period of cyclone genesis, which could have been the result of the transiting MJO, and was found to have serious intensifying effects on the propagation of forest fires over Sumatra and the transport of haze over the MC. The model results showed that subsidence associated with Bebinca and the dry phases of the MJO contributed to regions of dryness over Central Sumatra and the migration of Bebinca from the SCS onto Indochina governed the direction of plume flow from Sumatra. In fact, the extreme haze event of June 2013 coincided with the presence of TC Bebinca. Therefore, intense and early TC seasons over the WNP can be an indication of the occurrence of early and extreme haze events over the MC. More importantly, the combined subsidence due to both Bebinca and the MJO is a phenomenon which requires further attention since no haze event occurred when stronger Category 1 Rumbia crossed the SCS during the lesser dry phase 8 of the MJO over the MC.

5. NUMERICAL STUDY OF THE TRANSPORT AND CONVECTIVE MECHANISMS OF BIOMASS BURNING HAZE IN SOUTH-SOUTHEAST ASIA

In the previous chapter, WRF-Chem results for the main domain were used to investigate the overall phenomenology and transport of haze over the study area. In particular, the influence of TC Bebinca on the overall transport of smoke over the region was demonstrated. In order to show the subsidence that was induced over Sumatra due to TC Bebinca, plots of vertical velocity were extracted from the 9 km nest. This chapter extends the use of this nest to investigate and analyse in detail the transport of haze over SPM and the convective mechanisms which uplift haze within the troposphere. While cumulus schemes are still required to implicitly resolve convection for a grid resolution of 9 km, higher grid solutions can resolve convection better (Klich and Fuelberg, 2014). Therefore, results from the 9 km nest are used to investigate the vertical transport of haze and convective mechanisms over SPM. In this chapter, $PM_{2.5}$ mass concentration plots and vertical wind speed at different levels in the atmosphere as well as cross-sections along major smoke plumes are analysed to identify the deep convective mechanisms responsible for uplifting haze emissions up in the troposphere.

5.1 Vertical Transport and Convective Mechanisms

Regions of deep convection near and downwind of the forest fire hotspots that were responsible for the transport of BBH to higher altitudes, and which are not easily observed through measurements, are identified in this chapter. Figures 5.1 to 5.6 show major smoke plumes which occurred during the haze episode, in particular plumes which reached at least the 700 hPa height (~ 3 km). In these figures, particular attention is given to results at 850 hPa and 700 hPa height respectively, which are two standard

weather map plot heights. The 850 hPa height is usually located right above the PBL and also where the residual smoke layers generally are (Pahlow et al., 2005; Wang et al., 2006). Therefore, the horizontal wind vectors at this height can be a good indication of the general direction of smoke plume flow while the vertical wind speeds at this height may also indicate whether any convection which could uplift the smoke particles to higher altitudes is taking place. If a plume has exceeded the 850 hPa height and reached the 700 hPa height, and deep convection occurs over that region, the smoke particles can be transported further up in the troposphere. Therefore, the $PM_{2.5}$ mass concentration is also shown for these levels, in addition to the surface concentration. For each major identified plume, a 3D isosurface of $PM_{2.5}$ mass concentration over the nest is also shown to provide a clearer picture of the overall shape and extent of the plume. A side view of the nest, as seen from the south, is shown for each iso-surface figure. Finally, a vertical cross-section of the plume of interest at a given time t is illustrated, as well as a vertical cross-section of vertical wind speed to show the convection mechanism responsible for the uplifting of the smoke. The vertical cross-section of vertical wind speed of the previous hour, that is $t - 1$, is shown since the convection occurring at the previous model output time-step (1 hour) is observed to be responsible for the vertical plume motion. The wind fields in both plots are calculated from the horizontal velocity along a particular cross-section and 10 times the vertical velocity (10 w). The identified convective mechanisms which transport haze up in the troposphere are illustrated and described below.

5.1.1 Orographic Motion over the Barisan Mountains in Sumatra

In Chapter 4, the WRF-Chem results are used to show that wind blew predominantly from the southwest over SPM during the haze episode and that subsidence due to TC Bebinca resulted in decreased precipitation and increased fire activity over Sumatra. However, the fires over Sumatra might also have been sustained by dry warm air flowing over the Barisan Mountains onto Riau. The Barisan Mountains are a range of mountains located along the west coast of Sumatra. As moist air coming from the Indian Ocean is force-lifted over the windward side of the mountain, moisture is lost to cloud formation thus resulting in dry air which warms up as it flows down over the leeward side of the mountain. If the winds blowing over the mountains are fast enough, this can result in the formation of turbulent eddies on the leeward side of the mountain. These eddies, called mountain waves, can also induce convection on the leeside of the

mountain (Houze Jr, 2012). Such convection may also be triggered by diurnal heating over the mountainous terrain (Mapes et al., 2003) or by gravity wave motions which are induced by the airflow over the terrain (Tripoli and Cotton, 1989). Such mountain flow which uplifted smoke emissions to altitudes reaching at least 3 – 7 km can be observed on 19 and 20 June in Figures 5.1 to 5.3.

Figure 5.1 shows the $PM_{2.5}$ mass concentration at 09 UTC and the vertical wind speed at 08 UTC on 19 June 2013. The smoke concentrations were mostly confined to below 2 km in height as shown by Figures 5.1(a), (b), (c) and (d). Figure 5.1(e) shows that southwesterlies prevailed at 850 hPa height, and the smoke plume near the surface was carried accordingly as shown in Figures 5.1(a) and (b). Figure 5.1(c) shows that only one plume reached at least the 700 hPa height. This plume can be observed in Figure 5.1(d). Vertical wind speeds of at least 6 cm s^{-1} prevailed over that location at 850 hPa height. Figures 5.1(f) and (g) show that the smoke plume reached more than 3 km in height near 101.7 °E due to strong vertical motion of at least 35 cm s^{-1} extending up to at least 3 km in height, prevailing over that location. The Barisan Mountains are located between 99.4 °E and 101.7 °E along the cross-section. The mountain flow and the corresponding eddies causing this upward vertical motion can be clearly observed between 99.4 °E and 104.0 °E in both Figures 5.1(f) and (g).

Similarly, on 20 June, orographic motion over the Barisan Mountains was responsible for the uplifting of smoke to at least 7 km height at 11 UTC over Riau and the Strait of Malacca (the sea between Sumatra and Peninsular Malaysia) as shown in Figures 2(d) and (f). This plume in fact grew from a smaller plume 4 km high at 08 UTC (not shown), which occurred due to mountain flow, between 99.4 °E and 101.7 °E. As mountain flow persisted, vertical upward motion reaching at least 35 cm s^{-1} uplifted the smoke emissions further to about 7 km in height. This is shown in Figures 5.2(f) and (g). A northeasterly plume persisted over SPM due to the fires. A second major plume also occurred further south in Riau, reaching at least 4 km in height at 11 UTC as shown in Figures 5.2(c) and 5.3(a). This peak in the plume occurred as a result of vertical convective motion reaching about 3 km in height at 101.7 °E as shown in Figure 5.3(b). Comparing the 2 plumes in Figures 5.2(f) and 5.3(a), the residual layer associated with the 4 km plume reached at least 2 km in height while that associated with the 7 km plume remained mostly confined near the surface downwind of the fire hotspots.

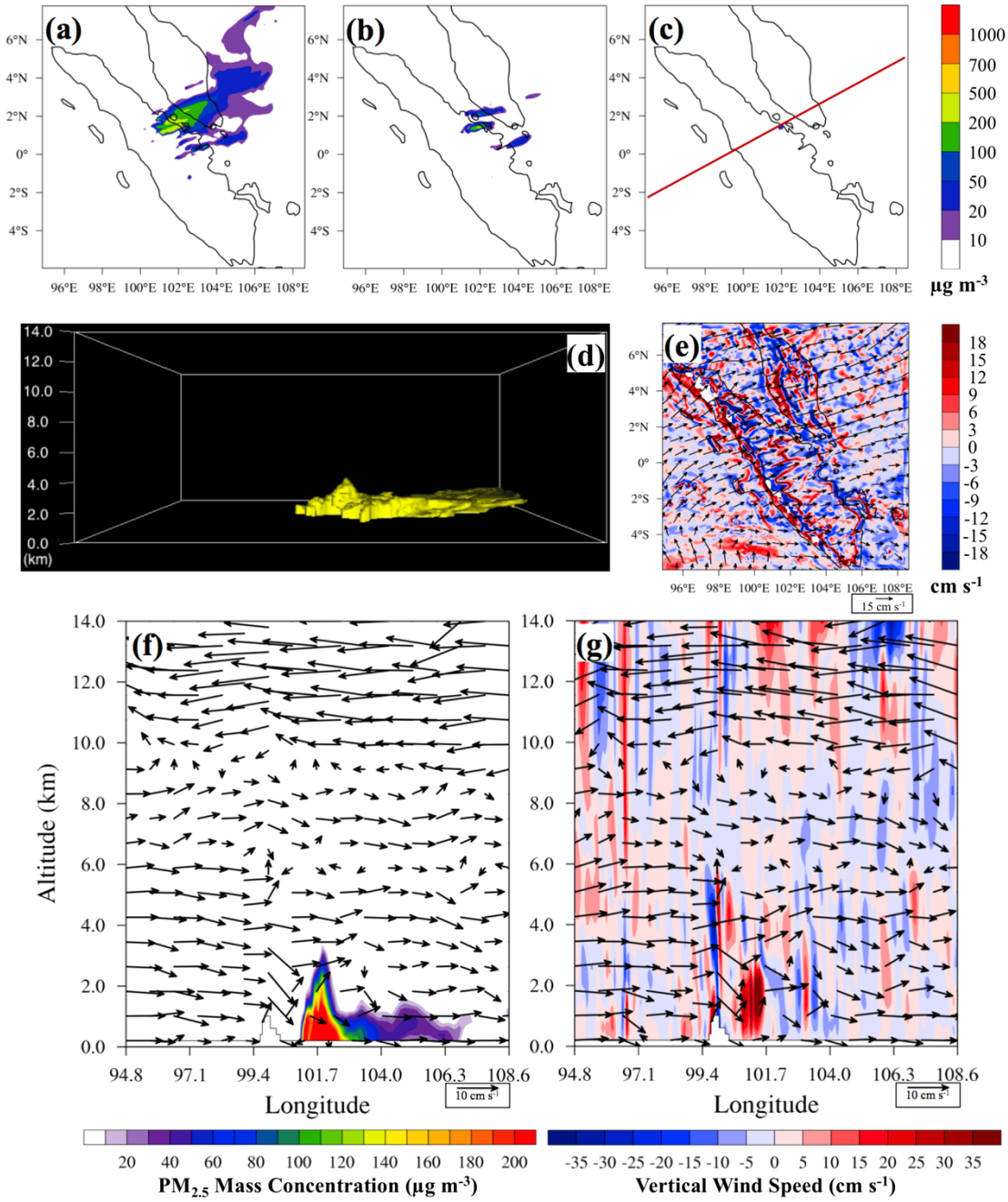


Figure 5.1 Smoke plume at 09 UTC and vertical wind speed at 08 UTC on 19 June 2013. Plots of $PM_{2.5}$ mass concentration (µg m^{-3}) at (a) surface, (b) 850 hPa height and (c) 700 hPa height. (d) Isosurface of $PM_{2.5}$ mass concentration over the nest at 5 µg m^{-3}, as seen from south of the nest. (e) Wind fields (m s^{-1}) (arrows) and Vertical wind speed (cm s^{-1}) (shaded colors) at 850 hPa height. Wind fields (m s^{-1}) (arrows), Vertical PM_{10} plume (µg m^{-3}) (shaded colours-left) and Vertical Wind Speed (cm s^{-1}) (shaded colours-right) along the red line in (c).

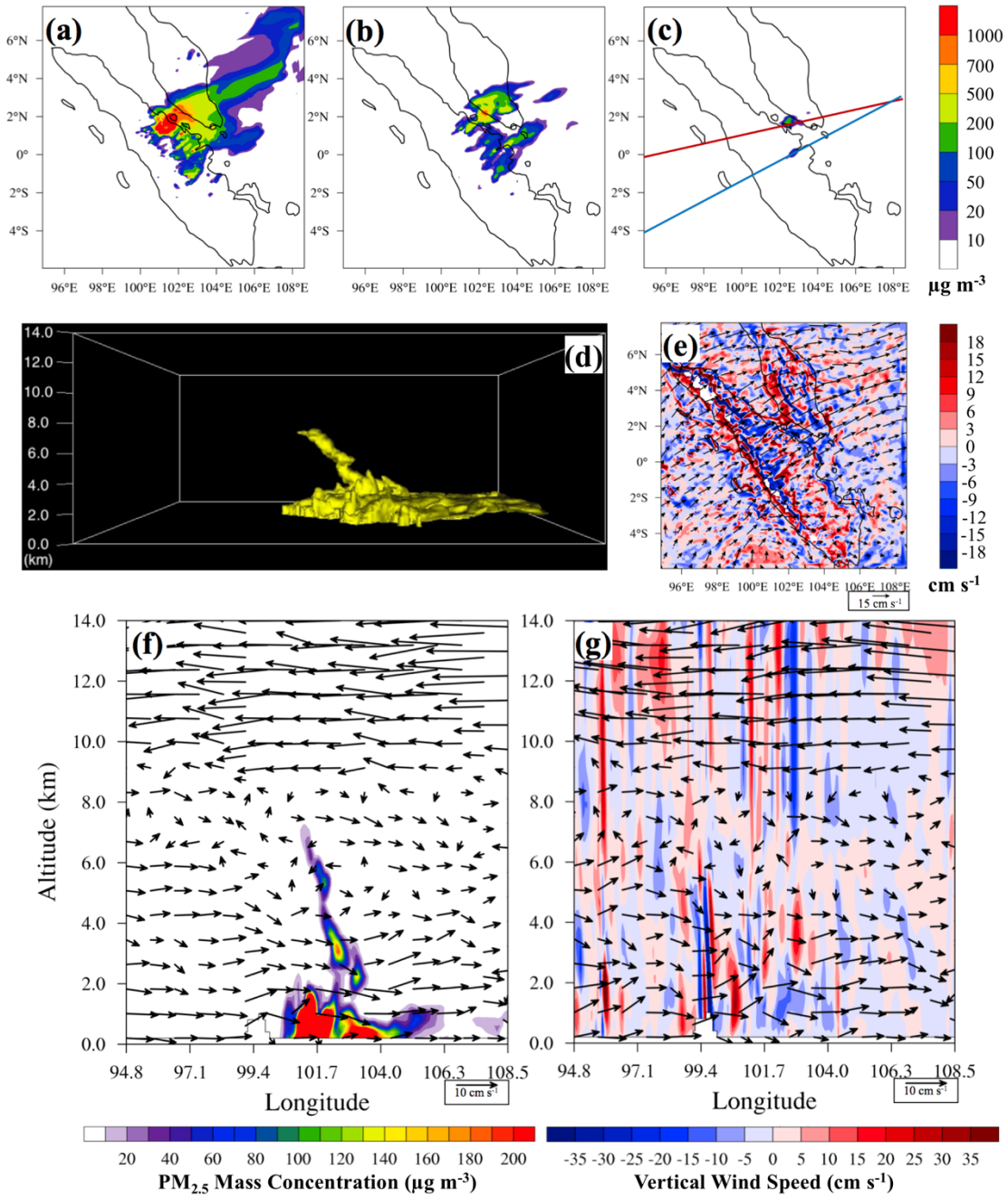


Figure 5.2 Same as Figure 5.1 but for the smoke plume at 11 UTC and vertical wind speed at 10 UTC on 20 June 2013.

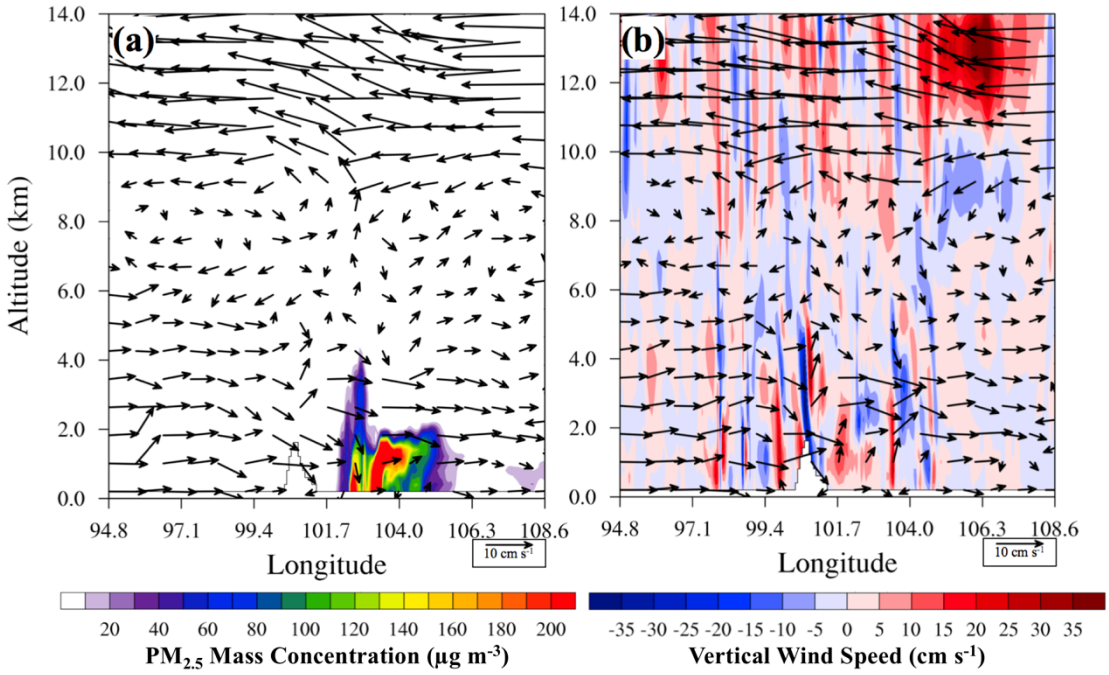


Figure 5.3 Wind fields (m s^{-1}) (arrows), Vertical PM_{10} plume (µg m^{-3}) (shaded colours-left) at 11 UTC and Vertical Wind Speed (cm s^{-1}) (shaded colours-right) at 10 UTC along the blue line in Figure 5.2(c) on 20 June 2013.

5.1.2 Convection over the Strait of Malacca

$PM_{2.5}$ concentrations were found to reach nearly 4 km in height due to a previously conjectured convergence over the Strait of Malacca. Fujita et al. (2010) describes the mechanism by which a morning maximum in the diurnal precipitation was formed by the convergence of cold outflows from SPM over the Strait. These outflows are generally produced by precipitation systems from the previous evening and converge over the Strait at around midnight.

In chapter 4, Figure 4.6 shows that by 24 June TC Bebinca had already made landfall over Vietnam and had lost in intensity. As a result, the wind direction shifted from a northeasterly direction to a northerly direction over SPM on that day. In addition, the wind vectors on Figure 5.4(e) show that the 850 hPa winds were much weaker than the winds that prevailed over the region on 19 and 20 June in Figures 5.1(e) and 5.2(e). While smoke concentrations barely reached the 700 hPa height, smoke was very prevalent near the surface and at the 850 hPa height over Riau and the Central and Northern region of Peninsular Malaysia, as shown by Figures 5.4(a – c). As a morning precipitation maximum forms (Fujita et al., 2010) between 22 UTC and 23 UTC over the strait of Malacca, a convective cell extending between 1.4 °S to 6 °N can be

observed along the cross-section in Figures 5.4(f) and (g). Low level convergence can be observed at 6 °N along the cross-section while upper level divergence can be observed at about 6 km in altitude. This convective cell entrained smoke within 2 km above the surface and was able to uplift smoke to a height of nearly 4 km.

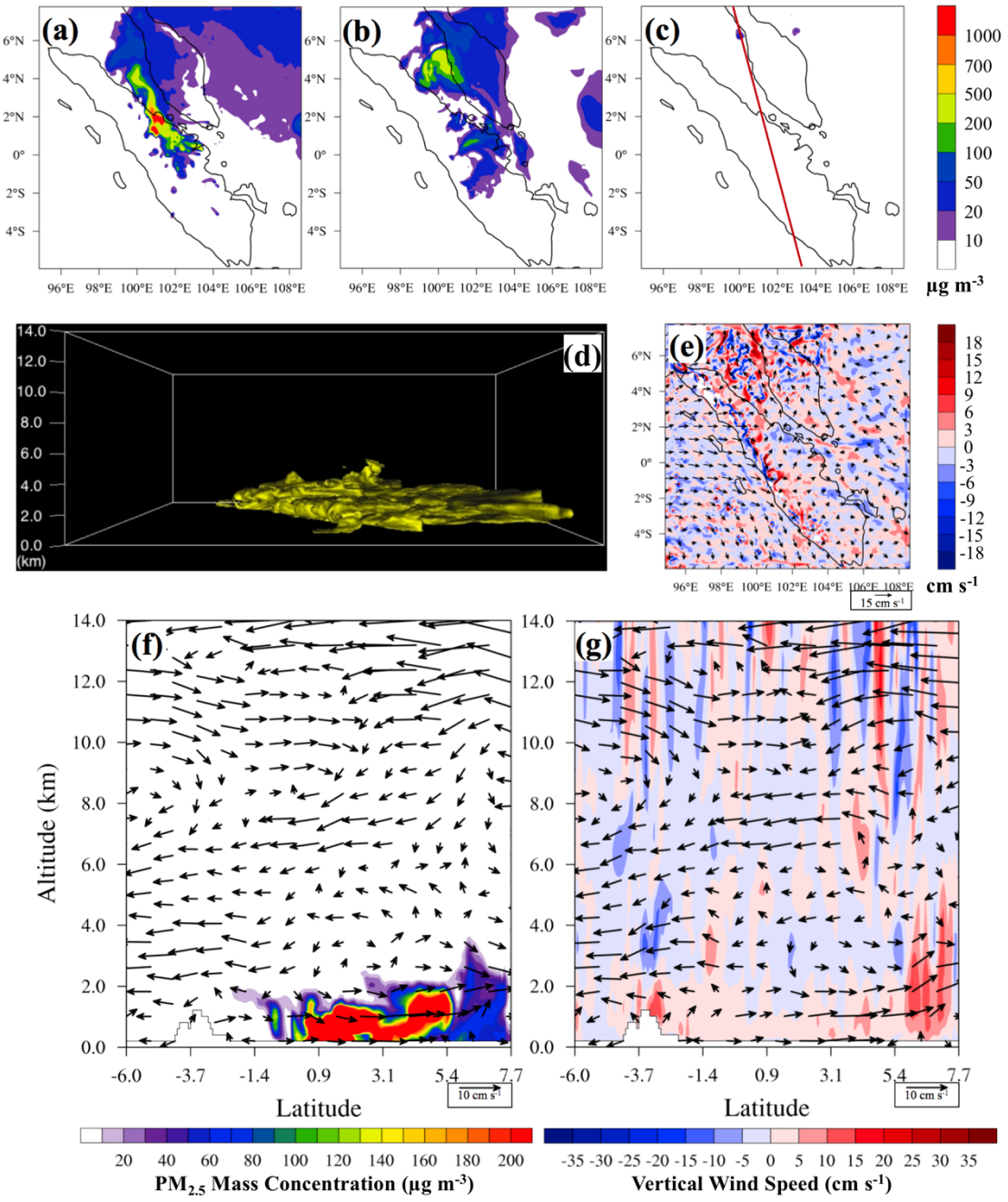


Figure 5.4 Same as Figure 5.1 but for the smoke plume at 23 UTC and vertical wind speed at 22 UTC on 24 June 2013.

5.1.3 Orographic Motion over Peninsular Malaysia

Figures 5.5 and 5.6 show that haze was uplifted to heights of at least 6 km and 10 km over Peninsular Malaysia on 24 and 25 June respectively. This deep convective transport can be attributed to a strong orographic effect which occurs as the wind is force-lifted over the slope on the West coast of Malaysia and its mountains deeper inland. Comparing these two days, it can be observed that on 25 June, more smoke reached the 850 hPa and 700 hPa heights, respectively, as compared to 24 June, as shown in Figures 5.5(b–c) and 5.6(b–c). In fact, on 25 June, the $PM_{2.5}$ concentrations at 850 hPa height were comparable to the near surface concentrations as shown in Figure 5.6(a) and (b). In addition, comparing Figures 5.5(f) and 5.6(f), it can be observed that the average plume height along the cross-section was confined to below 2 km on 24 June while on 25 June the average plume height was clearly more than 2 km. Comparing Figures 5.5(d) and 5.6(d) it can be seen that in general, the plume heights were higher on 25 June as compared to 24 June over the region. This can be attributed to reduced subsidence over the region due to TC Bebinca, as by 25 June the cyclone had already subsided allowing more convection to take place over the region. This drastic reduction in subsidence over the region can be clearly observed by comparing Figures 5.1(e) to 5.5(e). On 19 and 20 June, 850 hPa vertical wind speed plots show that downward vertical speeds of at least 18 cm s^{-1} prevailed over PSA while on 24 June downward vertical speeds over Riau and Peninsular Malaysia reached only around 6 cm s^{-1}. In contrast on 25 June, upward vertical motion predominated over Riau and Peninsular Malaysia at 850 hPa height. The resulting upward vertical motion, due to orography, reaching at least 35 cm s^{-1} at 3.1°N uplifted the smoke concentrations to at least 10 km in height. The uplifting of the biomass-burning emissions to such heights could have long range transport effects if the emissions are carried aloft by the prevailing upper level winds.

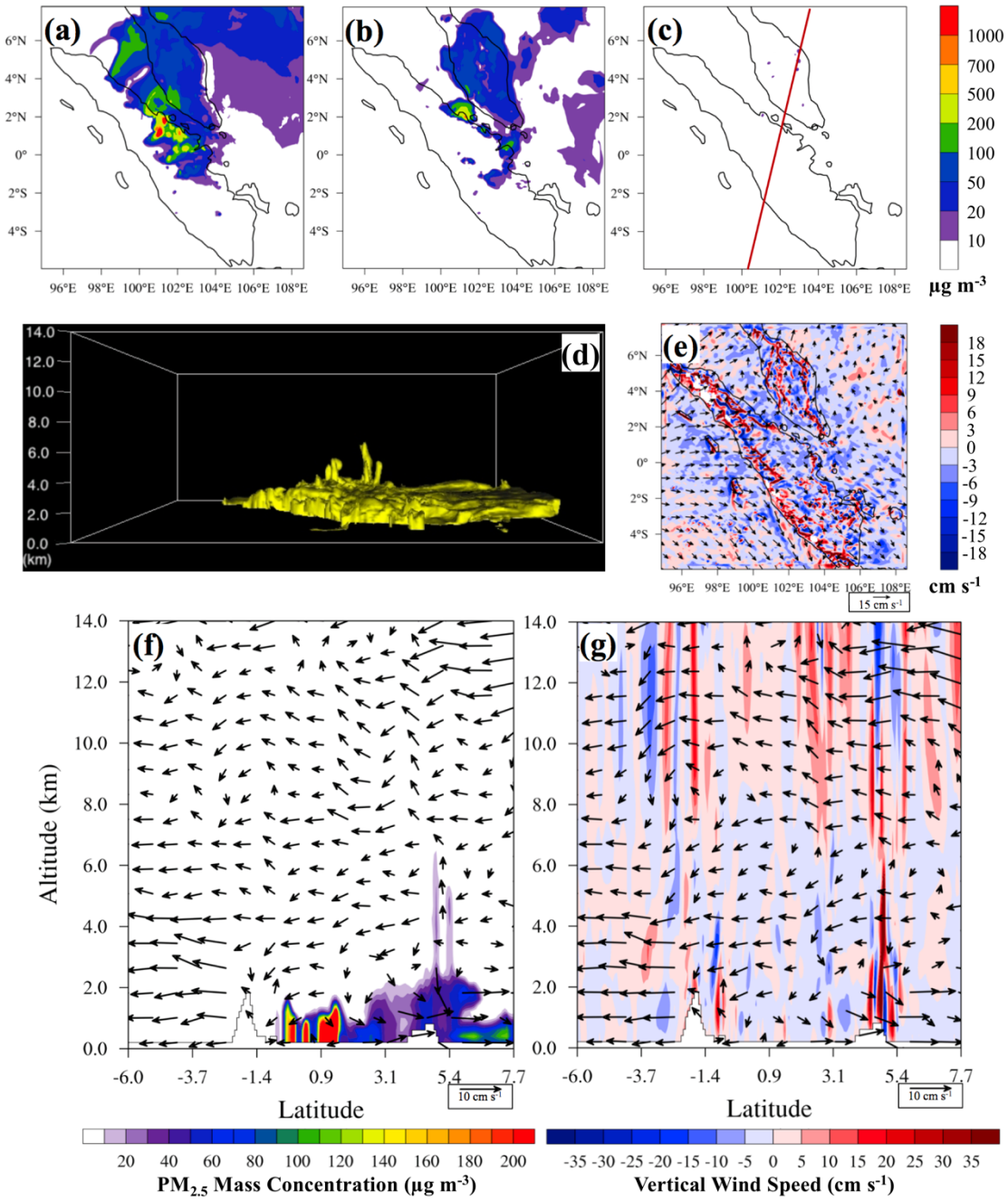


Figure 5.5 Same as Figure 5.1 but for the smoke plume at 10 UTC and vertical wind speed at 09 UTC on 24 June 2013.

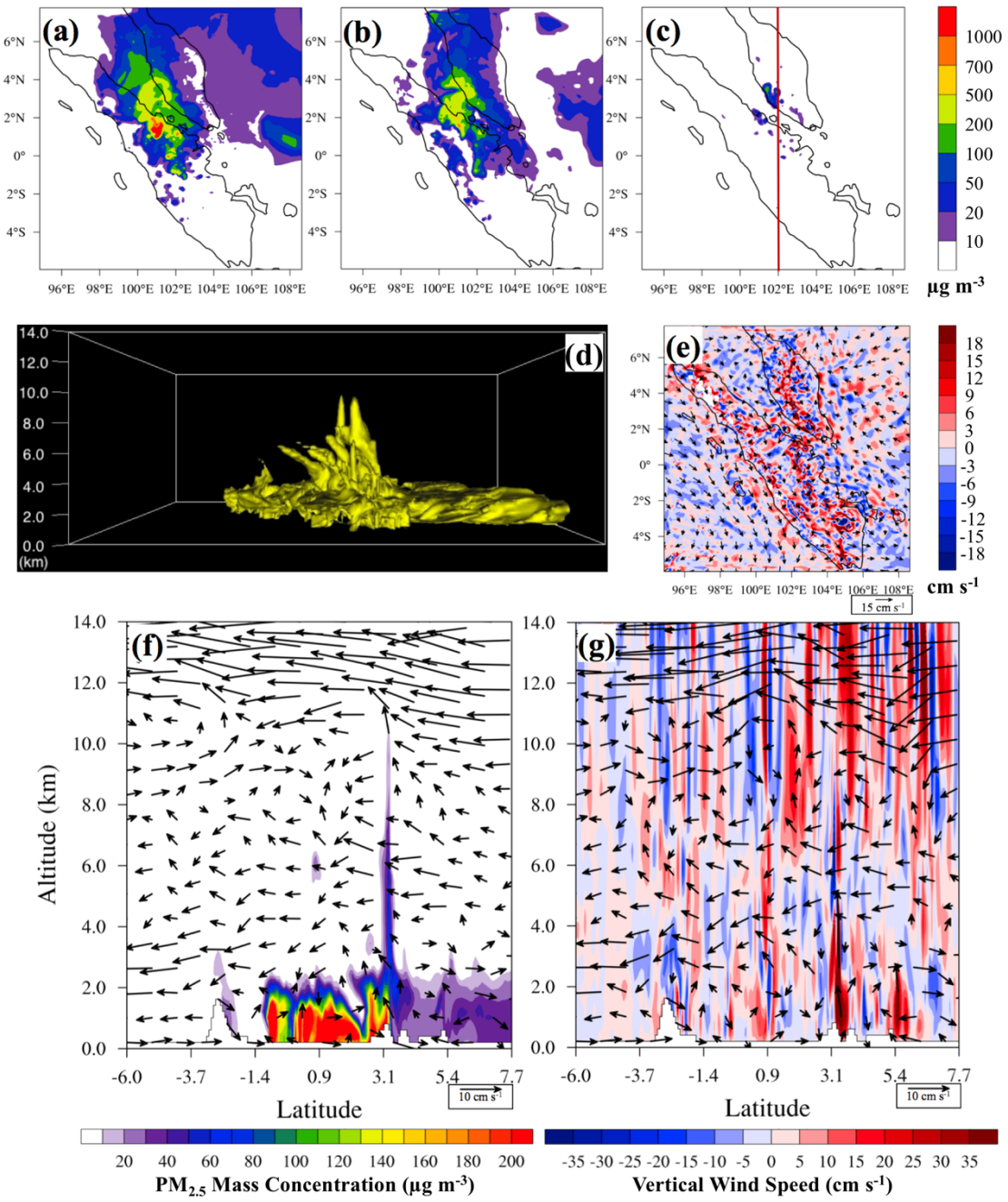


Figure 5.6 Same as Figure 5.1 but for the smoke plume at 12 UTC and vertical wind speed at 11 UTC on 25 June 2013.

5.2 Summary

The work presented in this chapter aimed at identifying the convective mechanisms which are responsible for uplifting haze within the troposphere, over Sumatra and Peninsular Malaysia. The WRF-Chem model simulation results for the study of the June 2013 episode were used to investigate and analyse haze transport over the 9 km model nest. This nest can resolve convection better than the main domain, owing to its

higher resolution. $PM_{2.5}$ mass concentration and vertical wind speed plots at different levels, namely, surface, 850 hPa and 700 hPa as well as vertical cross-sections of major smoke plumes were analysed. Three major convective mechanisms were identified.

Firstly, orographic motion over the Barisan Mountains in Sumatra was found to uplift smoke emissions to heights of at least 4 km on 19 and 20 June. Convection occurs on the lee side of the mountains as turbulent eddies are formed as air from the Indian Ocean blow over the mountains. On 20 June, two major plumes were observed, the highest reaching at least 7 km in height.

Secondly, a previously conjectured convergence over the Strait of Malacca was observed to uplift smoke to a height of about 4 km. This convergence occurs as cold outflows from Sumatra and Peninsular Malaysia form a morning maximum over the Strait in the morning. At 22 UTC on 24 June a convective cell extending up to 6 km in height formed as a result of low level convergence over the strait. This convective cell entrained smoke within 2 km above the surface and was able to uplift smoke to a height of nearly 4 km.

Finally, deep convective transport of smoke was observed due to a strong orographic effect which occurred as wind was force-lifted on the West coast of Malaysia and its mountains deeper in land, on 24 and 25 June. The maximum observed plume height reached around 6 km on 24 June while the maximum height was 10 km on 25 June. The higher average plume height on 25 June as compared to 24 June can be explained by the drastic reduction in subsidence which occurred as TC Bebinca subsided during these two days.

The uplifting of the biomass-burning emissions to such heights could have long range transport effects if the emissions are carried aloft by the prevailing upper level winds, hence the importance of identifying the mechanisms which are responsible for uplifting them.

6. CONCLUSION AND FUTURE WORK

6.1 Conclusion

Biomass-burning haze in Southeast Asia is an environmental issue which has gained much attention during the past few years. Not only does it have alarming detrimental effects but also its impact on the environment and the economy simply cannot be ignored. Therefore, numerous studies have been done to better understand and characterise the occurrence of haze episodes over Southeast Asia. While major haze episodes are known to occur during ENSO years, recently one of the worst cases of biomass-burning haze occurred in June 2013, which was a non-ENSO year. The air pollution indices over Malaysia and Singapore had reached hazardous levels during that episode and a state of emergency was declared in Malaysia. While the most significant fire events in the MC usually occur between August and early October during the southwest monsoon season, burning in June is not uncommon. However, the extreme magnitude of the June 2013 event was. Unfortunately, previous published work on that episode were limited to statistical studies of the impacts of haze on air quality and health. A major part of this study therefore aimed at investigating the meteorological environment that prevailed during the June 2013 haze event and the parameters which contributed to its intensification. The strong scale dependencies which interacted with each other to create the haze event, that is ENSO, the MJO and TC activity, are systematically examined. The WRF-Chem model was employed in order to study in detail the relative influence of TC activity, in particular TC Bebinca, on the haze event. The WRF-Chem model results were also used to study the convective mechanisms which uplift haze in the troposphere since the mechanisms over SPM are well under-studied. The uplifting of air pollutants to higher altitudes in Southeast Asia can have long-range transport effects if they are carried by upper level winds.

To determine the most suitable settings to be used in the WRF-Chem model, a set of sensitivity studies was performed to identify the WRF physics settings which best

represent the meteorology over the model domain during the June 2013 haze episode. The microphysics, cumulus parameterisation and planetary boundary layer schemes were investigated in the sensitivity study. Based on previous work, the following schemes were selected for the study: four microphysics schemes (Lin, WRF single-moment 6-class scheme (WSM6), Thompson and Morrison), three cumulus parameterisation schemes (Kain–Fritsch (KF), Betts–Miller–Janjic (BMJ) and Grell 3D – an improved version of Grell-Devenyi ensemble (GD) and two PBL schemes (Mellor-Yamada-Janjic (MYJ) and Yonsei University (YSU). A set of 13 single domain simulations were designed from these schemes for the sensitivity study and the results were compared for 17 to 25 June 2013. The sensitivity simulations results were evaluated with CMORPH precipitation data and observed data from ground stations over Malaysia. Overall the sensitivity simulation run with with the Lin microphysics, BMJ cumulus scheme and MYJ PBL scheme performed best. These settings were then used in a WRF-Chem nested model and the model was evaluated with CMORPH precipitation data, ground station data, and satellite data from CALIPSO and MODIS satellites. The model performed well at reproducing accumulated precipitation and successfully simulated the diurnal variation of 10 m wind speed and 2 m temperature. The model also successfully produced the patterns and magnitudes of AOT over the MC and captured the variations in plume height when compared to satellite data. Finally, the WRF-Chem model succeeded at reproducing the diurnal variation of smoke concentration at all ground stations included in the evaluation.

In order to study the June 2013 haze episode, before analysing the relevant WRF-Chem results, the aerosol and meteorological characteristics over Southeast Asia during the study period of 17 to 25 June 2013 were investigated using the aforementioned satellite and ground station data, in addition to meteorological indices. MODIS fire hotspot detections showed that fire activity was concentrated over Riau in Sumatra while CMORPH precipitation fields showed that the corresponding region was particularly dry. The AOT retrievals indicated that smoke was transported by southwesterlies, which prevail during the southwest monsoon season, towards the South China Sea where it was eventually scavenged out by precipitation associated with TC Bebinca. The MEI time-series from 1980 to 2016 showed that 2013 was indeed a neutral year and the MEI value for June 2013 was -0.144. Interestingly, MODIS fire counts observed over Sumatra and Peninsular Malaysia and the Maritime Continent for June

were the highest in 2013 as compared to any other year that MODIS Aqua and Terra satellites have been in operation and the highest ratio of fire count for Sumatra and Peninsular Malaysia to Maritime Continent was recorded in June 2013. An analysis of mean daily precipitation and MJO characteristics for the month of June for the years 2003 to 2015 suggested that the MJO induced subsidence contributed to increased burning over the region. Finally, the WRF-Chem results showed that TC Bebinca was found to have serious intensifying effects on the propagation of forest fires over Sumatra and the transport of haze over the MC. TC Bebinca was in fact formed during an early and active TC season in June 2013 as a result of the transiting MJO. The model results showed that subsidence associated with Bebinca and the dry phases of the MJO contributed to regions of dryness over Central Sumatra and the migration of Bebinca from the South China Sea onto Indochina governed the direction of plume flow from Sumatra. In fact, the extreme haze event of June 2013 coincided with the presence of TC Bebinca.

The results from the WRF-Chem model 9 km grid resolution nest were then used to investigate and identify the convective mechanisms which are responsible for uplifting haze within the troposphere, over Sumatra and Peninsular Malaysia. Three major convective mechanisms were identified. These are orographic motion over the Barisan Mountains of Indonesia, morning convergence over the strait of Malacca and orographic motion over Peninsular Malaysia. The later was found to have the most convective effect on the vertical transport of haze, lifting smoke to heights of at least 10 km in the atmosphere.

6.2 Future Work

The future work based on this thesis is twofold. Firstly, future work would include extending the study on subsidence over SPM. The combined subsidence due to both Bebinca and the MJO is a phenomenon which requires further attention since no haze event occurred when stronger Category 1 Rumbia crossed the SCS during the lesser dry phase 8 of the MJO over the MC. Therefore, a study focused on subsidence due to the MJO over Southeast Asia during a series of haze episodes would help determine the relative influence of the MJO on the occurrence of extreme haze episodes.

Finally, the convective mechanisms which uplift haze emissions to the upper troposphere have been identified. The present study only includes the transport of BBH

from the fire hotspots while excluding the radiative effects of these aerosols on the atmosphere. In particular the direct and indirect feedback effects of aerosols on the atmosphere and their interaction with clouds. Such a study of the aerosol radiative effect on the atmosphere during such uncharacteristic haze episodes will help provide an understanding of the effects of such episodes on climate.

REFERENCES

Ackermann, I.J., Hass, H., Memmesheimer, M., Ebel, A., Binkowski, F.S., Shankar, U., 1998. Modal Aerosol Dynamics model for Europe: Development and first applications. Atmos. Environ. 32, 2981–2999. doi:10.1016/S1352-2310(98)00006-5

Aditama, T.Y., 2000. Impact of haze from forest fire to respiratory health: Indonesian experience. Respirology 5, 169–174.

Ahrens, C., 2011. Essentials of meteorology: an invitation to the atmosphere, Sixth Edit. ed.

Aouizerats, B., van der Werf, G.R., Balasubramanian, R., Betha, R., 2015. Importance of transboundary transport of biomass burning emissions to regional air quality in Southeast Asia during a high fire event. Atmos. Chem. Phys. 15, 363–373. doi:10.5194/acp-15-363-2015

Arakawa, A., Schubert, W.H., 1974. Interaction of a Cumulus Cloud Ensemble with the Large-Scale Environment, Part I. J. Atmos. Sci. 31, 674–701. doi:10.1175/1520-0469(1974)031<0674:IOACCE>2.0.CO;2

Ashok, K., Behera, S.K., Rao, S.A., Weng, H., Yamagata, T., 2007. El Niño Modoki and its possible teleconnection. J. Geophys. Res. 112, C11007. doi:10.1029/2006JC003798

Berrisford, P., Dee, D.P., Fielding, K., Fuentes, M., Kallberg, P., Kobayashi, S., Uppala, S.M., 2009. The ERA-Interim Archive. ERA report series. Technical Report 1.

Betha, R., Behera, S.N., Balasubramanian, R., 2014. 2013 Southeast Asian smoke haze: Fractionation of particulate-bound elements and associated health risk. Environ. Sci. Technol. 48, 4327–4335. doi:10.1021/es405533d

Betha, R., Pradani, M., Lestari, P., Joshi, U.M., Reid, J.S., Balasubramanian, R., 2013. Chemical speciation of trace metals emitted from Indonesian peat fires for health risk assessment. Atmos. Res. 122, 571–578. doi:10.1016/j.atmosres.2012.05.024

Betts, A.K., 1986. A new convective adjustment scheme. Part I: Observational and theoretical basis. Q. J. R. Meteorol. Soc. 112, 677–691.

Betts, A.K., Miller, M.J., 1986. A new convective adjustment scheme. Part II: Single column tests using GATE wave, BOMEX, ATEX and arctic air-mass data sets. Q. J. R. Meteorol. Soc. 112, 693–709.

Brown, J.M., 1979. Mesoscale Unsaturated Downdrafts Driven by Rainfall Evaporation: A Numerical Study. J. Atmos. Sci. 36, 313–338. doi:10.1175/1520-0469(1979)036<0313:MUDDBR>2.0.CO;2

Bureau of Meteorology, 2013. Madden-Julian Oscillation (MJO). URL http://www.bom.gov.au/climate/mjo/ (accessed 10.1.16).

Chan, C.Y., Chan, L.Y., Harris, J.M., Oltmans, S.J., Blake, D.R., Qin, Y., Zheng, Y.G., Zheng, X.D., 2003. Characteristics of biomass burning emission sources, transport, and chemical speciation in enhanced springtime tropospheric ozone profile over Hong Kong. J. Geophys. Res. 108, 4015. doi:10.1029/2001JD001555

Chan, L.Y., Chan, C.Y., Liu, H.Y., Christopher, S., Oltmans, S.J., Harris, J.M., 2000. A case study on the biomass burning in southeast Asia and enhancement of tropospheric ozone over Hong Kong. Geophys. Res. Lett. 27, 1479–1482. doi:10.1029/1999GL010855

Chang, C.-P., Wang, Z., McBride, J., Liu, C.-H., 2005. Annual Cycle of Southeast Asia—Maritime Continent Rainfall and the Asymmetric Monsoon Transition. J. Clim. 18, 287–301. doi:10.1175/JCLI-3257.1

Chen, F., Dudhia, J., 2001. Coupling an Advanced Land Surface–Hydrology Model with the Penn State–NCAR MM5 Modeling System. Part I: Model Implementation and Sensitivity. Mon. Weather Rev. 129, 569–585. doi:10.1175/1520-0493(2001)129<0569:CAALSH>2.0.CO;2

Chen, L., Ding, Y., 1979. The Conspectus of Western Pacific Typhoon.

Chen, S.-H., Sun, W.-Y., 2002. A One-dimensional Time Dependent Cloud Model. J. Meteorol. Soc. Japan. Ser. II 80, 99–118. doi:10.2151/jmsj.80.99

Cheng, F.-Y., Yang, Z.-M., Ou-Yang, C.-F., Ngan, F., 2013. A numerical study of the

dependence of long-range transport of CO to a mountain station in Taiwan on synoptic weather patterns during the Southeast Asia biomass-burning season. Atmos. Environ. 78, 277–290. doi:10.1016/j.atmosenv.2013.03.020

Cheng, W.Y.Y., Steenburgh, W.J., 2005. Evaluation of surface sensible weather forecasts by the WRF and the Eta models over the western United States. Weather Forecast. 20, 812–821.

Choi, I.-J., Jin, E.K., Han, J.-Y., Kim, S.-Y., Kwon, Y., 2015. Sensitivity of diurnal variation in simulated precipitation during East Asian summer monsoon to cumulus parameterization schemes. J. Geophys. Res. Atmos. 120, 11,971-11,987. doi:10.1002/2015JD023810

Chotamonsak, C., Salathe, E.P., Kreasuwan, J., Chantara, S., 2012. Evaluation of precipitation simulations over Thailand using a WRF regional climate model. Chiang Mai J. Sci. 39, 623–628.

Chotamonsak, C., Salathé, E.P., Kreasuwan, J., Chantara, S., Siriwitayakorn, K., 2011. Projected climate change over Southeast Asia simulated using a WRF regional climate model. Atmos. Sci. Lett. 12, 213–219. doi:10.1002/asl.313

Coiffier, J., 2011. Fundamentals of Numerical Weather Prediction. Cambridge University Press, Cambridge. doi:10.1017/CBO9780511734458

Crutzen, P.J., Delany, A.C., Greenberg, J., Haagenson, P., Heidt, L., Lueb, R., Pollock, W., Seiler, W., Wartburg, A., Zimmerman, P., 1985. Tropospheric chemical composition measurements in Brazil during the dry season. J. Atmos. Chem. 2, 233–256.

Department of Environment Malaysia, 2017. Air Pollution Index of Malaysia. URL http://apims.doe.gov.my/public_v2/home.html (accessed 6.10.17).

Department of Environment Malaysia, 2013a. PM10 concentrations at Muar by the Malaysian Department of Environment: April to November 2013. URL https://www.doe.gov.my/portalv1/en/category/info-umum/info-kualiti-udara (accessed 3.6.17).

Department of Environment Malaysia, 2013b. API readings by the Malaysian

Department of Environment:16th to 26th June 2013. URL http://apims.doe.gov.my/apims/hourly1.php (accessed 9.15.13).

Dinku, T., Chidzambwa, S., Ceccato, P., Connor, S.J., Ropelewski, C.F., 2008. Validation of high-resolution satellite rainfall products over complex terrain. Int. J. Remote Sens. 29, 4097–4110. doi:10.1080/01431160701772526

Duda, J.D., 2011. WRF simulations of mesoscale convective systems at convection-allowing resolutions. Iowa State University.

Dyer, A.J., Hicks, B.B., 1970. Flux-gradient relationships in the constant flux layer. Q. J. R. Meteorol. Soc. 96, 715–721.

Fast, J.D., Gustafson, W.I., Easter, R.C., Zaveri, R.A., Barnard, J.C., Chapman, E.G., Grell, G.A., Peckham, S.E., 2006. Evolution of ozone, particulates, and aerosol direct radiative forcing in the vicinity of Houston using a fully coupled meteorology-chemistry-aerosol model. J. Geophys. Res. Atmos. 111, 1–29. doi:10.1029/2005JD006721

Field, P.R., Hogan, R.J., Brown, P.R.A., Illingworth, A.J., Choularton, T.W., Cotton, R.J., 2005. Parametrization of ice-particle size distributions for mid-latitude stratiform cloud. Q. J. R. Meteorol. Soc. 131, 1997–2017. doi:10.1256/qj.04.134

Field, R.D., Shen, S.S.P., 2008. Predictability of carbon emissions from biomass burning in Indonesia from 1997 to 2006. J. Geophys. Res. Biogeosciences 113, 1–17. doi:10.1029/2008JG000694

Field, R.D., van der Werf, G.R., Fanin, T., Fetzer, E.J., Fuller, R., Jethva, H., Levy, R., Livesey, N.J., Luo, M., Torres, O., Worden, H.M., 2016. Indonesian fire activity and smoke pollution in 2015 show persistent nonlinear sensitivity to El Niño-induced drought. Proc. Natl. Acad. Sci. 113, 9204–9209. doi:10.1073/pnas.1524888113

Field, R.D., van der Werf, G.R., Shen, S.S.P., 2009. Human amplification of drought-induced biomass burning in Indonesia since 1960. Nat. Geosci. 2, 185–188. doi:10.1038/ngeo443

Fisher, J. a., Jacob, D.J., Purdy, M.T., Kopacz, M., Le Sager, P., Carouge, C., Holmes,

C.D., Yantosca, R.M., Batchelor, R.L., Strong, K., Diskin, G.S., Fuelberg, H.E., Holloway, J.S., Hyer, E.J., McMillan, W.W., Warner, J., Streets, D.G., Zhang, Q., Wang, Y., Wu, S., 2010. Source attribution and interannual variability of Arctic pollution in spring constrained by aircraft (ARCTAS, ARCPAC) and satellite (AIRS) observations of carbon monoxide. Atmos. Chem. Phys. 10, 977–996. doi:10.5194/acp-10-977-2010

Folkins, I., Chatfield, R., Baumgardner, D., Proffitt, M., 1997. Biomass burning and deep convection in southeastern Asia: Results from ASHOE/MAESA. J. Geophys. Res. Atmos. 102, 13291–13299.

Fujita, M., Kimura, F., Yoshizaki, M., 2010. Morning Precipitation Peak over the Strait of Malacca under a Calm Condition. Mon. Weather Rev. 138, 1474–1486. doi:10.1175/2009MWR3068.1

Fujiwara, M., Kita, K., Kawakami, S., Ogawa, T., Komala, N., Saraspriya, S., Suripto, A., 1999. Tropospheric ozone enhancements during the Indonesian Forest Fire events in 1994 and in 1997 as revealed by ground-based observations.pdf. Geophys. Res. Lett. 26, 2417–2420.

Fuller, D.O., 2003. MODIS data used to study 2002 fires in Kalimantan, Indonesia. Eos, Trans. Am. Geophys. Union 84, 189–192. doi:10.1029/2003EO200001

Gao, M., Guttikunda, S.K., Carmichael, G.R., Wang, Y., Liu, Z., Stanier, C.O., Saide, P.E., Yu, M., 2015. Health impacts and economic losses assessment of the 2013 severe haze event in Beijing area. Sci. Total Environ. 511, 553–561. doi:10.1016/j.scitotenv.2015.01.005

Gao, Y., Zhao, C., Liu, X., Zhang, M., Leung, L.R., 2014. WRF-Chem simulations of aerosols and anthropogenic aerosol radiative forcing in East Asia. Atmos. Environ. 92, 250–266. doi:10.1016/j.atmosenv.2014.04.038

Ge, C., Wang, J., Reid, J.S., 2014. Mesoscale modeling of smoke transport over the Southeast Asian Maritime Continent: coupling of smoke direct radiative effect below and above the low-level clouds. Atmos. Chem. Phys. 14, 159–174. doi:10.5194/acp-14-159-2014

Ge, C., Wang, J., Reid, J.S., Posselt, D.J., Xian, P., Hyer, E., 2017. Mesoscale modeling

of smoke transport from equatorial Southeast Asian Maritime Continent to the Philippines: First comparison of ensemble analysis with in situ observations. J. Geophys. Res. Atmos. 122, 5380–5398. doi:10.1002/2016JD026241

GES DISC Northern Eurasian Earth Science Partnership Initiative Project, 2006a. MOD14CM1: MODIS/Terra 1 degree Gridded MODIS Active Fire Product V005. MODIS/Terra 1 degree Gridded MODIS Act. Fire Prod. V005, Greenbelt, MD, USA, Goddard Earth Sci. Data Inf. Serv. Cent. (GES DISC). URL http://disc.gsfc.nasa.gov/datacollection/MOD14CM1_005.html (accessed 4.1.16).

GES DISC Northern Eurasian Earth Science Partnership Initiative Project, 2006b. MYD14CM1: MODIS/Aqua 1 degree Gridded MODIS Active Fire Product V005. MODIS/Aqua 1 degree Gridded MODIS Act. Fire Prod. V005, Greenbelt, MD, USA, Goddard Earth Sci. Data Inf. Serv. Cent. (GES DISC). URL http://disc.gsfc.nasa.gov/datacollection/MYD14CM1_005.html (accessed 4.1.16).

Giglio, L., Csiszar, I., Justice, C.O., 2006. Global distribution and seasonality of active fires as observed with the Terra and Aqua Moderate Resolution Imaging Spectroradiometer (MODIS) sensors. J. Geophys. Res. Biogeosciences 111, n/a--n/a. doi:10.1029/2005JG000142

Giglio, L., Descloitres, J., Justice, C.O., Kaufman, Y.J., 2003. An Enhanced Contextual Fire Detection Algorithm for MODIS. Remote Sens. Environ. 87, 273–282. doi:10.1016/S0034-4257(03)00184-6

Gilmore, M.S., Straka, J.M., Rasmussen, E.N., 2004. Precipitation Uncertainty Due to Variations in Precipitation Particle Parameters within a Simple Microphysics Scheme. Mon. Weather Rev. 132, 2610–2627. doi:10.1175/MWR2810.1

Goh, A.Z.-C., Chan, J.C.L., 2010. Interannual and interdecadal variations of tropical cyclone activity in the South China Sea. Int. J. Climatol. 30, 827–843. doi:10.1002/joc.1943

Gómez-Navarro, J.J., Raible, C.C., Dierer, S., 2015. Sensitivity of the WRF model to PBL parametrisations and nesting techniques: Evaluation of wind storms over

complex terrain. Geosci. Model Dev. 8, 3349–3363. doi:10.5194/gmd-8-3349-2015

Gray, W.M., 1979. Hurricanes: Their formation, structure and likely role in the tropical circulation. Meteorol. over Trop. Ocean. 77, 155–218.

Grell, G.A., Dévényi, D., 2002. A generalized approach to parameterizing convection combining ensemble and data assimilation techniques. Geophys. Res. Lett. 29, 1693. doi:10.1029/2002GL015311

Grell, G. a., Peckham, S.E., Schmitz, R., McKeen, S. a., Frost, G., Skamarock, W.C., Eder, B., 2005. Fully coupled "online" chemistry within the WRF model. Atmos. Environ. 39, 6957–6975. doi:10.1016/j.atmosenv.2005.04.027

Hamada, Y., Darung, U., Limin, S.H., Hatano, R., 2013. Characteristics of fire-generated gas emission observed during a large peatland fire in 2009 at Kalimantan, Indonesia. Atmos. Environ. 74, 177–181. doi:10.1016/j.atmosenv.2013.03.058

Han, J., Pan, H.-L., 2011. Revision of Convection and Vertical Diffusion Schemes in the NCEP Global Forecast System. Weather Forecast. 26, 520–533. doi:10.1175/WAF-D-10-05038.1

Heath, N.K., Fuelberg, H.E., 2014. Using a WRF simulation to examine regions where convection impacts the Asian summer monsoon anticyclone. Atmos. Chem. Phys. 14, 2055–2070. doi:10.5194/acp-14-2055-2014

Heymsfield, A.J., Donner, L.J., 1990. A Scheme for Parameterizing Ice-Cloud Water Content in General Circulation Models. J. Atmos. Sci. 47, 1865–1877. doi:10.1175/1520-0469(1990)047<1865:ASFPIC>2.0.CO;2

Ho, R.C., Zhang, M.W., Ho, C.S., Pan, F., Lu, Y., Sharma, V.K., 2014. Impact of 2013 south Asian haze crisis: study of physical and psychological symptoms and perceived dangerousness of pollution level. BMC Psychiatry 14, 81. doi:10.1186/1471-244X-14-81

Hong, S.-Y., Dudhia, J., Chen, S.-H., 2004. A Revised Approach to Ice Microphysical Processes for the Bulk Parameterization of Clouds and Precipitation. Mon.

Weather Rev. 132, 103–120. doi:10.1175/1520-0493(2004)132<0103:ARATIM>2.0.CO;2

Hong, S.-Y., Noh, Y., Dudhia, J., 2006. A New Vertical Diffusion Package with an Explicit Treatment of Entrainment Processes. Mon. Weather Rev. 134, 2318–2341. doi:10.1175/MWR3199.1

Hong, S., Lim, J., 2006. The WRF single-moment 6-class microphysics scheme (WSM6). J. Korean Meteorol. Soc.

Houze Jr, R.A., 2012. OROGRAPHIC EFFECTS ON PRECIPITATING CLOUDS. Rev. Geophys. 50, 2011RG000365. doi:10.1029/2011RG000365

Iacono, M.J., Delamere, J.S., Mlawer, E.J., Shephard, M.W., Clough, S. a., Collins, W.D., 2008. Radiative forcing by long-lived greenhouse gases: Calculations with the AER radiative transfer models. J. Geophys. Res. 113, D13103. doi:10.1029/2008JD009944

Janjic, Z.., 2002. Nonsingular Implementation of the Mellor-Yamada Level 2 . 5 Scheme in the NCEP Meso model. NCEP Off. Note 437, 1–61.

Janjic, Z.., 1996. The surface layer in the NCEP Eta Model, in: Eleventh Conference on Numerical Weather Prediction,Norfolk, VA. American Meteorological Society, pp. 354–355.

Janjić, Z.I., 2000. Comments on "Development and Evaluation of a Convection Scheme for Use in Climate Models." J. Atmos. Sci. 57, 3686–3686. doi:10.1175/1520-0469(2000)057<3686:CODAEO>2.0.CO;2

Janjić, Z.I., 1994. The Step-Mountain Eta Coordinate Model: Further Developments of the Convection, Viscous Sublayer, and Turbulence Closure Schemes. Mon. Weather Rev. 122, 927–945. doi:10.1175/1520-0493(1994)122<0927:TSMECM>2.0.CO;2

Janowiak, J.E., Kousky, V.E., Joyce, R.J., 2005. Diurnal cycle of precipitation determined from the CMORPH high spatial and temporal resolution global precipitation analyses. J. Geophys. Res. 110, D23105. doi:10.1029/2005JD006156

Jiménez, P.A., Dudhia, J., 2012. Improving the Representation of Resolved and Unresolved Topographic Effects on Surface Wind in the WRF Model. J. Appl. Meteorol. Climatol. 51, 300–316. doi:10.1175/JAMC-D-11-084.1

Joint Typhoon Warning Center, 2013. Annual Tropical Cyclone Report 2013.

Joyce, R.J., Janowiak, J.E., Arkin, P. a., Xie, P., 2004. CMORPH: A Method that Produces Global Precipitation Estimates from Passive Microwave and Infrared Data at High Spatial and Temporal Resolution. J. Hydrometeorol. 5, 487–503. doi:10.1175/1525-7541(2004)005<0487:CAMTPG>2.0.CO;2

Justice, C., Giglio, L., Korontzi, S., Owens, J., Morisette, J., Roy, D., Descloitres, J., Alleaume, S., Petitcolin, F., Kaufman, Y., 2002. The MODIS fire products. Remote Sens. Environ. 83, 244–262. doi:10.1016/S0034-4257(02)00076-7

Kain, J.S., 2004. The Kain–Fritsch Convective Parameterization: An Update. J. Appl. Meteorol. 43, 170–181. doi:10.1175/1520-0450(2004)043<0170:TKCPAU>2.0.CO;2

Kain, J.S., Fritsch, J.M., 1992. The role of the convective “trigger function” in numerical forecasts of mesoscale convective systems. Meteorol. Atmos. Phys. 49, 93–106. doi:10.1007/BF01025402

Kessler, E., 1969. On the Distribution and Continuity of Water Substance in Atmospheric Circulations, in: On the Distribution and Continuity of Water Substance in Atmospheric Circulations. American Meteorological Society, Boston, MA, pp. 1–84. doi:10.1007/978-1-935704-36-2_1

Kim, J.-H., Ho, C.-H., Kim, H.-S., Sui, C.-H., Park, S.K., 2008. Systematic Variation of Summertime Tropical Cyclone Activity in the Western North Pacific in Relation to the Madden–Julian Oscillation. J. Clim. 21, 1171–1191. doi:10.1175/2007JCLI1493.1

Oanh, N.T.K., Bich, T.L., Tipayarom, D., Manadhar, B.R., Prapat, P., Simpson, C.D., Liu, L.-J.S., 2011. Characterization of Particulate Matter Emission From Open Burning of Rice Straw. Atmos. Environ. (1994). 45, 493–502. doi:10.1016/j.atmosenv.2010.09.023

Klich, C.A., Fuelberg, H.E., 2014. The role of horizontal model resolution in assessing the transport of CO in a middle latitude cyclone using WRF-Chem. Atmos. Chem. Phys. 14, 609–627. doi:10.5194/acp-14-609-2014

Krishnamurti, T.N., Low-Nam, S., Pasch, R., 1983. Cumulus Parameterization and Rainfall Rates II. Mon. Weather Rev. 111, 815–828. doi:10.1175/1520-0493(1983)111<0815:CPARRI>2.0.CO;2

Kumar, R., Naja, M., Pfister, G.G., Barth, M.C., Brasseur, G.P., 2012. Simulations over South Asia using the Weather Research and Forecasting model with Chemistry (WRF-Chem): set-up and meteorological evaluation. Geosci. Model Dev. 5, 321–343. doi:10.5194/gmd-5-321-2012

Kunii, O., Kanagawa, S., Yajima, I., Hisamatsu, Y., Yamamura, S., Amagai, T., Ismail, I.T.S., 2002. The 1997 Haze Disaster in Indonesia: Its Air Quality and Health Effects. Arch. Environ. Heal. An Int. J. 57, 16–22. doi:10.1080/00039890209602912

Kwun, J.H., Kim, Y.-K., Seo, J.-W., Jeong, J.H., You, S.H., 2009. Sensitivity of MM5 and WRF mesoscale model predictions of surface winds in a typhoon to planetary boundary layer parameterizations. Nat. hazards 51, 63–77.

Laprise, R., 1992. The Euler Equations of Motion with Hydrostatic Pressure as an Independent Variable. Mon. Weather Rev. doi:10.1175/1520-0493(1992)120<0197:TEEOMW>2.0.CO;2

Levy, R.C., Mattoo, S., Munchak, L.A., Remer, L.A., Sayer, A.M., Patadia, F., Hsu, N.C., 2013. The Collection 6 MODIS aerosol products over land and ocean. Atmos. Meas. Tech. 6, 2989–3034. doi:10.5194/amt-6-2989-2013

Lim, K.-S.S., Hong, S.-Y., 2010. Development of an Effective Double-Moment Cloud Microphysics Scheme with Prognostic Cloud Condensation Nuclei (CCN) for Weather and Climate Models. Mon. Weather Rev. 138, 1587–1612. doi:10.1175/2009MWR2968.1

Lin, C.-Y., Hsu, H., Lee, Y.H., Kuo, C.H., Sheng, Y., Chu, D.A., 2009. A new transport mechanism of biomass burning from Indochina as identified by modeling studies. Atmos. Chem. Phys. 7901–7911.

Lin, C.-Y., Zhao, C., Liu, X., Lin, N.-H., Chen, W.-N., 2014. Modelling of long-range transport of Southeast Asia biomass-burning aerosols to Taiwan and their radiative forcings over East Asia. Tellus B 66. doi:10.3402/tellusb.v66.23733

Lin, Y.-L., Farley, R.D., Orville, H.D., 1983. Bulk Parameterization of the Snow Field in a Cloud Model. J. Clim. Appl. Meteorol. 22, 1065–1092. doi:10.1175/1520-0450(1983)022<1065:BPOTSF>2.0.CO;2

Lin, Y., Colle, B.A., 2011. A New Bulk Microphysical Scheme That Includes Riming Intensity and Temperature-Dependent Ice Characteristics. Mon. Weather Rev. 139, 1013–1035. doi:10.1175/2010MWR3293.1

Liu, H., Chang, W.L., Oltmans, S.J., Chan, L.Y., Harris, J.M., 1999. On springtime high ozone events in the lower troposphere from Southeast Asian biomass burning. Atmos. Environ. 33, 2403–2410. doi:10.1016/S1352-2310(98)00357-4

Ma, L.-M., Tan, Z.-M., 2009. Improving the behavior of the cumulus parameterization for tropical cyclone prediction: Convection trigger. Atmos. Res. 92, 190–211.

Madden, R.A., Julian, P.R., 1971. Detection of a 40–50 Day Oscillation in the Zonal Wind in the Tropical Pacific. J. Atmos. Sci. 28, 702–708. doi:10.1175/1520-0469(1971)028<0702:DOADOI>2.0.CO;2

Mahmud, M., 2009. Mesoscale equatorial wind prediction in Southeast Asia during a haze episode of 2005. Geofizika 26, 67–84.

Maloney, E.D., Hartmann, D.L., 2001. The Madden–Julian Oscillation, Barotropic Dynamics, and North Pacific Tropical Cyclone Formation. Part I: Observations. J. Atmos. Sci. 58, 2545–2558. doi:10.1175/1520-0469(2001)058<2545:TMJOBD>2.0.CO;2

Mapes, B.E., Warner, T.T., Xu, M., 2003. Diurnal Patterns of Rainfall in Northwestern South America. Part III: Diurnal Gravity Waves and Nocturnal Convection Offshore. Mon. Weather Rev. 131, 830–844. doi:10.1175/1520-0493(2003)131<0830:DPORIN>2.0.CO;2

Mass, C., Ovens, D., 2011. Fixing WRF's high speed wind bias: a new subgrid scale drag parameterization and the role of detailed verification, in: 24th Conference on

Weather and Forecasting and 20th Conference on Numerical Weather Prediction, Preprints, 91st American Meteorological Society Annual Meeting.

McBride, J.L., Haylock, M.R., Nicholls, N., 2003. Relationships between the Maritime Continent Heat Source and the El Niño–Southern Oscillation Phenomenon. J. Clim. 16, 2905–2914. doi:10.1175/1520-0442(2003)016<2905:RBTMCH>2.0.CO;2

Mellor, G.L., Yamada, T., 1982. Development of a turbulence closure model for geophysical fluid problems. Rev. Geophys. 20, 851–875.

Menendez, M., García-Díez, M., Fita, L., Fernández, J., Méndez, F.J., Gutiérrez, J.M., 2014. High-resolution sea wind hindcasts over the Mediterranean area. Clim. Dyn. 42, 1857–1872. doi:10.1007/s00382-013-1912-8

Miettinen, J., Liew, S.C., 2009. Burn-scar patterns and their effect on regional burnt-area mapping in insular South-East Asia. Int. J. Wildl. Fire 18, 837. doi:10.1071/WF08102

Monin, A.S., Obukhov, A.M.F., 1954. Basic laws of turbulent mixing in the surface layer of the atmosphere. Contrib. Geophys. Inst. Acad. Sci. USSR 151, e187.

Moron, V., Robertson, A.W., Boer, R., 2009. Spatial Coherence and Seasonal Predictability of Monsoon Onset over Indonesia. J. Clim. 22, 840–850. doi:10.1175/2008JCLI2435.1

Morrison, H., Curry, J.A., Shupe, M.D., Zuidema, P., 2005. A New Double-Moment Microphysics Parameterization for Application in Cloud and Climate Models. Part II: Single-Column Modeling of Arctic Clouds. J. Atmos. Sci. 62, 1678–1693. doi:10.1175/JAS3447.1

Morrison, H., Pinto, J.O., 2006. Intercomparison of bulk cloud microphysics schemes in mesoscale simulations of springtime Arctic mixed-phase stratiform clouds. Mon. Weather Rev. 134, 1880–1900.

Morrison, H., Thompson, G., Tatarskii, V., 2009. Impact of Cloud Microphysics on the Development of Trailing Stratiform Precipitation in a Simulated Squall Line: Comparison of One- and Two-Moment Schemes. Mon. Weather Rev. 137, 991–

1007. doi:10.1175/2008MWR2556.1

Napitu, A.M., Gordon, A.L., Pujiana, K., 2015. Intraseasonal Sea Surface Temperature Variability across the Indonesian Seas*. J. Clim. 28, 8710–8727. doi:10.1175/JCLI-D-14-00758.1

NASA Calipso, 2013. NASA Calipso. URL https://subset.larc.nasa.gov/calipso/login.php (accessed 11.1.16).

NASA Giovanni, 2013. NASA Giovanni. URL https://giovanni.gsfc.nasa.gov/giovanni/ (accessed 11.1.16).

NASA Worldview, 2013. NASA Worldview. URL https://earthdata.nasa.gov/labs/worldview/ (accessed 9.1.13).

Neumann, C.J., 1993. Global overview. Glob. Guid. to Trop. cyclone Forecast. 560.

Nichol, J., 1998. Smoke haze in Southeast Asia: A predictable recurrence. Atmos. Environ. 32, 2715–2716.

NOAA, 2016. Weather Research and Forecasting model coupled to Chemistry (WRF-Chem). URL https://ruc.noaa.gov/wrf/wrf-chem/ (accessed 3.1.16).

NOAA, 2015. Multivariate ENSO Index (MEI). URL https://www.esrl.noaa.gov/psd/enso/mei/table.html (accessed 4.1.16).

Oozeer, M.Y., Chan, A., Ooi, M.C.-G., Zarzur, A.M., Salinas, S.V., Chew, B.-N., Morris, K.I., Choong, W.-K., 2016. Numerical Study of the Transport and Convective Mechanisms of Biomass Burning Haze in South-Southeast Asia. Aerosol Air Qual. Res. 16, 2950–2963. doi:10.4209/aaqr.2015.07.0461

Osuri, K.K., Mohanty, U.C., Routray, A., Kulkarni, M.A., Mohapatra, M., 2012. Customization of WRF-ARW model with physical parameterization schemes for the simulation of tropical cyclones over North Indian Ocean. Nat. Hazards 63, 1337–1359. doi:10.1007/s11069-011-9862-0

Pahlow, M., Kleissl, J., Parlange, M.B., 2005. Atmospheric boundary-layer structure observed during a haze event due to forest-fire smoke. Boundary-Layer Meteorol. 114, 53–70. doi:10.1007/s10546-004-6350-z

Pan, H.L., Wu, W.S., 1995. Implementing a mass flux convective parameterization package for the NMC medium range forecast model, NMC office note, 409, 40 pp. Natl. Cent. Environ. Predict. CampSprings, Md.

Patil, R., Pradeep Kumar, P., 2016. WRF model sensitivity for simulating intense western disturbances over North West India. Model. Earth Syst. Environ. 2, 82. doi:10.1007/s40808-016-0137-3

Paulson, C.A., 1970. The mathematical representation of wind speed and temperature profiles in the unstable atmospheric surface layer. J. Appl. Meteorol. 9, 857–861.

Pennelly, C., Reuter, G., Flesch, T., 2014. Verification of the WRF model for simulating heavy precipitation in Alberta. Atmos. Res. 135–136, 172–192. doi:10.1016/j.atmosres.2013.09.004

Quah, E., 2002. Transboundary Pollution in Southeast Asia: The Indonesian Fires. World Dev. 30, 429–441. doi:10.1016/S0305-750X(01)00122-X

Quah, E., Johnston, D., 2001. Forest fires and environmental haze in Southeast Asia: using the "stakeholder" approach to assign costs and responsibilities. J. Environ. Manage. 63, 181–191. doi:10.1006/jema.2001.0475

Que, L.-J., Que, W.-L., Feng, J.-M., 2016. Intercomparison of different physics schemes in the WRF model over the Asian summer monsoon region. Atmos. Ocean. Sci. Lett. 9, 169–177. doi:10.1080/16742834.2016.1158618

Radojevic, M., 2003. Chemistry of Forest Fires and Regional Haze with Emphasis on Southeast Asia. Pure Appl. Geophys. 160, 157–187. doi:10.1007/s00024-003-8771-x

Rajeevan, M., Kesarkar, A., Thampi, S.B., Rao, T.N., Radhakrishna, B., Rajasekhar, M., 2010. Sensitivity of WRF cloud microphysics to simulations of a severe thunderstorm event over Southeast India. Ann. Geophys. 28, 603–619. doi:10.5194/angeo-28-603-2010

Raju, P.V.S., Potty, J., Mohanty, U.C., 2011. Sensitivity of physical parameterizations on prediction of tropical cyclone Nargis over the Bay of Bengal using WRF model. Meteorol. Atmos. Phys. 113, 125–137. doi:10.1007/s00703-011-0151-y

Raktham, C., Bruyère, C., Kreasuwun, J., Done, J., Thongbai, C., Promnopas, W., 2014. Simulation sensitivities of the major weather regimes of the Southeast Asia region. Clim. Dyn. 1403–1417. doi:10.1007/s00382-014-2156-y

Ramanathan, V., Crutzen, P.J., 2003. New Directions: Atmospheric Brown "Clouds." Atmos. Environ. 37, 4033–4035. doi:10.1016/S1352-2310(03)00536-3

Rasmusson, E.M., Wallace, J.M., 1983. Meteorological aspects of the El Nino/southern oscillation. Science (80-.). 222, 1195–1202.

Reid, J.S., Hyer, E.J., Johnson, R.S., Holben, B.N., Yokelson, R.J., Zhang, J., Campbell, J.R., Christopher, S.A., Di Girolamo, L., Giglio, L., Holz, R.E., Kearney, C., Miettinen, J., Reid, E. a., Turk, F.J., Wang, J., Xian, P., Zhao, G., Balasubramanian, R., Chew, B.N., Janjai, S., Lagrosas, N., Lestari, P., Lin, N.-H., Mahmud, M., Nguyen, A.X., Norris, B., Oanh, N.T.K., Oo, M., Salinas, S. V., Welton, E.J., Liew, S.C., 2013. Observing and understanding the Southeast Asian aerosol system by remote sensing: An initial review and analysis for the Seven Southeast Asian Studies (7SEAS) program. Atmos. Res. 122, 403–468. doi:10.1016/j.atmosres.2012.06.005

Reid, J.S., Hyer, E.J., Prins, E.M., Westphal, D.L., Zhang, J., Wang, J., Christopher, S.A., Curtis, C.A., Schmidt, C.C., Eleuterio, D.P., Richardson, K. a., Hoffman, J.P., 2009. Global monitoring and forecasting of biomass-burning smoke: Description of and lessons from the fire Locating and Modeling of Burning Emissions (FLAMBE) program. IEEE J. Sel. Top. Appl. Earth Obs. Remote Sens. 2, 144–162. doi:10.1109/JSTARS.2009.2027443

Reid, J.S., Koppmann, R., Eck, T.F., Eleuterio, D.P., 2005. A review of biomass burning emissions part II : intensive physical properties of biomass burning particles. Atmos. Chem. Phys. Discuss. 4, 799–825. doi:10.5194/acpd-4-5135-2004

Reid, J.S., Lagrosas, N.D., Jonsson, H.H., Reid, E.A., Atwood, S.A., Boyd, T.J., Ghate, V.P., Lynch, P., Posselt, D.J., Simpas, J.B., Uy, S.N., Zaiger, K., Blake, D.R., Bucholtz, A., Campbell, J.R., Chew, B.N., Cliff, S.S., Holben, B.N., Holz, R.E., Hyer, E.J., Kreidenweis, S.M., Kuciaskas, A.P., Lolli, S., Oo, M., Perry, K.D., Salinas, S. V., Sessions, W.R., Smirnov, A., Walker, A.L., Wang, Q., Yu, L.,

Zhang, J., Zhao, Y., 2016. Aerosol meteorology and Philippine receptor observations of Maritime Continent aerosol emissions for the 2012 7SEAS southwest monsoon intensive study. Atmos. Chem. Phys. Discuss. 1–61. doi:10.5194/acp-2016-214

Reid, J.S., Lagrosas, N.D., Jonsson, H.H., Reid, E.A., Sessions, W.R., Simpas, J.B., Uy, S.N., Boyd, T.J., Atwood, S.A., Blake, D.R., Campbell, J.R., Cliff, S.S., Holben, B.N., Holz, R.E., Hyer, E.J., Lynch, P., Meinardi, S., Posselt, D.J., Richardson, K.A., Salinas, S. V., Smirnov, A., Wang, Q., Yu, L., Zhang, J., 2015. Observations of the temporal variability in aerosol properties and their relationships to meteorology in the summer monsoonal South China Sea/East Sea: the scale-dependent role of monsoonal flows, the Madden–Julian Oscillation, tropical cyclones, squall l. Atmos. Chem. Phys. 15, 1745–1768. doi:10.5194/acp-15-1745-2015

Reid, J.S., Prins, E.M., Westphal, D.L., Schmidt, C.C., Richardson, K.A., Christopher, S.A., Eck, T.F., Reid, E.A., Curtis, C.A., Hoffman, J.P., 2004. Real-time monitoring of South American smoke particle emissions and transport using a coupled remote sensing/box-model approach. Geophys. Res. Lett. 31, n/a-n/a. doi:10.1029/2003GL018845

Reid, J.S., Xian, P., Hyer, E.J., Flatau, M.K., Ramirez, E.M., Turk, F.J., Sampson, C.R., Zhang, C., Fukada, E.M., Maloney, E.D., 2012. Multi-scale meteorological conceptual analysis of observed active fire hotspot activity and smoke optical depth in the Maritime Continent. Atmos. Chem. Phys. 12, 2117–2147. doi:10.5194/acp-12-2117-2012

Rivière, E.D., Marécal, V., Larsen, N., Cautenet, S., 2006. Modelling study of the impact of deep convection on the UTLS air composition – Part 2: Ozone budget in the TTL. Atmos. Chem. Phys. 6, 1585–1598. doi:10.5194/acp-6-1585-2006

Rogers, E., Black, T., Ferrier, B., Lin, Y., Parrish, D., DiMego, G., 2001. Changes to the NCEP Meso Eta Analysis and Forecast System: Increase in resolution, new cloud microphysics, modified precipitation assimilation, modified 3DVAR analysis. NWS Tech. Proced. Bull. 488, 15.

Rutledge, S.A., Hobbs, P.V., 1984. The Mesoscale and Microscale Structure and

Organization of Clouds and Precipitation in Midlatitude Cyclones. XII: A Diagnostic Modeling Study of Precipitation Development in Narrow Cold-Frontal Rainbands. J. Atmos. Sci. doi:10.1175/1520-0469(1984)041<2949:TMAMSA>2.0.CO;2

Rutledge, S.A., Hobbs, P., 1983. The Mesoscale and Microscale Structure and Organization of Clouds and Precipitation in Midlatitude Cyclones. VIII: A Model for the "Seeder-Feeder" Process in Warm-Frontal Rainbands. J. Atmos. Sci. 40, 1185–1206. doi:10.1175/1520-0469(1983)040<1185:TMAMSA>2.0.CO;2

Santos-Alamillos, F.J., Zquez, D.P.V., Ruiz-Arias, J.A., Lara-Fanego, V., Tovar-Pescador, J., 2013. Analysis of WRF model wind estimate sensitivity to physics parameterization choice and terrain representation in Andalusia (Southern Spain). J. Appl. Meteorol. Climatol. 52, 1592–1609. doi:10.1175/JAMC-D-12-0204.1

Sapiano, M.R.P., Arkin, P.A., 2009. An Intercomparison and Validation of High-Resolution Satellite Precipitation Estimates with 3-Hourly Gauge Data. J. Hydrometeorol. 10, 149–166. doi:10.1175/2008JHM1052.1

Schell, B., Ackermann, I.J., Hass, H., Binkowski, F.S., Ebel, A., 2001. Modeling the formation of secondary organic aerosol within a comprehensive air quality model system. J. Geophys. Res. Atmos. 106, 28275–28293. doi:10.1029/2001JD000384

Sessions, W.R., Fuelberg, H.E., Kahn, R.A., Winker, D.M., 2011. An investigation of methods for injecting emissions from boreal wildfires using WRF-Chem during ARCTAS. Atmos. Chem. Phys. 11, 5719–5744. doi:10.5194/acp-11-5719-2011

Shen, Y., Xiong, A., Wang, Y., Xie, P., 2010. Performance of high-resolution satellite precipitation products over China. J. Geophys. Res. 115, D02114. doi:10.1029/2009JD012097

Skamarock, W.C., Klemp, J.B., Dudhia, J., Gill, D.O., Barker, D.M., Duda, M.G., Huang, X.-Y., Wang, W., Powers, J.G., 2008. A Description of the Advanced Research WRF Version 3. NCAR Tech Notes-475+STR.

Stauffer, D.R., Seaman, N.L., 1990. Use of Four-Dimensional Data Assimilation in a Limited-Area Mesoscale Model. Part I: Experiments with Synoptic-Scale Data. Mon. Weather Rev. doi:10.1175/1520-

0493(1990)118<1250:UOFDDA>2.0.CO;2

Stockwell, W.R., Middleton, P., Chang, J.S., Tang, X., 1990. The second generation regional acid deposition model chemical mechanism for regional air quality modeling. J. Geophys. Res. Atmos. 95, 16,343-16,367. doi:10.1029/JD095iD10p16343

Sunny Lim, K.-S., Hong, S.-Y., Yoon, J.-H., Han, J., 2014. Simulation of the summer monsoon rainfall over East Asia using the NCEP GFS cumulus parameterization at different horizontal resolutions. Weather Forecast. 29, 1143–1154.

Tao, W.-K., Simpson, J., McCumber, M., 1989. An ice-water saturation adjustment. Mon. Weather Rev. 117, 231–235.

Taylor, Z.B., 2011. The impact of cumulus parameterization schemes on the convective transport of biomass burning emissions using WRF-Chem. Florida State Univ. Libr.

Thompson, G., Field, P.R., Rasmussen, R.M., Hall, W.D., 2008. Explicit Forecasts of Winter Precipitation Using an Improved Bulk Microphysics Scheme. Part II: Implementation of a New Snow Parameterization. Mon. Weather Rev. 136, 5095–5115. doi:10.1175/2008MWR2387.1

Thompson, G., Rasmussen, R.M., Manning, K., 2004. Explicit Forecasts of Winter Precipitation Using an Improved Bulk Microphysics Scheme. Part I: Description and Sensitivity Analysis. Mon. Weather Rev. 132, 519–542. doi:10.1175/1520-0493(2004)132<0519:EFOWPU>2.0.CO;2

Tiedtke, M., 1989. A comprehensive mass flux scheme for cumulus parameterization in large-scale models. Mon. Weather Rev. 117, 1779–1800.

Tripoli, G.J., Cotton, W.R., 1989. Numerical Study of an Observed Orogenic Mesoscale Convective System. Part 1: Simulated Genesis and Comparison with Observations. Mon. Weather Rev. 117, 273–304. doi:10.1175/1520-0493(1989)117<0273:NSOAOO>2.0.CO;2

UCAR, 2017. WRF Model Users' Page. URL http://www2.mmm.ucar.edu/wrf/users/ (accessed 5.1.17).

Unisys, 2013. 2013 Hurricane/Tropical Data for Western Pacific. URL http://www.weather.unisys.com/hurricane/w_pacific/2013/

Vadrevu, K.P., Lasko, K., Giglio, L., Justice, C., 2014. Analysis of Southeast Asian pollution episode during June 2013 using satellite remote sensing datasets. Environ. Pollut. 195, 245–256. doi:10.1016/j.envpol.2014.06.017

Velasco, E., Rastan, S., 2015. Air quality in Singapore during the 2013 smoke-haze episode over the Strait of Malacca : Lessons learned. Sustain. Cities Soc. 17, 122–131. doi:10.1016/j.scs.2015.04.006

Wang, B., Huang, F., Wu, Z., Yang, J., Fu, X., Kikuchi, K., 2009. Multi-scale climate variability of the South China Sea monsoon: A review. Dyn. Atmos. Ocean. 47, 15–37. doi:10.1016/j.dynatmoce.2008.09.004

Wang, J., Christopher, S.A., Nair, U.S., Reid, J.S., Prins, E.M., Szykman, J., Hand, J.L., 2006. Mesoscale modeling of Central American smoke transport to the United States: 1. "Top-down" assessment of emission strength and diurnal variation impacts. J. Geophys. Res. Atmos. 111, 1–21. doi:10.1029/2005JD006416

Wang, J., Ge, C., Yang, Z., Hyer, E.J., Reid, J.S., Chew, B.-N., Mahmud, M., Zhang, Y., Zhang, M., 2013. Mesoscale modeling of smoke transport over the Southeast Asian Maritime Continent: Interplay of sea breeze, trade wind, typhoon, and topography. Atmos. Res. 122, 486–503. doi:10.1016/j.atmosres.2012.05.009

Wang, X., Wu, Z., Liang, G., 2009. WRF/CHEM modeling of impacts of weather conditions modified by urban expansion on secondary organic aerosol formation over Pearl River Delta. Particuology 7, 384–391. doi:10.1016/j.partic.2009.04.007

Ward, E., 1999. Smoke from wildland fires. Heal. Guidel. Veg. FIRE EVENTS Backgr. Pap. 70–85.

Webb, E.K., 1970. Profile relationships: The log-linear range, and extension to strong stability. Q. J. R. Meteorol. Soc. 96, 67–90.

Wheeler, M.C., Hendon, H.H., 2004. An All-Season Real-Time Multivariate MJO Index: Development of an Index for Monitoring and Prediction. Mon. Weather Rev. 132, 1917–1932. doi:10.1175/1520-

0493(2004)132<1917:AARMMI>2.0.CO;2

Winker, D.M., Pelon, J., Coakley, J.A., Ackerman, S.A., Charlson, R.J., Colarco, P.R., Flamant, P., Fu, Q., Hoff, R.M., Kittaka, C., Kubar, T.L., Le Treut, H., McCormick, M.P., Mégie, G., Poole, L., Powell, K., Trepte, C., Vaughan, M.A., Wielicki, B.A., 2010. The CALIPSO Mission: A Global 3D View of Aerosols and Clouds. Bull. Am. Meteorol. Soc. 91, 1211–1229. doi:10.1175/2010BAMS3009.1

Wiwanitkit, V., 2008. PM10 in the atmosphere and incidence of respiratory illness in Chiangmai during the smoggy pollution. Stoch. Environ. Res. Risk Assess. 22, 437–440. doi:10.1007/s00477-007-0149-7

Wolter, K., Timlin, M.S., 1998. Measuring the strength of ENSO events: How does 1997/98 rank? Weather 53, 315–324. doi:10.1002/j.1477-8696.1998.tb06408.x

Wu, C.-H., Hsu, H.-H., 2009. Topographic Influence on the MJO in the Maritime Continent. J. Clim. 22, 5433–5448. doi:10.1175/2009JCLI2825.1

Wu, L., Su, H., Jiang, J.H., 2011a. Regional simulations of deep convection and biomass burning over South America: 1. Model evaluations using multiple satellite data sets. J. Geophys. Res. Atmos. 116, 1–14. doi:10.1029/2011JD016105

Wu, L., Su, H., Jiang, J.H., 2011b. Regional simulations of deep convection and biomass burning over South America: 2. Biomass burning aerosol effects on clouds and precipitation. J. Geophys. Res. 116, D17209. doi:10.1029/2011JD016106

Yesubabu, V., Srinivas, C. V., Ramakrishna, S.S.V.S., Hari Prasad, K.B.R.R., 2014. Impact of period and timescale of FDDA analysis nudging on the numerical simulation of tropical cyclones in the Bay of Bengal. Nat. Hazards 74, 2109–2128. doi:10.1007/s11069-014-1293-2

Ying, M., Bai, L., Zhan, R., 2014. Tropical Cyclone Activity over the western North Pacific in 2013. Trop. CYCLONE Res. Rev. 3, 131–144. doi:10.6057/2014TCRR03.01

Yu, E., Wang, H., Gao, Y., Sun, J., 2011. Impacts of cumulus convective parameterization schemes on summer monsoon precipitation simulation over

China. Acta Meteorol. Sin. 25, 581–592. doi:10.1007/s13351-011-0504-y

Zhang, C., 2013. Madden–Julian Oscillation: Bridging Weather and Climate. Bull. Am. Meteorol. Soc. 94, 1849–1870. doi:10.1175/BAMS-D-12-00026.1

Zhang, C., 2005. Madden-Julian Oscillation. Rev. Geophys. 43, RG2003. doi:10.1029/2004RG000158

Zhang, C., Wang, Y., Hamilton, K., 2011. Improved representation of boundary layer clouds over the southeast Pacific in ARW-WRF using a modified Tiedtke cumulus parameterization scheme. Mon. Weather Rev. 139, 3489–3513.

Zhong, M., Saikawa, E., Liu, Y., Naik, V., Horowitz, L.W., Takigawa, M., Zhao, Y., Lin, N.H., Stone, E.A., 2016. Air quality modeling with WRF-Chem v3.5 in East Asia: Sensitivity to emissions and evaluation of simulated air quality. Geosci. Model Dev. 9, 1201–1218. doi:10.5194/gmd-9-1201-2016

Zilitinkevich, S., 1995. Non-local turbulent transport pollution dispersion aspects of coherent structure of convective flows. Air Pollut. III, Air Pollut. theory Simul. (H Power, N Moussiopoulos, CA Brebbia, eds) Comput. Mech. Publ, Southampton, Bost. 1, 53–60.

APPENDICES

Appendix A: namelist.wps

```
&share
 wrf_core             = 'ARW',
 max_dom              = 2,
 start_date           = '2013-06-14_00:00:00','2013-06-14_00:00:00',
 end_date             = '2013-06-27_00:00:00','2013-06-27_00:00:00',
 interval_seconds     = 21600
 io_form_geogrid      = 2,
/
&geogrid
 parent_id            =   1, 1,
 parent_grid_ratio    =   1, 3,
 i_parent_start       =   1, 18,
 j_parent_start       =   1, 25,
 e_we                 =  160, 172,
 e_sn                 =  150, 172,
 geog_data_res        = 'modis_30s+10m', 'modis_30s+5m',
 dx                   = 27000,
 dy                   = 27000,
 map_proj             = 'mercator',
 ref_lat              =  6.25,
 ref_lon              = 110,
 truelat1             =  2.496,
 stand_lon            = 102.6,
 geog_data_path       = '/panfs/panasas01.panfs.cluster/WRF_DATA/geog'
```

```
 opt_geogrid_tbl_path = '/home/ezamo1/june2013/wps_001'
/
&ungrib
 out_format              = 'WPS',
 prefix                  = 'case_001',
/
&metgrid
 fg_name                 = 'case_001', 'PRES'
 io_form_metgrid         = 2,
 opt_metgrid_tbl_path = '/home/ezamo1/june2013/wps_001'
  /
```

Appendix B: namelist.input

```
&time_control
 run_days                            = 1,
 run_hours                           = 0,
 run_minutes                         = 0,
 run_seconds                         = 0,
 start_year                          = 2013, 2013,
 start_month                         = 06, 06,
 start_day                           = 26, 26,
 start_hour                          = 00, 00,
 start_minute                        = 00, 00,
 start_second                        = 00, 00,
 end_year                            = 2013, 2013,
 end_month                           = 06, 06,
 end_day                             = 27, 27,
 end_hour                            = 00, 00,
 end_minute                          = 00, 00,
 end_second                          = 00, 00,
 interval_seconds                    = 21600,
 input_from_file                     = .true., .true.,
 history_interval                    = 60, 60,
 frames_per_outfile                  = 72, 72,
 restart                             = .True.,
 restart_interval                    = 1440,
 write_hist_at_0h_rst                = .True.,
 io_form_history                     = 2,
 io_form_restart                     = 2,
 io_form_input                       = 2,
```

```
 io_form_boundary           = 2,
 auxinput5_inname           = 'wrfchemi_d<domain>',
 auxinput6_inname           = 'wrfbiochemi_d<domain>',
 auxinput7_inname           = 'wrffirechemi_d<domain>',
 auxinput8_inname           = 'wrfchemi_gocart_bg_d<domain>',
 auxinput12_inname          = 'wrf_chem_input',
 auxinput13_inname          = 'wrfchemv_d<domain>',
 auxinput5_interval_m       = 60,  60,
 auxinput7_interval_m       = 1440, 1440,
 frames_per_auxinput7       = 1, 1,
 io_form_auxinput2          = 2,
 io_form_auxinput5          = 2,
 io_form_auxinput6          = 0,
 io_form_auxinput7          = 0,
 io_form_auxinput8          = 0,
 io_form_auxinput12         = 2,
 io_form_auxinput13         = 0,
 debug_level                = 0,
 auxinput1_inname           = "met_em.d<domain>.<date>",
 /
 &dfi_control
/
 &domains
 time_step                  = 90,
 time_step_fract_num        = 0,
 time_step_fract_den        = 1,
 max_dom                    = 2,
 s_we                       = 1, 1,
 e_we                       = 160, 172,
```

s_sn = 1, 1,

e_sn = 150, 172,

e_vert = 51, 51,

eta_levels = 1.000, 0.997, 0.992, 0.986, 0.974, 0.960, 0.948, 0.934, 0.922, 0.908, 0.896, 0.882, 0.870, 0.856, 0.831, 0.805, 0.779, 0.766, 0.753, 0.740, 0.727, 0.714, 0.675, 0.662, 0.623, 0.597, 0.571, 0.545, 0.519, 0.493, 0.467, 0.441, 0.415, 0.389, 0.363, 0.337, 0.311, 0.260, 0.208, 0.156, 0.143, 0.130, 0.117, 0.104, 0.091, 0.078, 0.052, 0.031, 0.021, 0.010, 0.000,

num_metgrid_levels = 61,

num_metgrid_soil_levels = 4,

dx = 27000, 9000,

dy = 27000, 9000,

grid_id = 1, 2,

parent_id = 1, 1,

i_parent_start = 1, 18,

j_parent_start = 1, 25,

parent_grid_ratio = 1, 3,

parent_time_step_ratio = 1, 3,

p_top_requested = 5000,

numtiles = 16,

feedback = 0,

smooth_option = 0

zap_close_levels = 50

interp_type = 1

t_extrap_type = 2

force_sfc_in_vinterp = 0

use_levels_below_ground = .true.

use_surface = .true.

lagrange_order = 1

/

sfcp_to_sfcp = .true.

```
&physics
mp_physics                          = 2, 2,
progn                               = 0, 0,
ra_lw_physics                       = 4, 4,
ra_sw_physics                       = 4, 4,
radt                                = 27, 27,
sf_sfclay_physics                   = 2, 2,
sf_surface_physics                  = 2, 2,
bl_pbl_physics                      = 2, 2,
bldt                                = 0, 0,
cu_physics                          = 2, 2,
cugd_avedx                          = 1,
cu_diag                             = 0, 0,
cudt                                = 0, 0,
ishallow                            = 1,
isfflx                              = 1,
ifsnow                              = 1,
icloud                              = 1,
surface_input_source                = 1,
num_soil_layers                     = 4,
num_land_cat                        = 20,
sf_urban_physics                    = 0,
mp_zero_out                         = 2,
mp_zero_out_thresh                  = 1.e-12
maxiens                             = 1,
maxens                              = 3,
maxens2                             = 3,
maxens3                             = 16,
ensdim                              = 144,
```

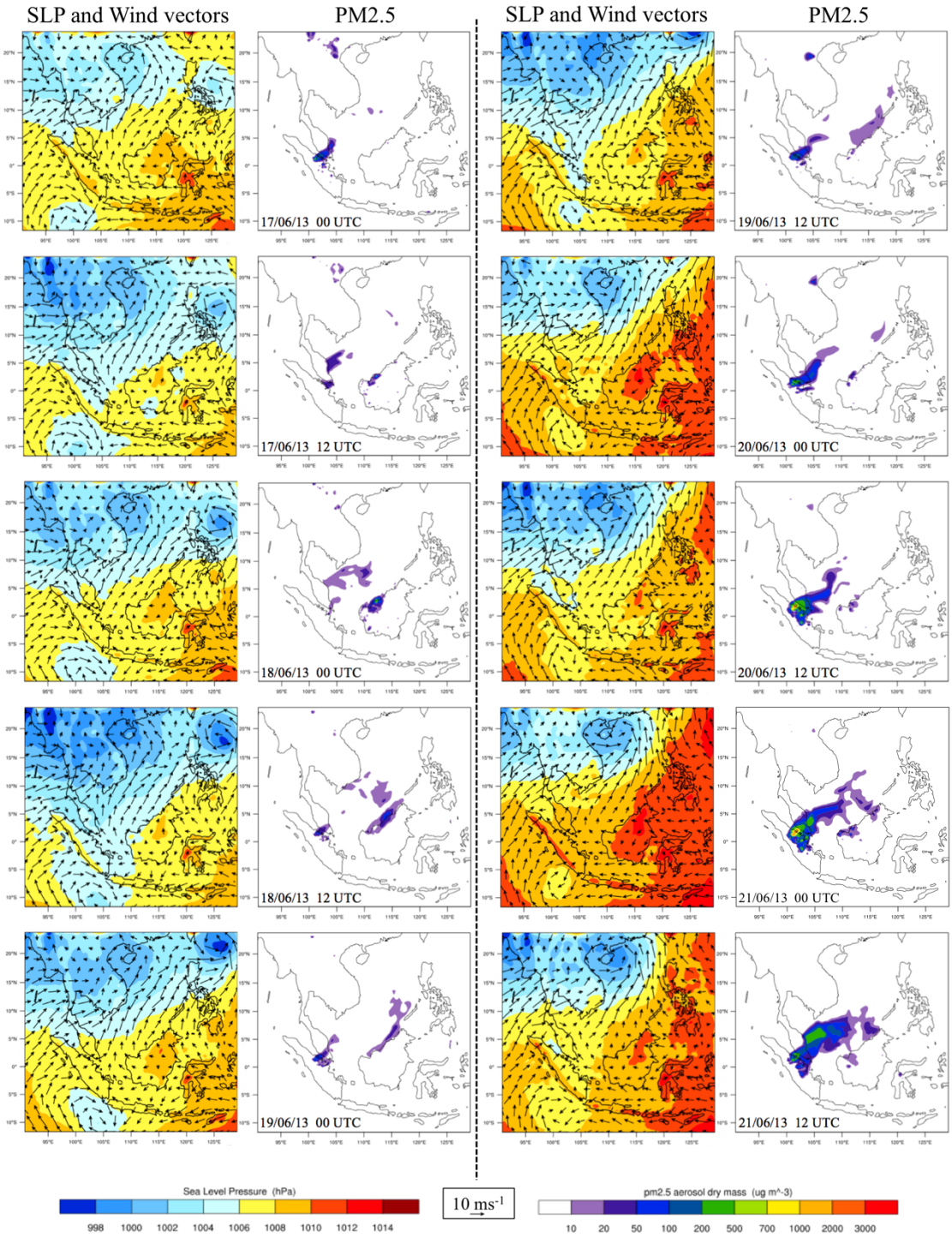
```
cu_rad_feedback             = .True., .True.,
/
&fdda
grid_fdda                   =  1, 1,
gfdda_inname                = "wrffdda_d<domain>",
gfdda_end_h                 =  24,24,
gfdda_interval_m            = 360, 360,
fgdt                        =   0, 0,
if_no_pbl_nudging_uv        =   0, 0,
if_no_pbl_nudging_t         =   0, 0,
if_no_pbl_nudging_q         =   0, 0,
if_zfac_uv                  =   0, 0,
 k_zfac_uv                  =  18, 18,
if_zfac_t                   =   0, 0,
 k_zfac_t                   =  18, 18,
if_zfac_q                   =   0, 0,
 k_zfac_q                   =  18, 18,
guv                         = 0.0003, 0.0003,
gt                          = 0.0003, 0.0003,
gq                          = 0.0003, 0.0003,
if_ramping                  = 1,
dtramp_min                  = 60.0,
io_form_gfdda               = 2,
/
&dynamics
rk_ord                      = 3,
w_damping                   = 1,
diff_opt                    = 1,
km_opt                      = 4,
```

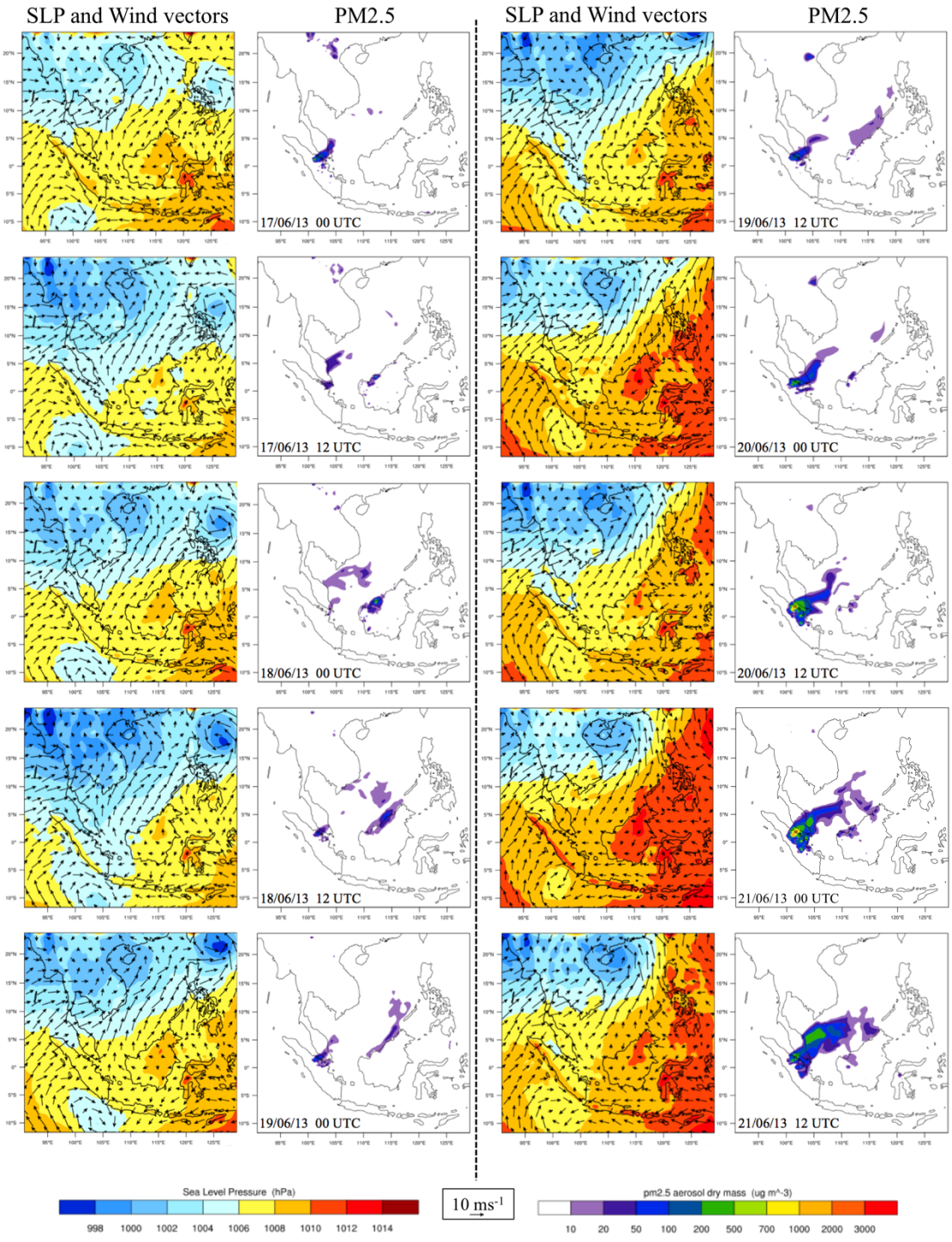
```
diff_6th_opt                = 0,
diff_6th_factor             = 0.12,
base_temp                   = 290.
damp_opt                    = 0,
zdamp                       = 5000., 5000.,
dampcoef                    = 0.01, 0.01,
khdif                       = 0, 0,
kvdif                       = 0, 0,
non_hydrostatic             = .True., .True.,
moist_adv_opt               = 2, 2,
scalar_adv_opt              = 2, 2,
chem_adv_opt                = 2, 2,
tke_adv_opt                 = 2, 2,
time_step_sound             = 4, 4,
h_mom_adv_order             = 5, 5,
v_mom_adv_order             = 3, 3,
h_sca_adv_order             = 5, 5,
v_sca_adv_order             = 3, 3,
/
&bdy_control
spec_bdy_width              = 5,
spec_zone                   = 1,
relax_zone                  = 4,
specified                   = .true., .false.,
nested                      = .false., .true.,
/
&grib2
/
&namelist_quilt
```

```
 nio_tasks_per_group      = 0,
 nio_groups               = 0,
/
 &chem
 kemit                    = 19,
 chem_opt                 = 2, 2,
 bioemdt                  = 0, 0,
 photdt                   = 30, 30,
 chemdt                   = 2.5, 2.5,
 io_style_emissions       = 2,
 emiss_opt                = 3, 3,
 chem_in_opt              = 1, 1,
 phot_opt                 = 2, 2,
 gas_drydep_opt           = 1, 1,
 aer_drydep_opt           = 1, 1,
 bio_emiss_opt            = 0, 0,
 dust_opt                 = 0,
 dmsemis_opt              = 0,
 seas_opt                 = 0,
 gas_bc_opt               = 1, 1,
 gas_ic_opt               = 1, 1,
 aer_bc_opt               = 1, 1,
 aer_ic_opt               = 1, 1,
 gaschem_onoff            = 1, 1,
 aerchem_onoff            = 1, 1,
 wetscav_onoff            = 0, 0,
 cldchem_onoff            = 0, 0,
 vertmix_onoff            = 1, 1,
 chem_conv_tr             = 0, 0,
```

```
biomass_burn_opt        = 0, 0,
plumerisefire_frq       = 30, 30,
have_bcs_chem           = .False., .False.,
aer_ra_feedback         = 0, 0,
aer_op_opt              = 1, 1,
opt_pars_out            = 1,
diagnostic_chem         = 0,
/
&tc
/
&noah_mp
/
&scm
/
&fire
/
 &diags
/
```

Appendix C: Sea-level pressure (SLP) with wind vectors at 12-hour intervals for 17 – 26 June 2013




SLP and Wind vectors
PM2.5
SLP and Wind vectors
PM2.5
17/06/13 00 UTC
19/06/13 12 UTC
17/06/13 12 UTC
20/06/13 00 UTC
18/06/13 00 UTC
20/06/13 12 UTC
18/06/13 12 UTC
21/06/13 00 UTC
19/06/13 00 UTC
21/06/13 12 UTC
Sea Level Pressure (hPa)
998 1000 1002 1004 1006 1008 1010 1012 1014
10 ms-1
pm2.5 aerosol dry mass (ug m^-3)
10 20 50 100 200 500 700 1000 2000 3000

PUBLICATIONS AND CONFERENCES

Journal Publications

1. Oozeer, M.Y., Chan, A., Wang, J., Reid, J.S., Salinas, S.V., Ooi, M.C.-G., Morris, K.I., Ashfold, M.J., 2017. The Uncharacteristic Occurrence of the June 2013 Biomass-Burning Haze Event in Southeast Asia: Combined Effect of the MJO and Tropical Cyclone Activity. J. Geophys. Res. Atmos. (under review).
2. Oozeer, M.Y., Chan, A., Ooi, M.C.-G., Zarzur, A.M., Salinas, S.V., Chew, B.-N., Morris, K.I., Choong, W.-K., 2016. Numerical Study of the Transport and Convective Mechanisms of Biomass Burning Haze in South-Southeast Asia. Aerosol Air Qual. Res. 16, 2950–2963. doi:10.4209/aaqr.2015.07.0461

Conferences

1. Oozeer, M.Y., Chan, A., Reid, J.S., Wang, J., Salinas, S.V., Ooi, M.C.-G., Morris, K.I., 2017. A case study of the June 2013 Biomass-Burning Haze event using WRF-Chem: Model sensitivity study and vertical transport of haze. 4th International Conference on Atmospheric Sciences and Application to Air Quality, Strasbourg, France.
2. Oozeer, M.Y., Chan, A., Wang, J., Salinas, S.V., Ooi, M.C.-G., Choong, W.-K., 2016. A Case Study of the June 2013 Biomass-Burning Haze Event using WRF-Chem. 16th EMS Annual Meeting & 11th European Conference on Applied Climatology (EMS 2016), Trieste, Italy.
3. Oozeer, M.Y., Chan, A., Wang, J., Salinas, S.V., Ooi, M.C.-G., Choong, W.-K., 2016. Evaluation of WRF-Chem Model: A Case Study of the June 2013 Biomass-Burning Haze Event. 32nd Conference on Agricultural and Forest Meteorology (AMS 2016), Salt Lake City, United States of America (in proceeding).
4. Oozeer, M.Y., Chan, A., Ooi, M.C.-G., Zarzur, A.M., Salinas, S.V., Chew, B.-N., 2015. Evaluation of WRF-Chem Model with High-Spectral Resolution Lidar Data of Singapore: A Case Study of the June 2013 Biomass Burning Haze event. 12th Annual Meeting (AOGS 2015), Singapore.